

Methodology for Designing Megawatt-scale Yokeless and Segmented Armature (YASA) Generators for Wind Turbines

Sook Teng Vun

Wolfson College

A thesis submitted in fulfilment of requirement for the degree of
DPhil in Engineering Science at The University of Oxford

Abstract

This thesis develops design methodologies for megawatt (MW)-scale yokeless and segmented armature (YASA) generators for wind turbine applications. The methodologies include the electromagnetic, the structural and the thermal designs of a YASA generator.

The design process starts with developing an analytical method to generate preliminary machine designs for a megawatt-scale YASA generator. This analytical approach considers both electromagnetic and structural aspects of a generator, the parameters of which were obtained and visualised on a design reference map. This new concept of displaying machine parameters is useful for a designer to identify the relationship between them. An optimisation tool using pseudo-weight approach is integrated into the analytical tool to determine a optimum machine design. This is a flexible optimisation tool, allowing the user to give priorities to each objective function. The analytical calculation has reduced the design space for suitable machine candidates to be applied in further finite element analysis (FEM). In finite element analysis of an optimised YASA machine, the electromagnetic performance of a 1 MW YASA generator was produced and verified with analytical and experiment results. This is followed by structural

optimisation with finite element method, where a spider wheel with a support ring geometry is applied to the rotor plate. This reduces the structural weight by more than 50% while the structure retain strong stiffness. Finally, the cooling system of the stator of the YASA generator is studied and the cooling channels design is proposed. Simulation results show that the stator of a 1 MW YASA generator can be effectively cooled with forced air.

Acknowledgements

I would like to thank my supervisor Dr Malcolm McCulloch for his continuous help and support in the process of my PhD. I thank him for being a good mentor and encouraging and helping me to shape this research. I also thank him for helped me with my English and academic writing, which I do think they have improved a lot over the years.

My gratitude also goes to Dr Marcus Leong who was the supervisor of me in my first year. I really learned a lot from him about how to do research and how to be a successful PhD. After he left Oxford for a better career, he still cares about my progress and has contacted me many times about my work.

I would like to thank my colleague in the Energy Power Group: Dr Tim Woolmer has shared with me a lot of knowledge about YASA and helping me with initial modelling. He also provided me the data of power efficiency map; Mr Richard Wong for helping with MatLab programming when I was stuck in numerous errors in codes, Mr Syarif Yahya, Mr Keng Wai Chan and Mr Ren Kang for teaching me how to use Solidworks, Mr Robert Camilleri for discussing the cooling system for a YASA machine, Mr Nathan Ewin for helping me set up the YASA machine rig.

I thank Prof Peter Ireland at the Osney Thermo-Fluid Laboratory for helping me with the thermochromic liquid crystal experiment, and Dr Matthew McGilvray for helping set up the experiment, Mr Trevor Godfrey, Mr Gerald Walker and Mr Duncan Blake for building the experimental rig.

Finally, I want to thank my family, who has given me a lot of support in this journey. Even though none of you will ever read, this thesis is especially dedicated to you.

Statement of Originality

This thesis is an account of work carried out by the author in the Department of Engineering Science, the University of Oxford under the supervision of Dr Malcolm McCulloch. Where the work of others has been drawn upon this is duly acknowledged in the text, and a list of references is presented at the end of each chapter. No part of this thesis has been submitted towards the completion of another degree at the University of Oxford or elsewhere. Parts of the thesis have been submitted to or published in the following journal or conference proceeding:

Journal article:

Vun, S. T., & McCulloch, M. D. (2015). Optimal Design Method for Large Scale YASA Machines. *IEEE Transactions on Energy Conversion "Optimal Design of Electric Machines",(pp.1-8)*.

Conference proceeding:

Vun, S. T., McCulloch, M. D., & Leong, C. Y. (2011). The development of an electromagnetic analytical design tool for megawatt-scale YASA generators. In *IET Conference on Renewable Power Generation (RPG 2011)*. IET.

Table of Contents

Abstract ..... **i**

Acknowledgements ..... **iii**

Statement of Originality ..... **v**

Table of Contents ..... **vi**

Nomenclature ..... **x**

Chapter 1 – Introduction **1**

1.1 Background 1

1.2 Trends in wind turbine technology 3

1.3 Research Motivation 6

1.4 Research objectives 8

1.5 Contribution to knowledge 9

1.6 Organisation of the thesis 10

Chapter 2 – Literature Review **12**

2.1 Background: the energy conversion system 12

2.2 Wind turbine generator systems 15

2.2.1 Fixed speed vs variable speed systems 16

2.2.2 Geared vs direct-drive systems 21

2.2.3 Electrically excited vs permanent magnet synchronous generator 24

2.3 Axial flux permanent magnet machines 28

2.4 Yokeless and segmented armature (YASA) machine 31
2.5 Methodologies for electrical machine design 36
2.5.1 Electromagnetic design 37
2.5.2 Structural design 42
2.5.3 Thermal analysis 44
2.6 Summary 46
Chapter 3 – Analytical Design Methods 47
3.1 Analytical design tool 48
3.2 Electromagnetic Design 50
3.2.1 Sizing equations 50
3.2.2 Estimation of power losses 59
3.2.3 Cost of active materials 61
3.2.4 Validation of the sizing equations 62
3.3 Structural design 63
3.3.1 Roark's formula approach 63
3.4 Optimisation process 66
3.4.1 Objective functions and variables 67
3.4.2 Design reference map 69
3.4.3 Optimisation with pseudo-weight vector approach 72
3.4.4 Sensitivity test 79
3.5 Properties and performance of the YASA machine 84
3.5.1 Efficiency map of the YASA generator 84
3.5.2 Validation of efficiency map calculation 87

3.5.3 No load air gap flux density 89
3.5.4 Winding design 91
3.5.5 Back EMF 94
3.5.6 Cogging Torque 96
3.6 Comparison of a MW-scale YASA machine with the transverse flux and radial flux machines 97
3.7 Summary 99
Chapter 4 – Electromagnetic Design 100
4.1 Finite element modeling, boundary condition and meshing 101
4.2 Flux density allowance on the magnetic materials 106
4.3 No-load steady state electromagnetic analysis 107
4.3.1 Air gap flux density 107
4.3.2 Back EMF waveforms 110
4.3.3 Cogging Torque 112
4.3.4 Validation of FEM with an existing 50 kW YASA machine. 114
4.4 Full-load steady state electromagnetic design 117
4.4.1 Saturation of iron under full load condition 117
4.4.2 Magnetic attractive force 118
4.4.3 Torque 118
4.5 Method to fabricate laminated stator core with electrical steel 120
4.6 Summary 121
Chapter 5 – Structural Design 123
5.1 Boundary conditions, meshing and convergence 124

5.2 Deflection simulation of rotor plates 125
5.3 Improving the rotor plate design 127
5.3.1 Determining the number of spokes....128
5.3.2 Analysis of spoke dimensions....129
5.3.3 Validation of the spider wheel design with the FEM 133
5.4 Rotor plates design with a support ring....139
5.5 Structure design of the stator 141
5.6 Proposed assembly method 144
5.7 Summary 146
Chapter 6 – Thermal Design 147
6.1 Forced air cooling system 149
6.2 Computational fluid dynamics (CFD) simulation 151
6.2.1 Boundary conditions and meshing 151
6.2.2 Determination of inlet mass flow rate....152
6.3 Summary 159
Chapter 7 – Conclusions and Further Work 161
7.1 Conclusions....161
7.2 Further work....163
Appendix I....168
Appendix II 169
Biblography....172

Nomenclature

Roman letters	Descriptions
a	Outer radius of the rotor plate
A	Surface area
A_{BI}	Surface area of back iron
A_{cp}	Cross sectional area of the channel between two stator cores
A_{Cu}	Surface area of copper coil
A_d	Area of flow path
A_g	Surface area of air gap
A_H	Surface area of the machine housing
A_m	Surface area of the permanent magnet
A_{PM}	Surface of permanent magnet
A_s	Electrical loading
A_{sc}	Surface area of stator core
A_v	Effective surface area
b	Radius of the shaft
B_{ag}	Air gap flux density (T)
B_{BI}	Maximum flux density of back iron
B_g	Average air gap flux density
B_{PM}	Magnetic flux density
B_r	Remanent flux density
B_{sh}	Maximum flux density of stator shoe
B_t	Maximum flux density of stator tooth
CFD	Computational fluid dynamics
C_m	Moment coefficient

C_{φ}	Magnet concentration factor
D	Plate constant
dcu	Depth of coil
DH	Hydraulic diameter of the rectangular duct
din	Diameter of inlet
D_o	Outer diameter of the machine
$dout$	Diameter of outlet
dr	Depth of reservoir
dsb	Depth of stator bar
dsh	Depth of stator shoes
D_{tot}	Total outer diameter
d_w	Diameter of single conductor
E	Modulus of elasticity
f_0	Electrical frequency
f_e	Frequency of the field in the stator iron
FEM	Finite-element method
f^{max}	Maximum objective function value
f^{min}	Minimum objective function value
F_{PM}	Magnetic attractive forces
g	Air gap length
G	Air gap ratio
g_e	Effective air gap length
h	Convection heat transfer coefficient
H	Hysteresis losses
I_{rms}	Root mean square current
J_{rms}	Root mean square current density
k	Thermal conductivity
k_{BI}	Thermal conductivity of rotor back iron
K_c	Carter's Coefficient
k_{Cu}	Thermal conductivity of copper

k_d	Ratio of inner to outer diameter
k_e	EMF factor
k_f	Fill factor of the stator
k_{fluid}	Thermal conductivity of fluid
k_H	Thermal conductivity of the machine housing
k_i	Current waveform factor
k_l	Leakage factor
k_p	Electrical power waveform factor
k_{PM}	Thermal conductivity of permanent magnet
k_r	Magnetic path reluctance factor
k_{sc}	Thermal conductivity of stator core
l	Length of flow path
l_{act}	Length of active copper
l_{BI}	Length of the back iron
l_e	Total effective length of the machine
l_{endi}	Length of the outer end-windings
l_{endo}	Length of the inner end-windings
l_{PM}	Length of the permanent magnet
l_{sc}	Length of stator core
l_{sh}	Length of the stator shoe
l_{ss}	Length of the stator slot
l_{turn}	Average length of one turn of copper coil
m	Number of machine phase
M	Total number of objective functions
m_1	Number of phase of each stator
m_r	Mass of rotor discs
M_{rb}	Unit radial bending moment
n	Number of harmonic
n_{disc}	Number of rotor disc
N_{ph}	Number of turns per phase

N_{ph}	Number of turns per phase
N_{turn}	Number of turns per coil
Nu	Nusselt number
Nu_m	Mean Nusselt number
p	Number of pole pair
P	Rated power of the machine
P	Wetted perimeter
P_{Cu}	Copper losses
P_{Fe}	Iron losses
P_{in}	Input power
P_{loss}	Power losses
P_{out}	Output power
q	Magnetic pressure
Q	Number of slots
Q_b	Unit shear force
$q_{cond.}$	Heat transfer rate of conduction
$q_{conv.}$	Heat transfer rate of convection
r	Outer radius of the machine
R	Resistance
r_0	Radius from the centre of shaft to the starting point of the stress applied
Ra	Rayleigh number
R_{c1}	Convection Thermal Resistance between stator casing and air gap
R_{c2}	Convection Thermal Resistance between air gap and permanent magnet
R_{c3}	Convection Thermal Resistance between rotor back iron and air gap
R_{c4}	Convection Thermal Resistance between air gap and housing
R_{c5}	Convection Thermal Resistance between housing and air gap

$R_{cond.}$	Resistance of conduction
$R_{conv.}$	Resistance of convection
r_{Cu}	Resistivity of copper
R_{d1}	Conduction Thermal Resistance of copper coil
R_{d2}	Conduction Thermal Resistance of stator core
R_{d3}	Conduction Thermal Resistance of permanent magnet
R_{d4}	Conduction Thermal Resistance of rotor back iron
R_{d5}	Conduction Thermal Resistance of housing
R_{dc}	DC phase resistance of the stator windings
Re	Reynolds number
Re_{φ}	Rotational Reynolds number
R_{ph}	AC phase resistance of the stator windings
R_{TH}	Total thermal resistance
S_{ag}	Surface area of air gap
S_{PM}	Active surface area of permanent magnets
t	Thickness of the rotor plate
T	Temperature of the coil
T_f	Temperature of surrounding fluid
t_r	Minimum rotor thickness
T_s	Temperature of surface
v	Poisson's ratio
V	Volume of air gap
v	Viscosity of the cooling fluid
V_{Cu}	Volume of the copper coil
W	Total air gap coenergy
W_{act}	Total active material mass
W_{BI}	Mass of rotor back iron
w_{Cu}	Depth of copper
W_{Cu}	Mass of copper coil
$wdiv$	Width of divider

W_{Fe}	Mass of iron
w_i	Weight of the each objective function *i*
w_{PM}	Average width of permanent magnets
W_{PM}	Mass of permanent magnets
w_s	Width of stator core
w_{sd}	Slot depth
w_{sh}	Width of stator shoe
W_{sh}	Mass of a stator shoe
wss	Width of stator slot
W_t	Mass of stator teeth
x_{PF}	Pareto front
y_a	Deflection of the rotor disc
$YASA$	Yokeless and segmented armature
α_{cg}	Gap between the coils
α_p	Ratio between the magnet arc and the magnetic pole arc
α_{sh}	Ratio between arc of the shoes and the arc of the stator pole
α_t	Loss of tooth area due to radii
η	Efficiency
θ	Electrical angle
λ	Relative permeance of air gap with slotting effect
μ_0	Permeability of free space
μ_{PM}	Permanent magnet recoil permeability
μ_r	Recoil permeability
ρ_{air}	Density of air
ρ_{Cu}	Density of copper
ρ_{Fe}	Density of iron
ρ_{ms}	Density of mild steel
ρ_{PM}	Density of permanent magnet
τ_s	Stator pitch
χ	Skin depth of the conductor in free space

ω	Rotational speed
$\dot{m}$	Mass flow rate

Chapter 1 – Introduction

This thesis develops the electromagnetic, structural and thermal designs of a megawatt-scale direct-drive wind turbine generator based on a Yokeless and Segmented Armature (YASA) topology.

1.1 Background

As international pressure mounts to cut greenhouse gas emissions (The Kyoto Protocol) (United Nations 1998) and evidence directly linking CO_2 emissions to global warming continues to increase, governments are looking at means to reduce its dependency on fossil fuels and to adopt more sustainable methods of energy production from renewable sources. The rapid rise in demand for energy harnessed from renewable means in the near future has opened up new opportunities for research and development into sustainable technologies. Presently, out of all the renewable energy sources, the technology used to extract wind energy is the most mature with wind farms experiencing the fastest annual growth rate of installation (30%) (Polinder et al. 2007). At the end of 2012, it was revealed that the global wind electricity generating capacity increased from 238,035 MW in 2011 to 282,482 MW in 2012 (Global Wind Energy Council 2013). In

the foreseeable future, this capacity will need to increase substantially in order to meet the 2020 Kyoto targets.

The UK has met the Kyoto Protocol target to cut greenhouse gases by 12.5% by 2010 (Clark 2012). More than half of the installed renewable capacity in the UK came from wind generation. Since October 2008, the UK has been lead the world in capacity installed of offshore wind turbine (RenewableUK 2014). The capacity of electricity generated by the UK offshore wind farms is around 8 terawatt hours (TWh) annually, which is equivalent to the electricity consumption of around 2 million homes (RenewableUK 2014). The UK's first offshore wind farm was installed off the North Wales Coast in 2003. Currently, the largest offshore wind farm in the UK is the London Array with 175 of 3.6 MW wind turbines installed with a total of electricity capacity of 630 MW(London Array 2014). Other large-scale offshore wind farms in the UK include Greater Gabbard wind farm (504 MW) (4C Offshore 2014b), Walney wind farm (367 MW) (Walney (UK) Offshore Windfarms Ltd 2014) and Sheringham Shoal offshore wind farm (317 MW) (Sheringham Shoal 2014). At the end of 2013, the UK had 7 GW installed capacity of onshore wind, with 3.7 GW offshore wind (Department of Energy & Climate Change 2013).

To support this demand, there is a pressing need to explore and develop new generator topologies to replace some of the problematic conventional

geared generator systems. A novel generator design that can offer gearless direct-drive operation, higher operating efficiency and torque density and uses less materials which is cheap and simple to manufacture will ensure a more efficient delivery of clean energy (Departement of Energy & Climate Change 2011). In 2013, the UK installed a capacity 1,883 MW, of which 39% is offshore (The European Wind Energy Association 2014). In the recent two decades, wind turbines are increasingly being installed offshore to achieve more consistent and higher energy yields. Additionally, offshore wind farms are also less visually intrusive and installation space is not an issue.

1.2 Trends in wind turbine technology

Wind turbines convert wind energy into electrical energy. To generate a significant power to supply the national grid, megawatt (MW) wind farms usually consist of a large collection of interconnected wind turbines located in a specifically chosen area.

The power output of a wind turbine depends largely on the wind speed. Offshore wind speeds normally range between 5.5 m/s to 12 m/s (4C Offshore 2014a) and is generally higher and more consistent compared to onshore wind speeds which vary depending on geographical features and seldom exceeds 5 m/s to 7 m/s. On the downside, offshore wind farm sites are difficult to access, hence the installation cost are generally higher than onshore. To minimise this cost,

higher rated power wind turbines are generally used to reduce the number of wind turbines required to achieve the target energy demand. Fewer turbines mean maintenance costs are also lower.

The blades of MW-scale wind turbines also rotate at a lower speed (typically ≤25 rpm) compared to the operating speed of the generator; hence gearboxes are used to increase the speed of rotation to match with the higher operating speed generator. This also can compact the size of a generator in order for it to fit into a nacelle. To date, one of the most common problems associated with MW-scale wind turbines installed in the UK is gearbox mechanical failures (Feng et al. 2010). The high costs associated with gearbox failures disrupting wind farm power production are often reported (WindPower 2006; WindPower 2007; Windpower 2008). Power supplied to the grid has to maintain an acceptable degree of consistency and reliability to satisfy the baseline grid demand. Failure to deliver consistent power can lead to disruption to the end users and be costly to the energy suppliers. In addition, the cost of maintaining mechanical gearboxes can be expensive in the long term. To mitigate these issues, there is an urgent need to explore alternative generator systems that do not rely on a gearbox to operate. The direct-drive wind turbine is a suitable system that can replace the conventional geared generators.

The generator systems currently used by the top 10 wind turbine manufacturers of ear 2011 are summarised in Table 1.1 and an overview is shown in Figure 1.1. Details of these different types of generator systems will be discussed in Chapter 2.

Table 1.1: Top 10 wind turbine manufacturers of 2011. Current generator concepts and power ranges (Cleantech Investor Ltd 2012; Vestas 2013; Sinovel 2013; Goldwind 2013; Gamesa 2013; Enercon 2013; General Electric 2013; Guodian United Power Technology Co. Ltd 2013; Siemens 2013; Ming Yang 2013; Suzlon 2013).

Manufacturers	Concept	Rotor Diameter	Power Range
Vesta (Denmark)	DFIG DD PM	80-100m 80-164m	2-3MW 2-8MW
Sinovel (China)	DFIG	60-128m	1.5-5MW
Goldwind (China)	DD PM	70-100m	1.5-2.5MW
Gamesa (Spain)	DFIG GFC PM	52-97m 128m	850kW-2MW 4.5-5MW
Enercon (Germany)	DD EE	48-127m	800kW-7.5MW
GE Energy (USA)	DFIG GFC PM DD PM	70.5-82.5m 100m 110m	1.5MW 2.5MW 4MW
Suzlon (India)	FS	52-97m	600kW-2.1MW
Guodian United Power (China)	DFIG	77.36-100m	1.5-3MW
Siemens (Germany)	GFC IG DD PM	82-107m 101-154m	2.3-3.6MW 3-6MW
Ming Yang (China)	DFIG	77.1-82.6m	1.5-2MW

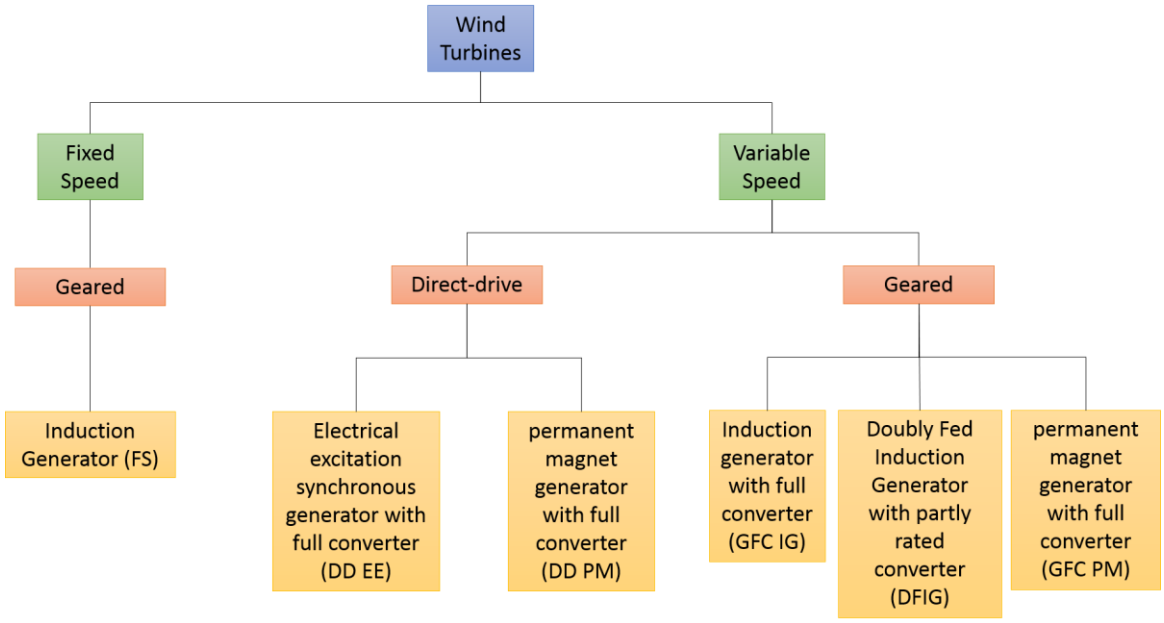


Figure 1.1: Overview of Generator Systems of wind turbines that currently used by the top 10 wind turbine manufacturer.

1.3 Research Motivation

Direct-drive or gearless generator systems have been introduced to avoid the problems associated with gearboxes. Permanent magnet synchronous machines are the most common direct-drive generator systems for wind turbines. As the cost of permanent magnets takes a significant portion of a total generator cost, improving the generator design to reduce the usage of permanent magnets and to improve efficiency will ultimately reduce the cost of the generators.

The YASA topology was developed to increase utilisation of permanent magnets compared to conventional axial flux machines (Woolmer 2009). An axial flux topology inherently requires less permanent magnets than a radial flux structure (Sitapati 2001). Without a yoke and using the concentrated windings, it

can increase the winding factors by using less end windings as well as less amount of iron in the stator, which reduces both copper and iron losses. A 50 kW YASA prototype for electric vehicles has been developed within the Energy and Power Group at Oxford University (Woolmer 2010; Woolmer 2009). It has proven to increase the overall torque density by around 20% and reduce the iron usage by 50% compared to a same size Torus axial flux machine.

To scale up the 50 kW YASA motor to a MW-scale generator, the associated weight increase is of major concern. A direct-drive generator system operates at the same speed as the rotational shaft of the turbine system. As the turbine typically rotates at low speeds, the direct-drive generators must produce large torques at low speed to achieve high power outputs. This tends to make them large in diameter, as the pole number must be increased. In addition, the rotor plates must also be strengthened as the increased magnetic attractive force may cause deflection. Additional materials are required to increase the stiffness of the structure. The structural weight will take a large portion of the total machine weight of a MW-scale direct-drive generator. The heavy weight and large diameter pose a problem for the transportation and the installation. Improving the structural design of the YASA topology to reduce its weight while maintaining the structural integrity is important in this design process.

1.4 Research objectives

The aim of this thesis is to develop mathematical tools and knowledge for the design and optimisation of YASA machines, taking into account of the electromagnetic properties, the structural stability and the thermal management of a complete generator system. The objectives can be summarised in the following points:

To develop an analytical tool for the design of a direct-drive MW-scale YASA generator. It is the first time that a YASA topology is applied to a MW-scale low speed machine, and therefore, an analytical design methodology needs to be developed. Analytical calculation is a fast and approximate approach to generate preliminary machine data, which can constrain the search space of an optimisation procedure using the finite-element method. Different designs that provide similar performance could emerge from this preliminary analysis. There may be an advantage to one design over another depending upon application requirements. Therefore, a multi-objective optimisation tool should be incorporated into the analytical tool to determine a unique design that can be carried forward for the finite-element study.

To optimise the YASA design using the finite-element methods by considering three-dimensional electromagnetic and structural properties of the YASA generator. It is essential to understand the electromagnetic performance of

a scaled-up YASA generator. The structure of the rotor plate will need be carefully designed to manage the weight increase. The CFD is used to design a forced air cooling system for the MW-scale YASA generator.

1.5 Contribution to knowledge

The contribution of knowledge of this thesis are stated as follows:

A design reference map, which provides a graphical presentation of the relationships between different machine parameters, is established using the analytical calculation. This technique provides the designers with a clear visualisation tool of where the design regions are and what compromises have be made in machine optimisation. This will be discussed in Chapter 3 and is published in a conference paper (Vun et al. 2011).

A novel multi-objective optimisation method has been applied to optimise YASA generators (Vun & McCulloch 2014). This is a flexible optimisation tool and a designer can sort priorities of the objectives. A paper is published in IEEE Transactions on Energy Conversion.

For the first time, a large-scale detailed electromagnetic design of the MW-scale YASA generator is presented. This is a new substantially different application of the topology.

A novel mechanical structural design of the rotors is presented in Chapter 5. The rotor design is a challenge at MW-scale.

The MW-scale YASA topology presents challenges in thermal management of such a large system with passages between stator cores having a high length-to-width ratio. To understand the real properties and to assist further cooling system design, detailed numerical simulations were studied.

1.6 Organisation of the thesis

To ground this thesis in the existing knowledge, Chapter 2 reviews the literature on current generator topologies applied to wind turbine applications and examines the methodologies used to design electrical machines. The design process starts with a fast analytical approach (Chapter 3), which characterises the whole design space of the machine candidates. This leads to a multi-objective optimisation process, which identifies a machine optimum such that the design space for finite-element analysis is reduced significantly. The optimised machine design is further studied in Chapter 4 by considering its detailed electromagnetic properties using commercial finite-element software. Having established the electromagnetic design, the structural component, mainly the rotor, is optimised to minimise the weight while maintaining the structural integrity (Chapter 5). Chapter 6 completes the design process by considering the thermal design using

the finite-volume method. The thesis finishes with key conclusions and ideas for further work.

Chapter 2 – Literature Review

This chapter reviews the generator systems used for wind turbine applications and the methodologies to design a new topology.

2.1 Background: the energy conversion system

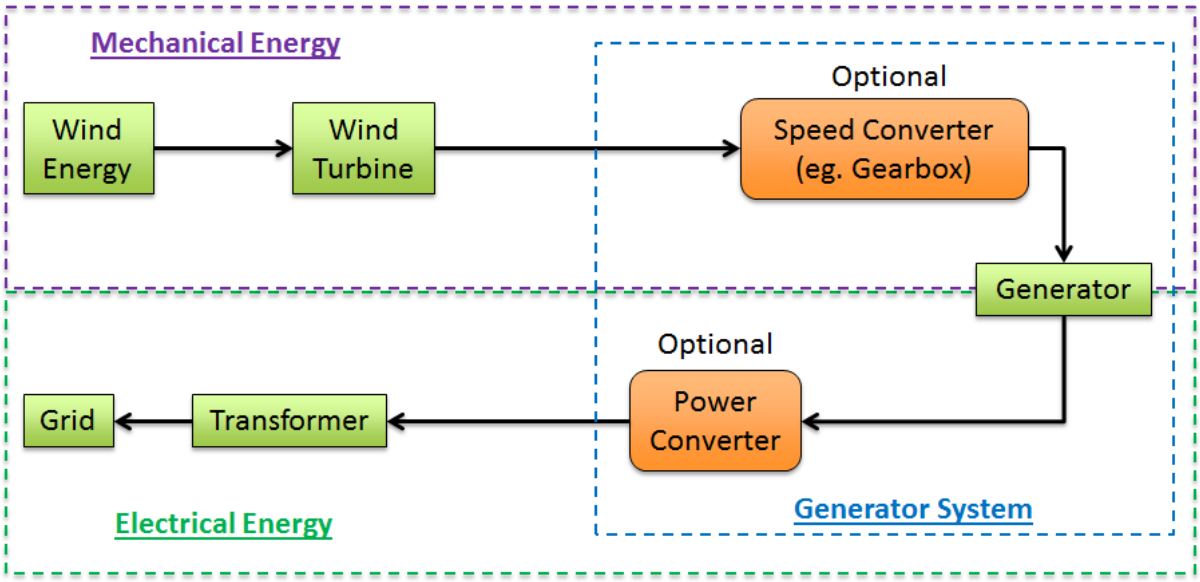


Figure 2.1: A typical wind energy conversion system.

Figure 2.1 shows a wind energy conversion system that is capable of harnessing wind energy sources that exist in the form of mechanical energy and transforming it to electrical energy. A wind generator system is an assembly of the components in the blue box. The system consists of a generator and two optional converters (speed and power). First, the generator system can be designed either

with or without gear. The second optional component, a power converter, consists of a set of electronically controlled switches to convert electricity from one form to another (from alternating current to direct current or vice versa). It also regulates the electrical frequency of the generator to match that of the grid. Finally, a transformer is used to alter the supply voltage magnitude to reduce power losses during transmission of the grid.

Wind power that is captured by wind turbines is directly proportional to the cube of wind speed (v_{wind}),

$$P_{turbine} = \frac{1}{2}\rho_{air} A C_p {v_{wind}}^3 \qquad (2.1)$$

where $P_{turbine}$ is the output power of the turbines, ρ_{air} is the air density, A is the swept area of the rotor blades, and C_p is the power coefficient. The power coefficient is to measure how efficient a wind turbine converts wind energy into electricity. The maximum value of the power coefficient is 0.593 based on the Betz limit introduced by Albert Betz, a German physicist. The limit exists because the cross section of the upstream air tube at full, free stream velocity is smaller than the area of the disc when the upstream tube expands when near to the actuator disc. The power coefficient is not a constant value. It varies with the tip speed ratio as shown in the performance curve of a modern three-bladed wind turbine (Figure 2.2). The tip speed ratio is defined by,

$$\lambda = \frac{v_{blade\ tip}}{v_{wind}} \tag{2.2}$$

where $v_{blade\text{-}tip}$ is the blade tip speed and v_{wind} is the wind speed. The maximum power coefficient is only 0.47 when the optimal tip speed ratio is 7 (Figure 2.2). The cut in tip speed ratio is around 1.4 and the cut out tip speed ratio is around 15.

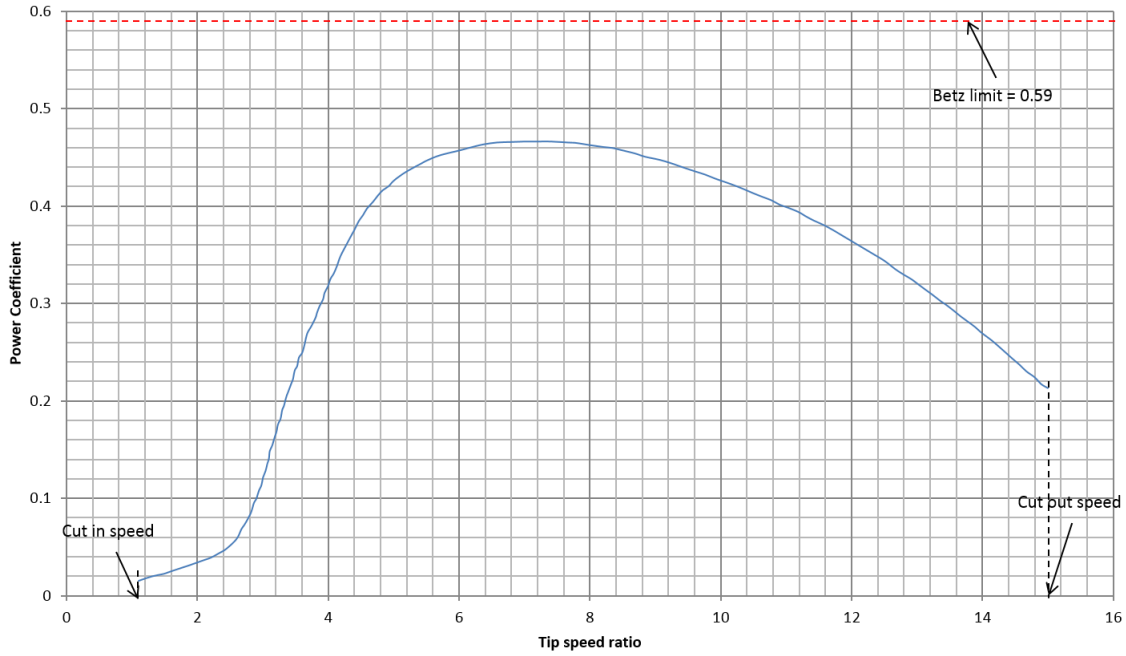


Figure 2.2: Performance curve for a modern three-blade turbine. Adapted from Burton et al.(2001) and Ragheb & Ragheb (2011).

As wind turbines can only extract the maximum power when it is operating at their optimal wind tip speed ratio, for conventional wind turbines with a fixed rotational speed, the wind turbines cannot capture the maximum wind energy under different wind speeds. Variable speed wind turbines can overcome this problem. Figure 2.3 shows the electrical power captured by a wind turbine with a

60 m rotor disc at four different constant wind speeds (5 m/s to 11 m/s). This demonstrates the sensitivity of changes in the power output at different wind speeds. About 70% increase in the peak electrical power when the wind speed increases from 9 m/s to 11 m/s. In this case, if a wind turbine is designed with a 1 MW rated power, 11 m/s is the rated wind speed and the rated rotational speed is 25 rpm.

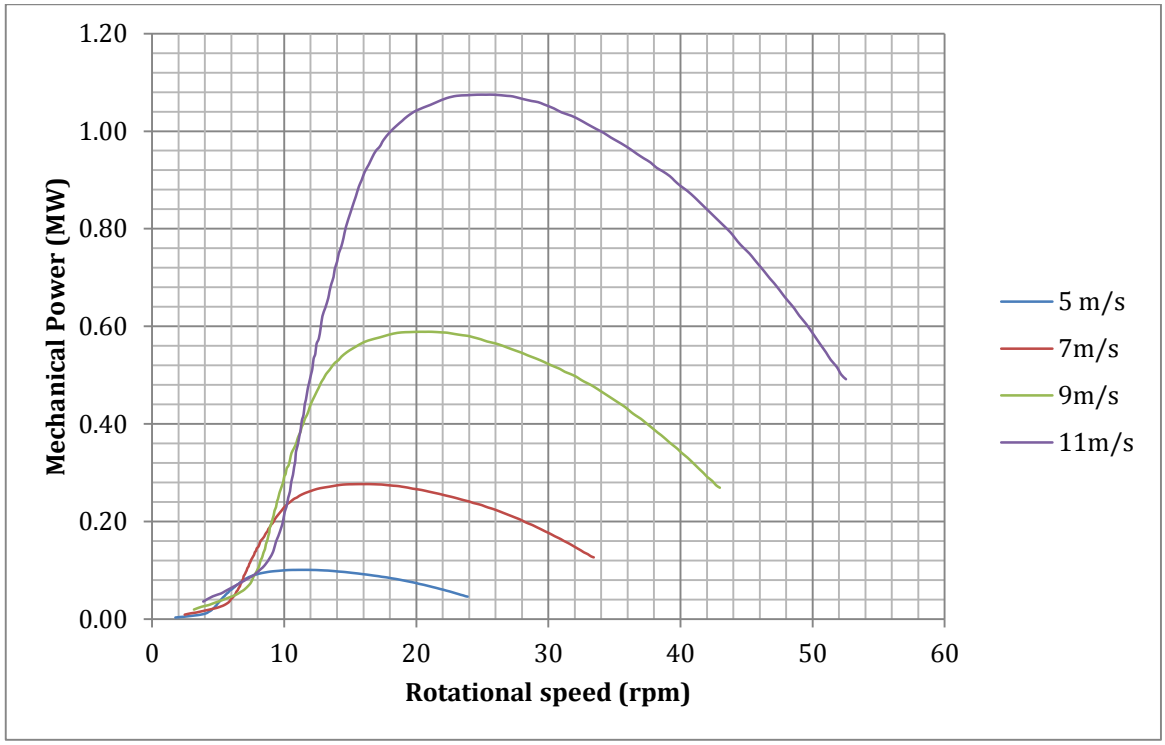


Figure 2.3: Comparison between mechanical power versus rotational speed curves under different wind speed.

2.2 Wind turbine generator systems

Figure 2.4 is an overview of the generator systems used for wind turbine applications. Each of these generator systems will be reviewed in the following

sub-sections based on this diagram. The flow along the red arrows is the configuration of the YASA generator studied in this thesis.

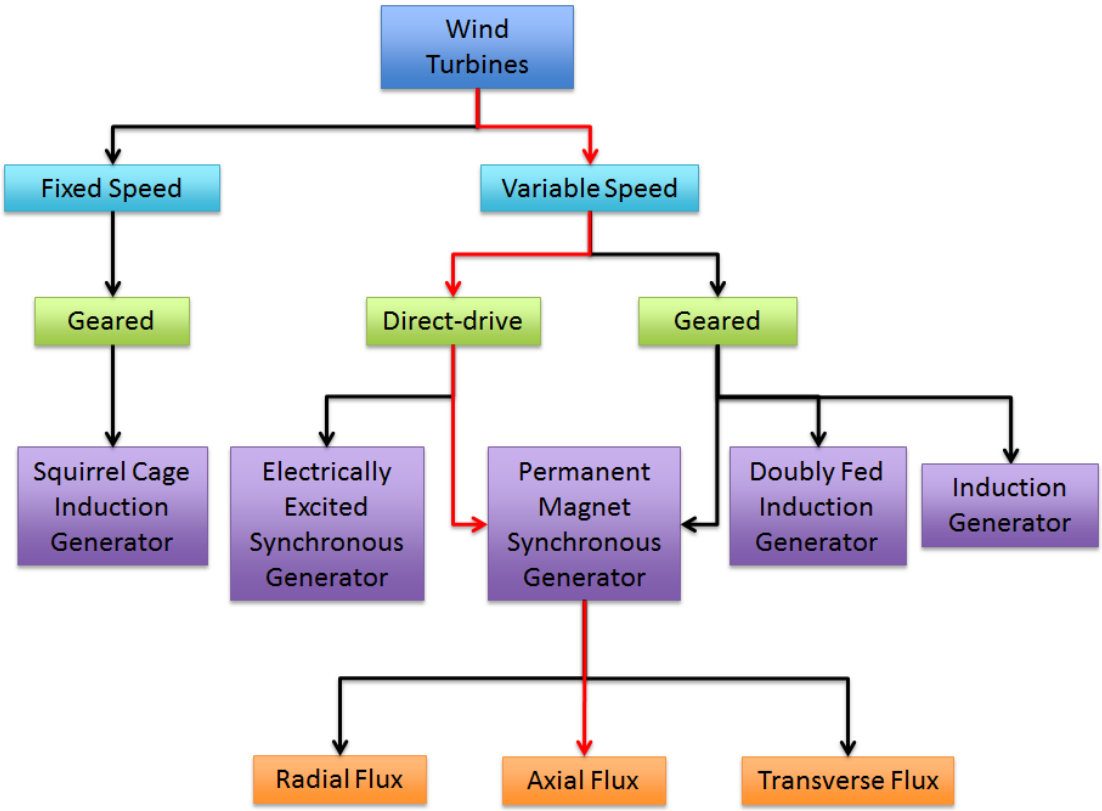


Figure 2.4: Overview of generator systems for wind turbines.

2.2.1 Fixed speed vs variable speed systems

For a direct-drive system, the rotation of the turbines is directly transferred to the rotation of the rotors in the generator. Therefore, the rotational speed of a direct drive generator tends to be low. Using a mechanical gearbox can increase the rotational speed such that a smaller machine diameter can be used to produce the same power, although it is a part that often fails. The relationship between the rotational speed and the machine diameter is described by Hanselman (1994),

$$\omega = \frac{P}{T} = \frac{P}{kD^2L} \tag{2.3}$$

where ω is the angular rotational speed, P is the generator rated power, T is the rotational torque, k is the constant of the generator, D is the outer diameter of the generator and L is the effective length of the generator.

The generator systems for wind turbines can either operate at a fixed speed based on the number of pole pairs of the generator and the blade pitch control, or at variable speed by varying the electrical frequency of the system using a power converter. The operating speed (n) of a generator is governed by the number of the machine pole pairs (p) and the electrical frequency of the grid (f) described by,

$$n = 60\frac{f}{p} \tag{2.4}$$

A fixed speed generator is designed to operate at a near-constant speed, allowing the output to match with the grid frequency. Since this generator has been designed to work optimally in a very narrow wind speed range, the energy yield of this system is limited if the wind speed fluctuations are high. To maintain a fixed speed operation during large fluctuations in wind conditions, the turbines, the blades, the gearbox and the generator will experience high mechanical stresses that can lead to failure.

A typical fixed speed wind turbine configuration, where a multi-stage gearbox is used with a squirrel cage induction generator (SCIG) to feed power directly to the grid, is shown in Figure 2.5. The SCIG is an asynchronous machine consists of a stator and a rotor that are separated by a uniform air gap. The SCIG rotor is made up of aluminium or copper bars which are connected together by aluminium or copper rings at both ends, resembling a squirrel cage. A rotating magnetic field is generated in the air gap when an alternating current is applied to the stator of the asynchronous machine. Through induction, a back electromagnetic force (EMF) is induced on the stator coils, which supplies power to the grid.

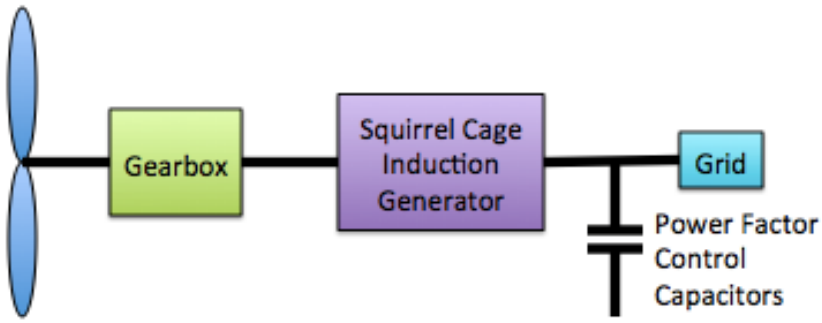


Figure 2.5: A typical configuration of a fixed speed wind turbine with an induction generator.

In the early 1990s, the fixed speed wind turbines were most widely installed (Hansen & Hansen 2007) for their simplicity and low cost, because a power converter is not necessary to be incorporated in the system (Li & Chen 2008). However, in recent years, the SCIGs are increasingly being replaced by the more

efficient variable speed generators with power converters. The variable speed generator system is dominating the current wind turbine market. Power converters are now widely used to control the reactive power flow as a result of the cost of power semiconductor devices steadily decreasing at a rate of 2-5% per year (Blaabjerg & Chen 2006). Typically, variable speed generators are designed to operate either in a very narrow or a very broad speed range. The most commonly used narrow speed range generator system is the geared doubly-fed induction generator (DFIG) with a partial-scale (30% rated power) electrical power converter (Figure 2.6). The DFIG is an asynchronous machine that has both rotor windings and stator windings. The rotor windings are connected to a power converter through three slip rings. The rotational speed of the rotor can be controlled by the alternating current that passes into the rotor windings. The power converter connected to this machine is a partial-scale power electronic converter, which can control the variation in electrical frequencies. The range of the frequencies that can be controlled depends on the size of the converter (typically ±30% of the synchronous speed). The advantage of this type of converters is that only part of the generated power (typically 30% of the total generated power) passes through the converter allowing a smaller converter to be used.

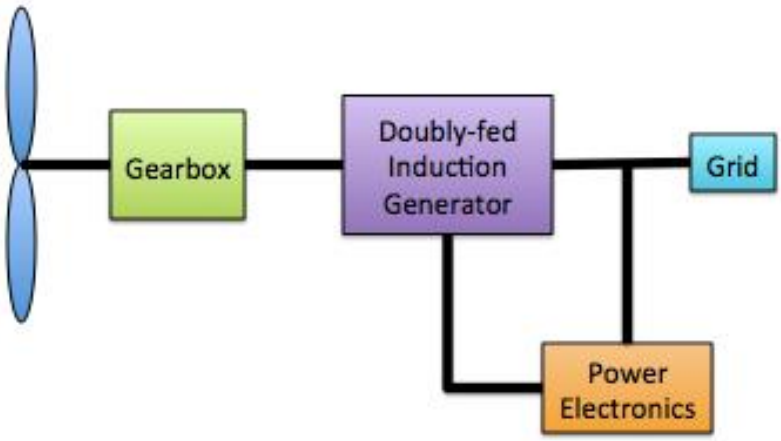


Figure 2.6: A variable speed wind turbine with a doubly-fed induction generator.

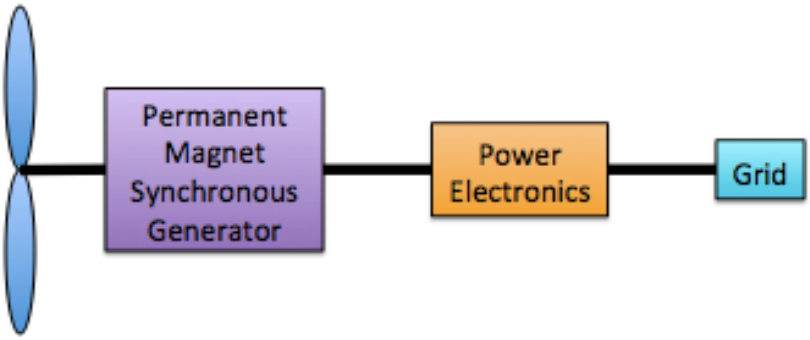


Figure 2.7: A variable speed wind turbine with a permanent magnet synchronous generator.

The most popular broad speed range generator system is the permanent magnet synchronous generator, which is used with a full-scale power converter (Figure 2.7). This generator system does not require a gearbox as the generator is designed to run at speeds comparable to that of the wind turbine rotor shaft. As the generator is directly connected to the grid through a power converter, a full-scale power converter is required to handle the rated power produced by the generator. Although the variable speed generator system is more complicated and

expensive, it is still more attractive than the fixed speed generator system due to: (1) its ability to capture more energy over a wider wind speed range; (2) better reactive power control as a power converter is used in the system; (3) lower mechanical fatigue on the turbine blades, gearbox and generator compared with the fixed speed system, as it allows electromagnetic torque variation produced by changes in wind speed (Zhang & Ula 2008; Li & Chen 2008). As it is widely accepted that the variable speed operation is more suitable for the wind turbine applications, this review will focus on the variable speed systems in the next section.

2.2.2 Geared vs direct-drive systems

A variable speed generator system can operate either with (geared) or without (direct-drive) a gearbox. Most of the wind turbine manufacturers adopt the geared variable speed wind turbine system, as it requires a smaller generator diameter. However, the gearbox of the variable speed generator system will have energy losses through heat dissipation and audible noise through friction between gears. Additionally, the gearbox requires frequent and regular maintenance throughout its lifetime, such as oil replacement. Four offshore wind farms (Barrow, North Hoyle, Scroby Sands and Kentish Flats) have reported that they experienced considerable gearbox bearing failure (Feng et al. 2010). In 2007, all 30 wind turbine gearboxes had bearing failure (WindPower 2007). In 2008, 20 wind turbine gearboxes required replacement to an upgraded version (Windpower 2008) and

the rest were replaced in 2009 (BBC 2009). From 2006 to 2008, the energy supplier in total spent £6,865,000 in operation and maintenance of wind turbine generators (Windpower 2008). Gearbox failure is often due to overheated oil. This could be resulted from a poor cooling system, blocked oil filters caused by metal powder produced from grinding wear, use of incompatible oil being refilled into gearbox, and imbalanced bearing movement resulted from wear and tear (Zhang 2005). The issues associated with gearbox damage and the long-term maintenance costs are major concerns for all wind farms using the geared wind turbine systems especially for the offshore ones.

A direct-drive wind turbine system, however, does not require a gearbox as the generator operates at the same speed as the wind turbine rotor. This can reduce the maintenance cost and downtime, hence improving the overall efficiency of the generator system over its lifetime. A direct-drive machine runs at low speed. To produce a high torque, a large generator diameter is required. This may create some transportation and installation difficulties, incurring more preliminary costs (Vries 2009). However, Siemens demonstrated that by replacing a 6 MW geared generator system with a direct-drive generator system, the generator system has 50% fewer parts and the towerhead mass is significantly reduced (Siemens 2012). A direct-drive wind turbine also requires a full-scale converter for variable speed operation and reactive power compensation. Full-scale converters typically cost up to three times more than partial-scale converters used in geared wind turbines.

However, falling prices in power electronic devices have made the use of direct-drive generator systems more appealing to many generator manufacturers (Blaabjerg & Chen 2006). The increase of power demand and the advancement of technology has shifted the wind turbine market trend to megawatt-scale standalone offshore wind turbines. Five out of ten of the top wind turbine manufacturers listed in Table 1.1 have started to invest in developing megawatt-scale direct-drive wind turbine generators.

Table 2.1: Top 10 wind turbine manufacturers of 2011, currently used generator concepts and power ranges (Cleantech Investor Ltd 2012; Vestas 2013; Sinovel 2013; Goldwind 2013; Gamesa 2013; Enercon 2013; General Electric 2013; Guodian United Power Technology Co. Ltd 2013; Siemens 2013; Ming Yang 2013; Suzlon 2013).

Manufacturer	Concept	Blades Diameter	Power Range
Vesta (Denmark)	DFIG DD PM	80-100 m 80-164 m	2-3 MW 2-8 MW
Sinovel (China)	DFIG	60-128 m	1.5-5 MW
Goldwind (China)	DD PM	70-100 m	1.5-2.5 MW
Gamesa (Spain)	DFIG GFC PM	52-97 m 128 m	850kW-2 MW 4.5-5 MW
Enercon (Germany)	DD EE	48-127 m	800kW-7.5 MW
GE Energy (USA)	DFIG GFC PM DD PM	70.5-82.5 m 100 m 110 m	1.5 MW 2.5 MW 4 MW
Suzlon (India)	FS	52-97 m	600kW-2.1 MW
Guodian United Power (China)	DFIG	77.36-100 m	1.5-3 MW
Siemens (Germany)	GFC IG DD PM	82-107 m 101-154 m	2.3-3.6 MW 3-6 MW
Ming Yang (China)	DFIG	77.1-82.6 m	1.5-2 MW

2.2.3 Electrically excited vs permanent magnet synchronous generator

A synchronous generator is widely used in the direct-drive variable speed generator systems. It consists of a magnetised rotor, which rotates at the same speed as the rotating magnetic field produced by a stator. The two types of synchronous generators are the electrically excited synchronous generator (electrically excited synchronous generator) and the permanent magnet synchronous generator.

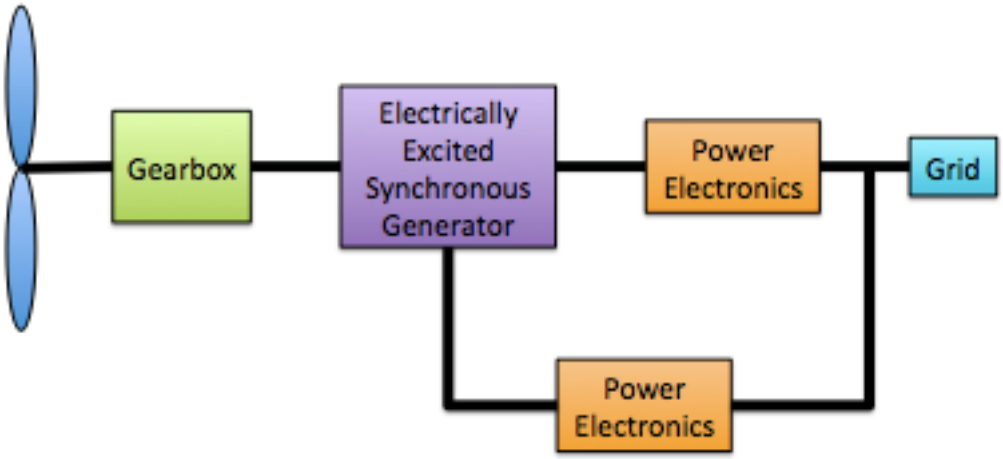


Figure 2.8: Schematic of electrically excited synchronous generator system.

An electrically excited synchronous generator consists of a rotor that is excited by direct current flowing in a field winding and a stator that has a three-phase winding. It is connected to two independent power converters, one for the rotor and the other for the stator (Figure 2.8). The power converter connected to the stator allows full control of the electric frequency, hence enabling the generator

speed to be controlled over a wide range, including at very low speeds. The other power converter connected to the rotor is used to control the excitation current; hence the flux can be controlled by the wind speed to reduce losses at different power ranges. In the mid-1990s, a direct-drive manufacturer (Enercon) based in Germany first produced this type of generators for the wind turbine applications. Currently, the largest electrically excited synchronous generator wind turbine is the Enercon E-126, which has a power rating of 7.5 MW (Veries 2012). The electrically excited synchronous generator does not require permanent magnets and thus the material cost is low. However, this machine is heavier and larger in size due to the use of large components such as the rotor excitation windings. Moreover, in order to excite the rotor windings with a direct current, slip rings and brushes, which require higher maintenances, are needed.

A permanent magnet synchronous generator uses permanent magnets to produce a magnetic flux in the air gap. The permanent magnet synchronous generator is more applicable than the electrically excited synchronous generator in the megawatt-scale direct-drive offshore wind turbine applications. This is because (1) permanent magnet synchronous generators can achieve higher energy yield and lower iron and copper losses, (2) it has higher power to weight ratio; and (3) higher reliability because no slip rings are needed (Bang et al. 2008; Li & Chen 2008; Polinder 2006). In 1980s, the high price of rare-earth magnets impeded the use of them on large-scale machines. In 1990s, the price of rare-earth permanent

magnets dropped steadily while the field strength of the magnets increased, enabling the large-scale adoption of the offshore permanent magnet synchronous generator wind turbines. However, in 2011, a sudden price rise happened when the largest suppliers, China (97% of rare-earth global market) restricted the resources to be exported. This resulted in the price increase by over 4 times in less than a year, leading to wind turbine manufacturers adjusting their design directions to other topologies. From 2012, the price of permanent magnets has slowly decreased. Walter (2012) predicted that there should be no price-jumps for the rare-earth materials for the first half of 2013. According to a comparative study (Polinder 2006), for a 3 MW variable speed wind turbine, the weight of using a permanent magnet synchronous generator is half of using an electrically excited synchronous generator. In addition, a permanent magnet synchronous generator has approximately 30% lower power losses than an electrically excited synchronous generator. However, the permanent magnet synchronous generator is more expensive. Secondly, the field strength of the permanent magnets cannot be varied. Demagnetisation of the permanent magnets can occur when the operating temperature rises above the Curie temperature, which depends on the properties of the magnet and the operating load line of the magnetic circuit (Negrea & Rosu 2001).

The permanent magnet synchronous generator can be categorised by the directions of the flux path in the generators. The three main categories according

to the directions of the flux path are the transverse flux, the radial flux and the axial flux.

A transverse flux permanent magnet machine produces a magnetic field in the direction that is perpendicular to the direction of movement and the direction of current flow. Although many researchers (Zavvos et al. 2012; Svechkarenko 2007; Bang et al. 2008; Bang et al. 2009) believe that the advantages of the transverse flux permanent magnet machines with high torque densities and low active materials cost are suitable for the direct-drive wind turbine applications. The transverse flux permanent magnet concept has not gained a foothold in the current wind turbine market due to the low power factor, the complex core design for manufacturing and assembly (Ivanovski 2011; Bang, Polinder, Shrestha, et al. 2008).

Radial flux permanent magnet machines produce a magnetic field in radial directions. Due to its simpler and more stable structure and lower manufacturing cost, most wind turbine manufacturers use radial flux permanent magnet generators for large-scale direct drive wind turbines. The radial flux machines with an outer rotor design are preferable for direct-drive application compared to the ones with an inner rotor design. This is because the outer rotor design has a higher torque density and the permanent magnet can be cooled by air more effectively (Chen et al. 2000). The manufacturers for the radial flux permanent magnet

machines include Vestas, Siemens, General Electric, and some others wind turbine manufacturers shown in Table 2.2.

Table 2.2: Large direct-drive wind turbines of different manufacturers with radial flux generator (Ivanovski 2011; Bang et al. 2008).

Generator Type	Power/Speed	Manufacturer
Electrically excited synchronous generator	4.5MW/13rpm	Enercon
Electrically excited synchronous generator	1.65MW/20rpm	MTorres
Permanent magnet synchronous generator	1.5(2)MW/18(23)rpm	Zephyros
Permanent magnet synchronous generator	2MW/24rpm	Mitsubishi
Permanent magnet synchronous generator	3.5MW/19rpm	Scanwind
Permanent magnet synchronous generator	1.5MW/23rpm	Leitwind
Permanent magnet synchronous generator	2.5MW/14.5(16)rpm	Vensys
Permanent magnet synchronous generator	1.5MW/19rpm	Goldwind

Axial flux permanent magnet machines have recently gained some interest in wind turbine applications. Some researchers have shown that, the axial flux permanent magnet machines can generate higher torque densities and require less core materials than the radial flux permanent magnet machines (Chen et al. 2004; Qu et al. 2003).

2.3 Axial flux permanent magnet machines

An axial flux permanent magnet machine is shaped like a disc or 'pancake' which produces a magnetic field in the axial direction. The axial flux machine can be designed with single, double or multiple air gaps (stacking machine). A single air gap axial flux machine is constructed either with a single stator or a single rotor. Due to the single-sided design, a force to balance rotor and a force to balance stator

is required to balance the magnetic forces. To increase the torque density, a dual air gap axial flux configuration was designed with two stators and a rotor (double-stator machine) or vice versa (double-rotor machine). This can generate high torque densities with a small outer diameter, and make better use of the active materials. For example, for a machine with 0.2 MW rated-power, a double-rotor slotted machine can double the torque density over a single-sided machine with rotor balance while having the outer diameter 27% smaller (Chen et al. 2004).

However, axial flux permanent magnet machines have larger diameters compared to a radial flux configuration. This is a major disadvantage of applying it to megawatt-scale wind turbines due to the difficulties this may bring in transportation and installation. In addition, axial flux permanent magnet machines have a higher structural weight in order to ensure small air gap clearance. Efforts have been made to reduce the outer diameter of axial flux permanent magnet machines by stacking multiple axial flux permanent magnet machines with low power ratings back-to-back. This approach increases the overall axial length without increasing the diameter, while each sub-machines can contribute to the total torque. This approach has shown to reduce the weight reported by Mueller et al. (2005). A two-stage axial flux machine with a rated machine torque of 1.26 MNm can lead to 16% rotor disc weight reduction.

The stators of axial flux permanent magnet machines can be designed with or without a core. As the reluctance of iron is lower than air, iron cores are used to guide more magnetic flux through to reduce the flux leakage. Cored machines can be divided into slotted and slotless. The main difference between these two core designs is the slotted machines have stator shoes, which the slotless machines do not have. This makes the slotless machines slightly lighter than the slotted ones. However, the slotless machines have larger air gap, so they will use more permanent magnets and copper windings to generate the same amount of magnetic flux (Sitapati 2001), and thus they will have higher lossess. According to Hanselman (2003), the copper losses of a 10 kW slotted axial flux machine were approximately 37.5% to 58% lower than those of a slotless axial flux machines. Cored machines will form a strong attractive force between iron cores and permanent magnets, hence requiring a stronger core structure to avoid closure of the air gap. This makes a cored machine much heavier in weight (Zavvos et al. 2012; Zhang et al. 2012).

In many different types of slotted axial flux permanent magnet machines, both studies conducted by Chen et al. (2004) and Hanselman (2003) concluded that the slotted axial flux permanent magnet machines with a double-rotor and single-stator design have the best overall performance. This type of machines has a higher torque density, lower copper and iron losses, a smaller total volume and a higher efficiency compared with other slotted axial flux permanent magnet machine

configurations. However, these machine designs may be too heavy for megawatt-scale wind turbine applications. Reducing the weight of a double rotor slotted machine is the key.

Ivanovski (2011) suggested that one way to reduce the weight of the electromagnetic materials is to make the magnetic flux path as short as possible. Woolmer (2009) introduced a Yokeless and Segmented Armature (YASA) machine with shorter magnetic flux paths. Although this may not be as light as a coreless machine, the permanent magnet can be used more effectively. In addition, the YASA configuration can make winding the copper an easier process and has a high winding factor. Therefore, investigation of the feasibility of applying a YASA machine for MW-scale wind turbine application is of great research interest.

2.4 Yokeless and segmented armature (YASA) machine

Yokeless and segmented armature (YASA) machine is a double-rotor single-stator slotted axial flux permanent magnet machine. The schematic is shown in Figure 2.9. A unique feature of YASA is that it has no stator yoke, and hence the stator teeth are mechanically and magnetically separated. The stator cores are held together with glass reinforced plastic (not included in the 3D model). The cross-section of such a machine is shown in Figure 2.10 and consists of two rotor discs each with magnets arranged circumferentially around the rotor plates with an opposite magnetic polarity on each rotor facing one another. A north magnet on

one disc faces a south magnet on the other disc so that the magnetic flux travels axially across the air-gap and then turns circumferentially into the stator core before returning to the rotors one pole pitch further on.

The open slot allows square wire to be wound directly onto the teeth and results in a high fill factor. The YASA stator teeth are made of a soft magnetic composite material (SMC), which can offer higher flexibility when manufacturing the segmented iron parts. In its original state, the iron is in powder form where each particle is coated with an electrical insulation compound. The insulation compound increased the resistivity and hence reduced machine eddy current losses. Stator core shapes can be easily produced by pressing the iron particles with a high pressure, therefore lowering manufacturing costs (Pinilla 2012; Chen & Pillay 2005).

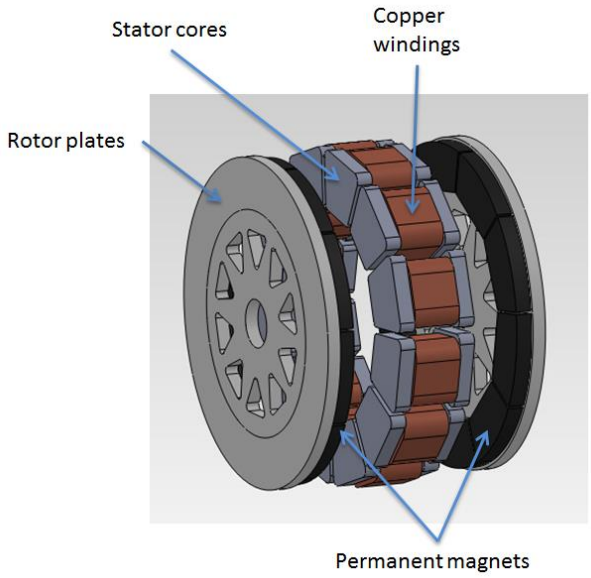


Figure 2.9: 3D model of 12 stator cores, 10 rotor poles YASA machine.

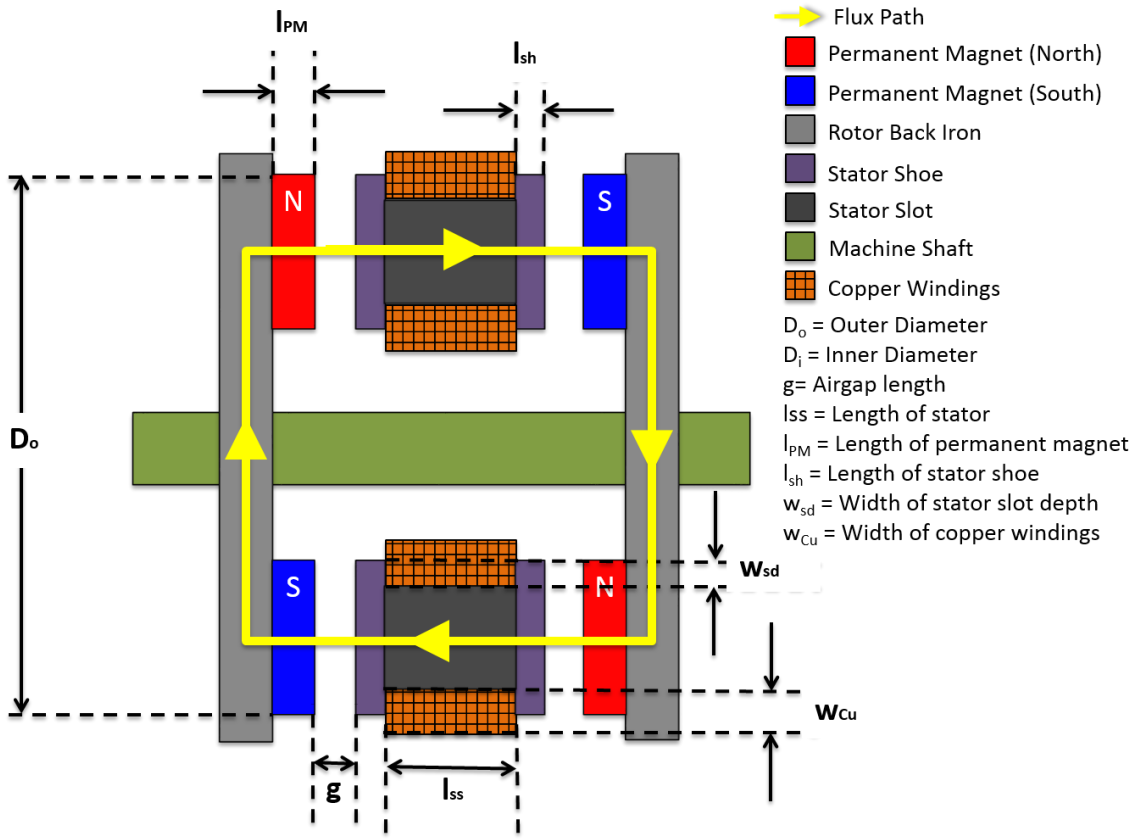


Figure 2.10: Cross section of the YASA machine.

In addition, a YASA machine was designed to have a cooling system allowing dielectric cooling fluid to be injected into the stator to directly cool down the copper coils (Woolmer 2010; R. Camilleri et al. 2012; Woolmer 2009). Woolmer (2009) stated that, the thermal resistances of YASA is approximately half of an axial flux generator with a standard cooling system using water as the coolant. This allows the YASA machine to run at higher current density with better thermal management ability.

The YASA topology was originally designed for vehicle propulsion applications where the power rating range is rated at 200 kW and below. Scaling

up the YASA machine for MW-scale wind turbine applications may pose a serious challenge in the generator electromagnetic, structural and thermal designs. The physical size and weight constraints are of concern for designing a MW-scale generator due to the space limited by the nacelle, and its impact on the transportation and the installation. Reducing the size using a multi-stage machine could be an option. However, this may increase the total weight and complexity of the structure. Currently, a YASA machine is 30% lighter and almost 50% smaller in volume than the best alternative axial flux machine (Woolmer 2009). With all these concerns, it is worth investigating in the first occasion a direct scale-up of the YASA machine.

Another possible issue for the scale-up is that the stator cores of the YASA machine was originally designed using SMC. SMC has many advantages (Chen & Pillay 2005) including: 1) the isotropic magnetic characteristics which can improve the machine performance; 2) the flexibility on shaping stator cores in more complex shapes and 3) it has lower eddy current loss due to the powder particles are coated with insulated layer to increase the resistivity; 4) more compact and higher torque per weight. However, SMC yields higher losses than traditional electrical steels, especially at low frequency. Figure 2.11and Figure 2.12 shows that at 50 Hz the core losses of SMC is 3-4 times higher than a low grade electrical steel (M400-50A). As a direct-drive generator operates at low frequency, using SMC may not be appropriate. An axial flux SMC prototype machine has 40% higher iron

losses than Bergey XL.1, a direct drive axial flux machine using laminating steel (Chen & Pillay 2005). Chen & Pillay (2005) conclude that direct replacement of electrical steel with SMC is not possible especially for machines with low frequency. In addition, SMC has relatively low permeability as shown in Figure 2.13.

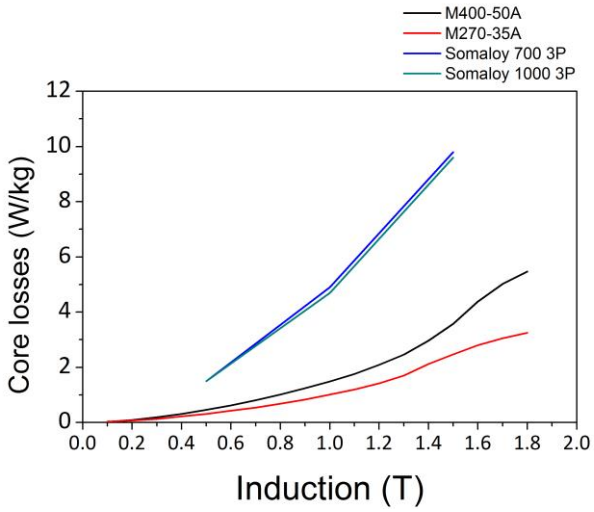


Figure 2.11: Material losses at 50 Hz as a function of induction.(Surahammmars Bruks AB 2013b; Höganäs AB 2013b; Höganäs AB 2013a)

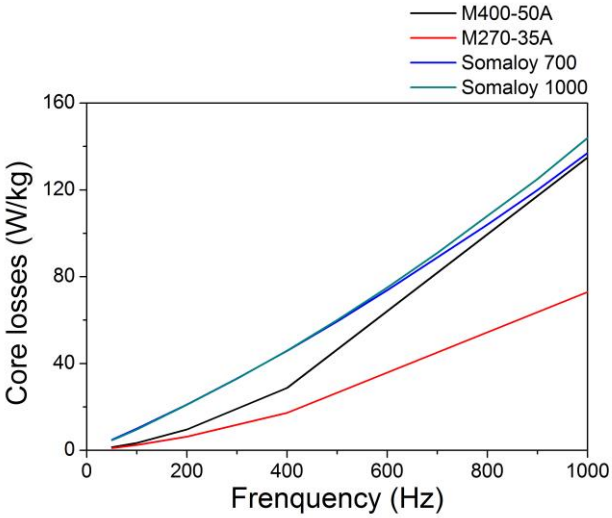


Figure 2.12: Material losses at 1 T as a function of frequency.(Surahammmars Bruks AB 2013b; Höganäs AB 2013b; Höganäs AB 2013a)

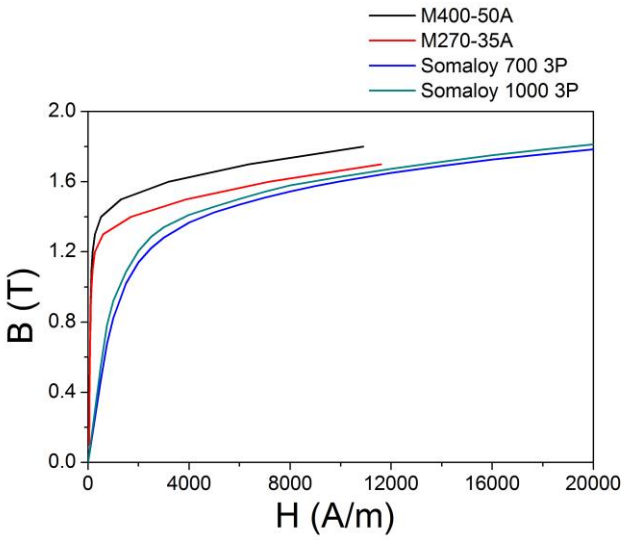


Figure 2.13: Comparison of the BH characteristics of two types of Somaloy™ 3P with two types of electrical steel.(Surahammmars Bruks AB 2013b; Höganäs AB 2013b; Höganäs AB 2013a)

Using laminated electrical steels to fabricate stator cores for a MW-scale generator is also a challenge. This is because the fabrication process requires high pressure and different sizes of laminations. Fei (2011) proposed a stator core design which stacks proportionally sized laminated electrical steel sheets together. This design is thought to increase the magnetic loading, mechanical strength, and reduce material cost and iron losses. (Fei and Luk 2009; Vansompel, Sergeant, Dupre, et al. 2012)

2.5 Methodologies for electrical machine design

This section reviews analytical and numerical methods used in electromagnetic, structural and thermal designs of permanent magnet synchronous machines.

The design process of permanent magnet synchronous machines can be generally divided into three stages: 1) analytical design, 2) numerical design and 3) building full-size or downscale prototypes for testing. The analytical method is often used in the first stage of a machine design process. This is a relatively fast process and is extremely useful to generate preliminary machine data. It requires low computing resource and design time. However, the results are approximate and assumptions are made to facilitate the calculations. It also generates a vast amount of possibilities, and therefore, a good optimisation tool should be integrated to reduce the design space for further analysis using FEM. FEM is time consuming and requires heavy computing power if good accuracy is required. The FEM results can be used to verify the analytical results and hence further adjustment can be made to optimise design parameters to achieve the design requirements. It also takes into account of the details of complex geometries and material properties in a 3-dimensional space to solve either steady-state or transient conditions. Once the FEM simulation has been carried out, a machine prototype can be built based on the FEM model for validation.

2.5.1 Electromagnetic design

In this section, two of the most popular analytical methods for the electromagnetic design of a generator are discussed. The two methods are the equivalent circuit method and the analytical design equations (sizing equations)

method. Finite element analysis can be applied to validate the analytical calculations and offer further optimisation.

2.5.1.1 Equivalent circuit-based design

The magnetic equivalent circuit (MEC) method builds a non-linear reluctance network to analyse the flux densities in different components of an electrical machine (Perho 2002; Rasmussen & Ritchie 1997). This method can be used to model non-linear magnetic fields in an electrical machine under steady state or dynamic conditions. The results between MEC and FEM have shown to be within 5% (Yilmaz & Krein 2008). MEC has been adapted to model the axial flux machine topologies (Figure 2.14). R_s, R_y, R_g and R_t in Figure 2.14 are equivalent reluctances representing the magnetomotive force (MMF) drop on the stator shoes, the stator yokes, the air gaps and the stator teeth. F_{PM} and F_I are the MMF produced by the permanent magnet and the stator current. Equations are derived to calculate the contribution from each reluctance element. Tangudu et al. (2009) applied MEC to a more complex fractional slot concentrated winding interior permanent magnet machine. The authors claim that MEC can significantly reduce the calculation time compared with FEM as it can incorporate air gap modelling which can eliminate the need of rebuilding the stator and rotor models while the rotor moves.

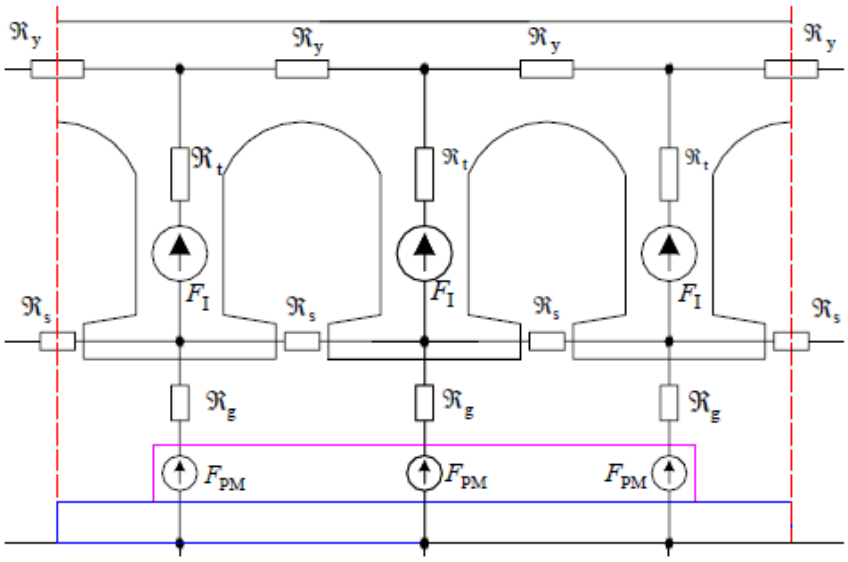


Figure 2.14: Magnetic equivalent circuit of the axial flux permanent magnet machine (Parviainen 2005).

Magnetic equivalent circuit is accurate to estimate the maximum flux density levels under either loaded or no load situation and can consider a material's saturation effect. However, it can only be applied to the designs with known dimensions.

2.5.1.2 Analytical design equations

The second analytical design method uses sizing equations derived for different types of machine topologies (Espanet et al. 2003; N. Bianchi et al. 2006; Bianchi et al. 2003; Honsinger 1987; Soong 2008; Huang et al. 1999; Huang et al. 1998). Specifically, Woolmer & McCulloch (2007)and Woolmer (2009) have applied the sizing equations to design the YASA topology. These sets of equations can calculate the machine dimensions, by considering the magnetic and electrical properties such as the saturation flux density of magnetic materials, the current

density and the current loading of a machine. It is also a very useful tool to compare performance of different types of electrical machine topologies (Huang et al. 1998).

Another advantage of this method is that optimisation algorithms can be integrated into the calculation, which can greatly reduce the search area of designs for the finite element analysis. However, this is also the challenge of this method as it can generate a huge number of design variables. Optimising all these variables at once is a difficult task and often become a dilemma. A rational analytical design approach is first using sizing equations to generate machine dimensions, followed by applying them to create a MEC network to calculate performance data.

2.5.1.3 Finite element methods (FEM)

Finite element analysis is a numerical method to solve partial differential or integral equations (Pelosi 2007; Ferrari 2007). The idea of this method is to divide a complicated geometry into a finite number of discrete shapes of small elements, called finite elements that can be solved in relation to each other. The finite element analysis allows modelling electrical machines with complicated geometries and with non-linear materials either in 2-D or 3-D. This can give an accurate result without considering many restricting assumptions as often used in an analytical method. The main considerations and covering equations for the finite element method are reported in Silvester & Ferrari (1996) and Gieras (1997).

The finite element methods are used widely in the design process of electrical machines, especially in large-scale wind turbine generators (Chen, Nayar, & Xu, 2000; Mardaneh et al., 2006; Marignetti, Colli, & Coia, 2008; Matsumoto, Shimomura, & Morimoto, 2010; Toliyat, Moreira, & Harbor, 1999). This is because the finite element analysis can calculate the characteristics of the electrical machine that would historically have been determined in prototype testing and from there the result gives guidance on what to expect in testing, where to look and what range of output to cater for. It also gives insight into effects that would have previously been impossible to identify. Most importantly, using finite element method can reduce the cost by simulating the generator model on a computer instead of building an expensive prototype for field tests (Gupta et al. 2009).

Marignetti et al. (2008) claims that axial flux machines require 3-D finite element modelling in order to simulate their intrinsically 3-D electromagnetic behaviour. Caricchi et al.(1998) modelled an axial flux machine with 2-D finite-element method but only consider the performance on the average radius of the machine which may not be sufficient to compute the results with high accuracy. Vansompel et al.(2012) proposed a 2.5-D FEM by combining multilayers 2-D model solutions to compute the performance of an axial flux machine and claims that it is less time consuming than the 3-D finite element method. However, this method has assumed no radial component of flux flows in the machine which will affect

the accuracy of the solutions. Therefore, 3-D FEM modelling is a more accurate method to design the electromagnetic aspects of axial flux machines.

The downside of FEM is that the preparation time and computational time may take long for simulating a large-scale machine. Like MEC, it can only be used to parameterise the machine dimensions with multiple runs.

2.5.2 Structural design

For a preliminary design of the structure of an electrical machine, rapid results with a reasonable level of confidence is important to predict the minimum volume of materials needed to fulfill the mechanical requirements. Finite element method is then used for validation and further optimisation by considering the 3-D properties of the materials and also the geometries of the machine.

2.5.2.1 Roark's formulas

In the preliminary design process of an electrical machine, complex machine geometries are often simplified as circular plates, elastic beams and cylindrical shells, which the structural properties can be analysed through the well-established Roark's formula (Young & Budynas 1938). This has been applied to design an axial flux machine by Mueller et al. (2005) in the design of rotor plates, stator plates and a beam structure to hold a stator. Crozier and Mueller (2012) has further used the method to design a direct-drive linear machine to harness wave energy. This method is very useful in estimating the structural weight of a machine

(Mcdonald et al. 2008). As at MW-scale, structural mass has taken a large portion of the total mass of a generator, which will affect the decision on machine optimisation.

The analytical method with Roark's formula can give indication of the machine size and the structural weight at an early stage in a short time. However, this method is only capable of calculating models with simple geometries. The applied stress on each component can only be analysed separately and hence the accuracy is low when it is used to consider the whole machine and the forces altogether.

2.5.2.2 Finite element method

Finite element method are more commonly used in the structural design of electrical machines, especially for structural optimisation (Roy & Whitcomb 1997; Chen & Lv 2010; Bang, Polinder, G. Shrestha, et al. 2008). This method is especially useful when designing a large scale machine when building the prototype to test is expensive (Keysan et al. 2011; Bang, Polinder, G. Shrestha, et al. 2008). A structural simulation is generally fast based on the current state of the computer. However, when a high accuracy simulation is needed and a machine size is large, a large number of meshes will increase the computational time significantly.

2.5.3 Thermal analysis

Thermal analysis of an electrical machine is usually performed using lumped system analysis and finite volume methods. In lumped system analysis, a network of nodes representing each machine component connected by resistances. A node is treated as a heat source if it represents components like windings or stator cores which generate heat. An example of the lumped parameter thermal network of an axial flux machine developed by Rostami et al. (2011) is shown in Figure 2.15. The benefit of the lumped circuit is that it is very fast to calculate, although developing this network model is a demanding task (Boglietti et al. 2009; Gorginpour et al. 2014) . An important parameter in thermal analysis is the heat transfer coefficient. These are either assumed or estimated using published data, which could have substantial deviations. However, Mellor (1991) and Di Gerlando (1994) believe that the influence of these deviations on the final results may be small.

Lumped circuit analysis is also a fast technique without heavy computing work. However, each node is treated to have a constant temperature. Although components can be further divided into smaller section to improve resolution and provide a greater detail. However, the complexity of the model increases rapidly with increasing number of nodes. In this case, a numerical method may be more desired.

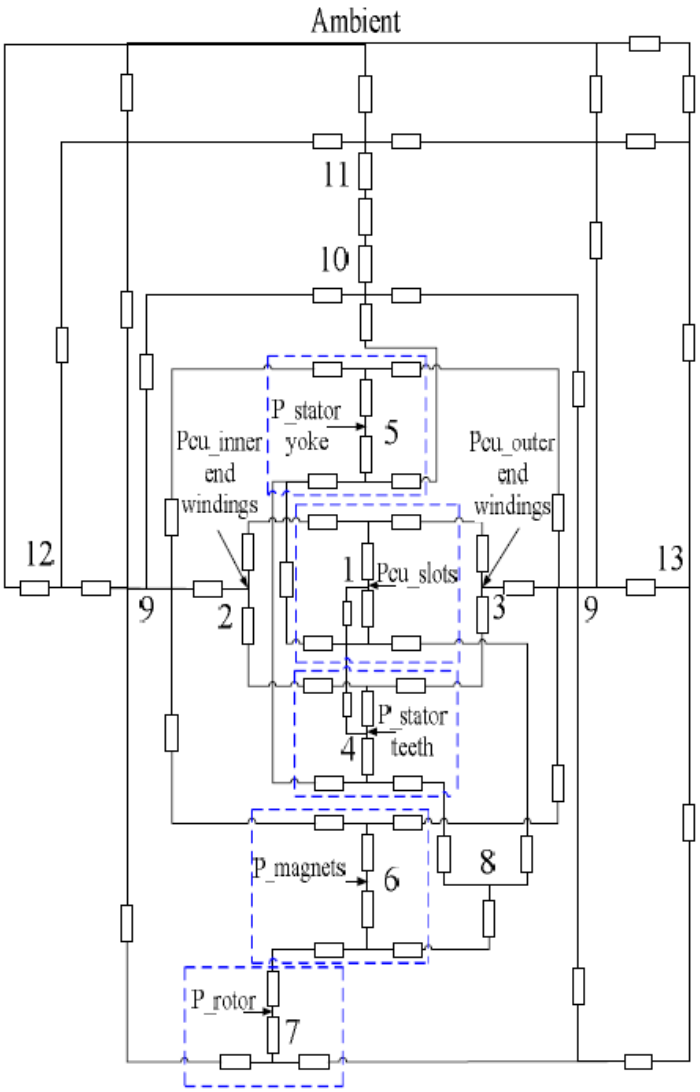


Figure 2.15:Lumped parameter thermal network of an axial flux machine. (Rostami et al. 2012)

2.5.3.1 Finite volume method

The computational method that can predict the convective heat transfer coefficients over surfaces is computational fluid dynamics (CFD). The CFD usually employs a finite volume method (FVM) to represent and evaluate partial differential equations in the form of algebraic equations (LeVeque 2004). This method has been widely used in thermal analysis for electrical machines (Lim et

al. 2011; Odvárˇka et al. 2010). Like FEM, FVM also requires high computational time and therefore, it is preferred to investigate small components of a machine (such a section of a rotor or a stator) rather than the whole machine model (Howey et al. 2012; Hey et al. 2010; Lim et al. 2011; Odvárˇka et al. 2010). Although there are still some researchers modelling a small-scale machine in full (Maynes et al. 2003; Liao et al. 1999), crude modelling assumptions were used such as using non-thermally conductive materials to represent the end windings.

2.6 Summary

This chapter reviews different generator topologies for wind turbine applications by comparing the fixed and variable speed, the gear and direct drive, as well as the electrically excited and permanent magnet generator systems. The success of applying an axial flux YASA for electric vehicles motivated this project on scaling up the YASA topology to a MW-scale generator.

Designing a new electrical machine should be approached from three aspects: electromagnetic, structural and thermal. Each aspect can be designed using both analytical and finite element methods. Analytical method is a fast and approximate, while the FEM is more accurate but demands good computational resources. The strategy to design a MW-scale machine should be combining both methods by using analytical method to reduce the design space, followed by the FEM. An optimisation tool is also useful to determine a design optimum.

Chapter 3 – Analytical Design Methods

This chapter develops an analytical tool for designing a MW-scale YASA generator. Although analytical calculation is an approximate approach to generate preliminary machine data, it effectively reduces the number of designs required for a more detailed design procedure using the FEM. In the analytical tool, the electromagnetic aspect of the machine is designed using sizing equations. Roark's formulas are used for structural design. Different designs that provide similar performance will have emerged from the analytical process. However, there may be an advantage of one design over another. Therefore, an optimisation process was applied to determine a design optimum. This optimal YASA machine design was used to compare directly with other machine topologies such as radial flux and transverse flux permanent magnet machines. This provides knowledge of the benefits of the YASA topology and what other machine parameters require further optimisation. The winding design is also considered for a 100 pole and 120 stator core YASA machine. Finally, analytical methods were also used to generate waveforms of air gap flux density, back EMF, and cogging torque. These results are subject to validation with FEM in the next chapter.

3.1 Analytical design tool

Figure 3.1 shows the process flow of a proposed analytical design tool containing the electromagnetic and structural designs of a generator, followed by an optimisation process to determine an optimised machine design.

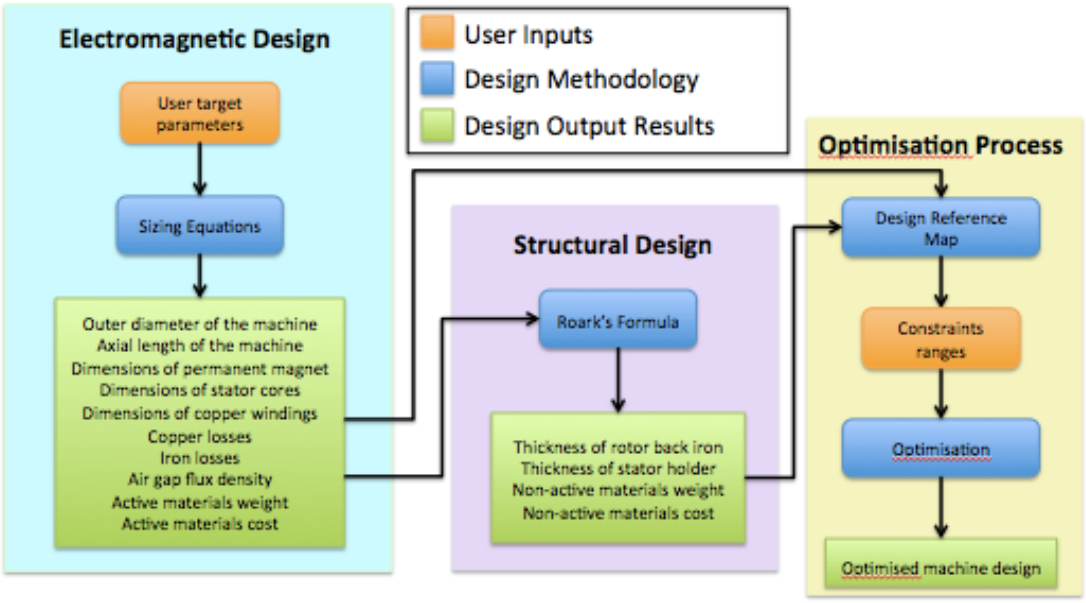


Figure 3.1: Flow diagram of the analytical design tool

In the electromagnetic design, the user target parameters are the rated power and the rotational speed. These were input in sizing equations, which can calculate the dimensions and the power losses as a function of the air gap flux density, the outer-to-inner diameter ratio and the current loading. The structural design with Roark's formula can thereafter be initiated once the electromagnetic parameters are determined. The structural design is essential to prevent a machine from mechanical failure, to maintain performance, and to achieve a high power-

to-weight ratio. Mechanical failure and reduction in electromagnetic performance could be caused by rotor deflection due to the attractive force between permanent magnets and stator cores. A high power-to-weight ratio can be achieved by reducing the structural weight of a machine, as it could take up to 90% of the total weight of a MW-scale generator (Mueller et al. 2005). In this case, the main objective of the structural design is to reduce the weight of the rotor plates.

In the optimisation process, a design reference map is produced using the calculated electromagnetic and structural parameters. This is a graphical presentation of the relationships between different machine parameters. It facilitates designers to determine an appropriate constraint range based on the application requirements. However, these machine parameters are often in conflict and compromises have to be made in order to optimise one or more parameters. Therefore, it is useful to have a flexible multi-objective optimisation tool, which designers can decide which parameters are more important than the others for their applications. In light of this, an optimisation tool using pseudo-weight vector approach is developed. It allows designers to place more weights on one or a few objectives to increase their levels of priority. This method is applied for the first time in machine designs. The design objectives considered in this study are: 1) to minimise the outer diameter; 2) to minimise the weight of the machine; 3) to minimise the copper and iron losses; 4) to minimise the amount of the permanent magnets and 5) to minimise the cost.

3.2 Electromagnetic Design

3.2.1 Sizing equations

Sizing equations (3.1-3.23) were developed by Huang et al. (1998; 1999) and modified by Woolmer (2009) to apply to the YASA generator.

The rated power of the machine is given by,

$$P = \frac{m}{m_1}\frac{\pi^2}{4} k_e k_i k_p B_g A_s \frac{f_e}{p}(1 - {k_d}^2)\frac{1 + k_d}{2}{D_o}^3 \qquad (3.1)$$

where m is the number of phases, m_1 is the number of phases of each stator (in this case $m_1=m$, as it is a single stator machine), k_e is the EMF factor which incorporates the winding distribution factor and the pitching factor, k_i is the current waveform factor, k_p is the electrical power waveform factor, B_g is the air gap flux density, A_s is the current loading, f_e is the electrical frequency, p is the number of pole pairs, k_d is the ratio of inner to outer diameter and D_o is the outer diameter of the generator.

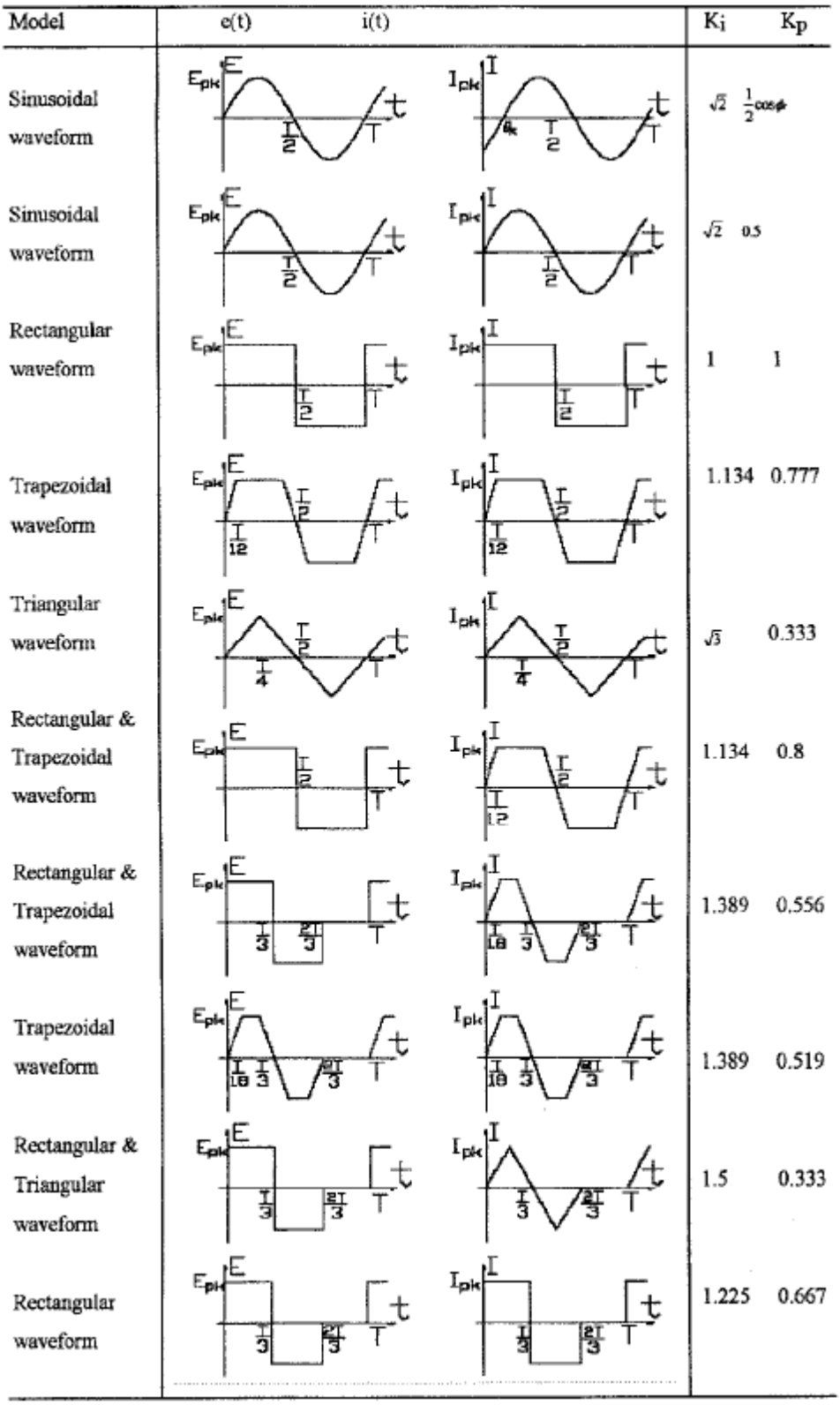


Figure 3.2: Typical prototype waveforms (Adapted from (Huang et al. 1998)).

A_s is given by,

$$A_s = \frac{2m_1 N_{ph} I_{rms}}{\pi D_o \frac{1+k_d}{2}} \tag{3.2}$$

where N_{ph} is the number of turns per phase and I_{rms} is the root mean square current.

D_o can be re-arranged from equation (3.1),

$$D_o = \left(\frac{T}{\frac{m}{m_1}\frac{\pi}{8} k_e k_i k_p B_g A_s (1-k_d{}^2) \frac{1+k_d}{2}} \right)^{1/3} \tag{3.3}$$

The total outer diameter of the YASA machine is estimated as:

$$D_{tot} = D_o + 2w_{sd} \tag{3.4}$$

where w_{sd} is slot depth.

The total effective length of the machine is equivalent to the sum of the axial length of the different parts of an axial flux machine as shown in Figure 3.3. It can be written as,

$$l_e = 2l_{ss} + 2l_{sh} + 2g + 2l_{PM} + 2l_{BI} \tag{3.5}$$

where l_{ss} is the length of the stator slot, l_{sh} is the length of the stator shoe, g is the air-gap length, l_{PM} is the length of the permanent magnet and l_{BI} is the length of the back iron. These lengths will be calculated later in equations (3.9), (3.12) and (3.14) respectively.

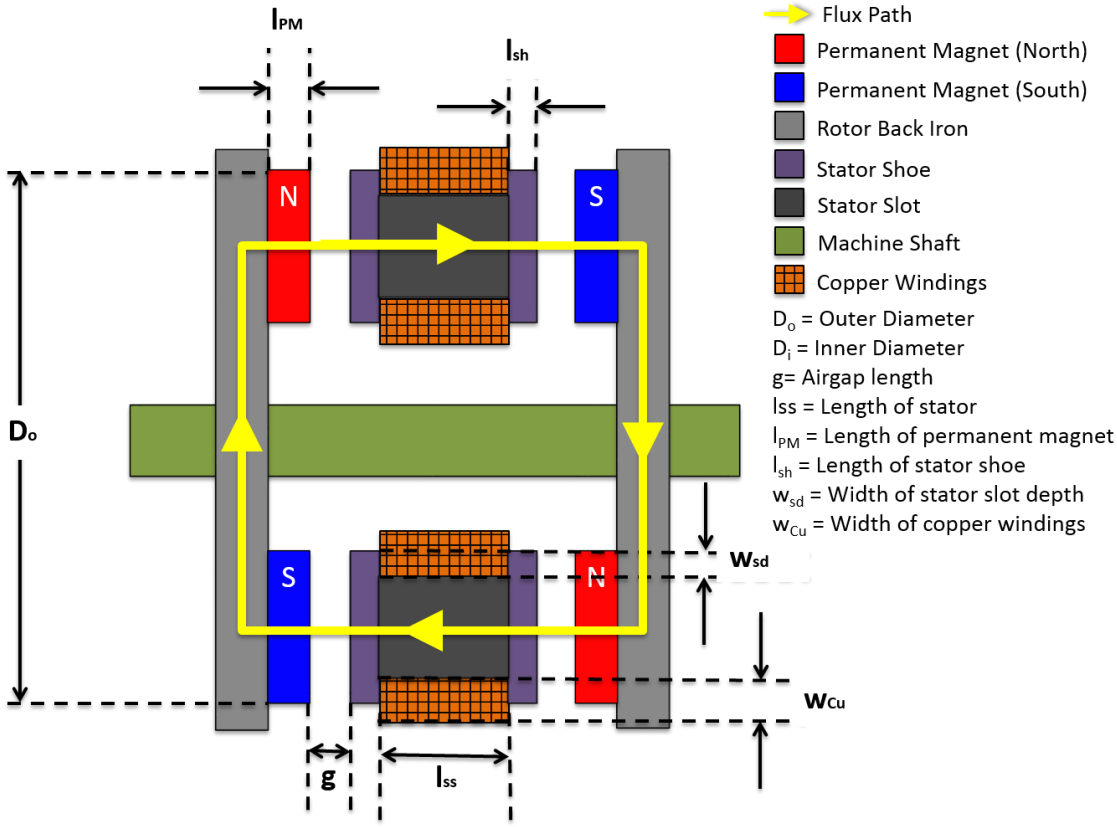


Figure 3.3 Side view of the YASA machine. Adapted from (Woolmer 2009).

The total active material weight is given by,

$$W_{act} = 2W_t + 2W_{sh} + 2W_{PM} + 2W_{BI} + 2W_{Cu} \tag{3.6}$$

where W_t is the weight of the stator teeth, W_{sh} is the weight of a stator shoes at one end of the stator teeth, W_{PM} is the weight of the permanent magnet, W_{BI} is the weight of the back iron and W_{Cu} is the weight of the copper coil on one set of the stator teeth.

The depth of copper w_{Cu} is required to find W_{Cu} and it can be described by,

$$w_{Cu} = \frac{\pi D_o(1+k_d)}{4Q}\frac{B_t\alpha_t - B_t\alpha_t\alpha_{cg} - B_g}{B_t} \tag{3.7}$$

where B_t is the maximum flux density which is allowed in the stator teeth and B_g is the average air gap flux density, α_t is the ratio of the reduction in the flux density due to the radii corner added to reduce the end winding and the leakage inductance, while in this analysis, the α_t is assumed at 0.9. α_{cg} is the gap between the coils to improved thermal conductivity between the copper and iron core and it is assumed at 0.05 for cooling purpose. Q is the number of slots of the machine and for YASA, the slot depth is equal to,

$$w_{sd} = \frac{\pi D_o(1+k_d)}{4Q}\frac{B_t\alpha_{sh}\alpha_t - B_g}{B_t\alpha_t} \tag{3.8}$$

where α_{sh} is the ratio between the arc of the shoes and the stator pole pitch and assumed at 0.9 in this analysis.

The length of the stator slots is,

$$l_{ss} = \frac{A_s}{2k_f J_{rms}} \frac{\pi D_o}{2Q w_{Cu}} \frac{1+k_d}{2} \tag{3.9}$$

where J_{rms} is the RMS current density, and k_f represents the fill factor of the stator. A typical range of the current density for a wind generator is between 3×10^6 and 6×10^6 A/m^2 (Li et al. 2009; Toliyat & Kliman 2004). The current density is limited by the thermal limits of the insulator and the permanent magnets. In this study, the highest value 6×10^6 A/m^2 is considered and whether this value can be achieved will be considered in conjunction with the thermal study in Chapter 6. A YASA topology can achieve a fill factor of 0.8 (Woolmer 2009) as the slots are entirely open and square or tape wire is used.

The average width of the shoe is given by,

$$w_{sh} = \frac{\pi(1+k_d)D_o\alpha_{sh}}{2Q} \tag{3.10}$$

The weight of the stator teeth can be expressed by,

$$W_t = \rho_{smc} Q l_{ss} \alpha_t (w_{sh} - 2w_{sd}) \frac{D_o}{2} (1 - k_d) \tag{3.11}$$

where ρ_{smc} is the density of the iron.

The length of the shoes for each topology,

$$l_{sh} = \frac{B_g w_{sd}}{B_{sh}} \tag{3.12}$$

where B_{sh} is the maximum flux density which is allowed in the stator shoe.

The weight of the shoes on the end of one set of stator teeth can subsequently be estimated,

$$W_{sh} = Q \rho_{smc} l_{sh} \alpha_{sh} w_{sh} \frac{D_o}{2} (1 - k_d) \tag{3.13}$$

The length of the magnet,

$$l_{PM} = \frac{\mu_r B_g g k_r}{k_l B_r - \frac{B_g}{C_\phi}} \tag{3.14}$$

where μ_r is the recoil permeability, k_r is the magnetic path reluctance factor which is typically $1<k_r\leq1.2$, k_l is the leakage factor, which is normally $0.9\leq k_l<1$, B_r is the remanence flux density of the permanent magnets, C_Φ is the magnet

concentration factor equal to A_m/A_g (Hanselman 2003), A_m is the surface area of the permanent magnet and A_g is the surface area of the air gap.

The average width of the permanent magnets,

$$w_{PM} = \frac{\pi(1+k_d)D_o\alpha_p}{4p} \tag{3.15}$$

where α_p is the ratio between the magnetic arc and the magnetic pole arc, which is 180°e. In this analysis α_p is assumed to be 1.

The mass of the permanent magnets can be defined by,

$$W_{PM} = \rho_{PM} l_{PM} \alpha_p \pi \frac{D_o^{\,2}}{4}(1-k_d^{\,2}) \tag{3.16}$$

where ρ_{PM} is the density of the permanent magnet.

The length of the back iron can be expressed by,

$$l_{BI} = \frac{\pi D_o}{4p}\frac{1+k_d}{2}\frac{B_g}{B_{BI}} \tag{3.17}$$

where B_{BI} is the maximum flux density of the rotor back iron.

The mass of the rotor back iron can be written as,

$$W_{BI} = \rho_{ms} l_{BI} \frac{{D_o}^2}{4} \left(1 - {k_d}^2\right) \tag{3.18}$$

where ρ_{ms} is the density of mild steel.

Iron losses and copper losses are two major power losses. Other losses such as mechanical losses are insignificant in comparison and not considered in this analysis for simplicity.

The total volume of the copper can be estimated by:

$$V_{Cu} = l_{turn} w_{Cu} 2 l_{ss} k_f \tag{3.19}$$

where l_{turn} is the average length of one turn of the copper coil, and

$$l_{turn} = 2l_{act} + l_{endi} + l_{endo} \tag{3.20}$$

Each turn includes the active copper l_{act}, the outer end-windings l_{endo}, and the inner end-windings l_{endi}. These windings lengths can be derived as the followings,

$$l_{act} = \frac{1}{2} D_o (1 - k_d) \tag{3.21}$$

$$l_{endo} = \frac{\pi (D_o + w_{Cu})}{Q} \tag{3.22}$$

$$l_{endi} = \frac{\pi(k_d D_o - w_{Cu})}{Q} \tag{3.23}$$

3.2.2 Estimation of power losses

By knowing the machine dimensions, the copper losses and the iron losses can be calculated. The copper losses are defined by,

$$P_{Cu} = J_{rms}{}^2 r_{Cu} V_{Cu} \tag{3.24}$$

where r_{Cu} is the resistivity of copper (Table 3.1).

The weight of the copper used can be expressed by,

$$W_{Cu} = Q\rho_{Cu} l_{ss} l_{turn} w_{Cu} k_f \tag{3.25}$$

where ρ_{Cu} is the density of copper (Table 3.).

The weight of the iron used can be estimated by,

$$W_{Fe} = 2W_{sh} + 2W_t + 2W_{BI} \tag{3.26}$$

The iron losses of a YASA machine occur in the stator cores. This is dependent on the magnetic flux density in the stator core, which is affected by the load condition. As different magnetic flux densities are allowed to pass through

the stator tooth and shoe, hence they are calculated separately. The iron losses can be expressed by (Pyrhnen et al. 2008),

$$P_{Fe} = 2W_{sh}P_{ES}\frac{f_e}{f_0}\frac{\hat{B}_{sh}}{\hat{B}_0} + 2W_tP_{ES}\frac{f_e}{f_0}\frac{\hat{B}_t}{\hat{B}_0} \tag{3.27}$$

where P_{ES} is the electrical steel iron loss per mass at a given angular frequency f_0 and flux density B_0, f_e is the frequency of the field in the stator iron. The stator core of the 1 MW YASA model is made of electrical steel M270-35A. The 50 kW YASA prototype has the stator cores made of soft magnetic composite (Somaloy 500). The *B-H* curves of these materials are shown in Figure 2.13 in the previous chapter. Each of these magnetic materials has its own maximum saturation point of flux densities. The saturation point of the electrical steel, M270-35A, is around 2.35 T (Adcock 2012) and the saturation point of the soft magnetic composite, Somaloy 500, is around 2 T (Höganäs AB 2013b). If the flux densities of the magnetic materials are saturated, the machine will have more eddy current and hysteresis losses. Therefore, it is necessary to maintain the flux density passing through the magnetic materials within the non-saturation region. The value of P_{ES} of this material is equal to 2.47 W/kg at 1.5 T and 50 Hz (Figure 2.11).

*Table 3.1: Generator material characteristics *(Bang & Polinder 2010)* **(Surahammmars Bruks AB 2013a)****(Pompermaier et al. 2012)* *****(The Engineering Toolbox 2014b).*

Parameter	Symbol	Value	Unit
Density of iron	ρ_{fe}	7800*	kg/m^3
Density of soft magnetic material	ρ_{smc}	7600**	kg/m^3
Density of permanent magnet	ρ_{PM}	7600*	kg/m^3
Density of copper	ρ_{Cu}	8900*	kg/m^3
Core loss of SMC (Somaloy 700)	P_{smc}	8.4***	W/kg
Resistivity of Copper at 20°C (ohm m)	$r_{Cu(20)}$	0.017****	μΩ m
Resistivity of Copper at 155°C (ohm m)	r_{Cu}	0.027	μΩ m

3.2.3 Cost of active materials

The cost of a generator is an important issue, which may deter whether a topology would be adopted for wind turbines. Estimating the total cost is a complex study, in which costs of manufacturing, labour, materials and transportation need to be considered. Of all, the cost of active materials (iron, copper and permanent magnet) takes a large percentage. To optimise a generator topology, the cost of the active materials should be minimised for a given power. The price per kilogram of each active material is listed in Table 3.2. From the table, it can be observed that the cost of the permanent magnet is the dominator of the cost. The total cost of the active materials can be derived by:

$$C_{act} = C_{smc}W_{smc} + C_{Cu}W_{Cu} + C_{PM}W_{PM} + C_{ms}W_{ms} \quad (3.28)$$

Table 3.2:Machine materials costs (Li et al. 2009).

Cost models	Price per kg (€/kg)
Iron core cost	3 €/kg
Copper cost	15 €/kg
Permanent Magnet	40 €/kg

3.2.4 Validation of the sizing equations

The sizing equations for the YASA machine are validated by comparing the calculated results with the dimension of an existing 120 Nm YASA prototype machine built in the EPG laboratory. The model is generated by inputting the same B_g and k_d values as those of the existing YASA machine. The dimensions of the calculated design shown in Table 3.3 have errors within 20% from those of the prototype machine, apart from w_{Cu} and l_{BI}. The w_{cu} is high because the outer diameter is larger than that of the prototype machine and also because the α_{cg} assumed in the analysis is slightly lower compared with the prototype.

For a preliminary analytical design, these percentages of error are expected, as the sizing equations do not consider the geometry of the generator and the ratio of the gaps between the permanent magnets and the stator cores. These will be resolved in next chapter with the finite element method.

Table 3.3: Comparison between the analytical results and the measured results.

Parameters	Analytical result (with same B_g and k_d values as the existing machine)	Existing 50kW YASA prototype	Precentage of error
Outer diameter, D_o	206.5 mm	204 mm	1.23%
Depth of permanent magnet, d_{PM}	32.3 mm	31.9 mm	1.25%
Stator winding slot width,w_{Cu}	5.6 mm	5.8 mm	3.45%
Length of stator bar, l_{ss}	18.2 mm	15 mm	21.3%
Length of stator shoe, l_{sh}	2.4 mm	5 mm	52%
Length of permanent magnet, l_{PM}	8.4 mm	10 mm	16%
Length of rotor back iron, l_{BI}	13.7 mm	9 mm	52.2%
Maximum air gap flux density, B_g	0.95 T	0.95 T	-

3.3 Structural design

The aim of this section is to investigate the minimum thickness of a rotor back iron that can avoid over-deflection. The method used in this study is based on the circular plate theory of Roark's formula that were introduced by Roark (1932). This method has been adapted in many circular plates with different stress applied situations (Young, Warren C., Budynas 2002). In addition, it has also been used in the structural design of axial flux machines by Mueller et al. (2005) and Polinder (2008). In our calculation, the rotor back iron is simplified as a flat circular plate without using reinforcement.

3.3.1 Roark's formula approach

The Roark's formula approach to design YASA generators is described as follows.

The magnetic attractive forces, F_{PM} which is the force between the rotor and the stator is given by,

$$F_{PM} = \frac{B_g^{\,2}}{2\mu_0} S_{PM} \tag{3.29}$$

where B_g is the air gap flux density, μ_0 is the permeability of free space and S_{PM} is the active surface area of all permanent magnets (single-sided machine).

The magnetic pressure, q, is given by,

$$q = \frac{F_{PM}}{S_{PM}} = \frac{B_g^{\,2}}{2\mu_0} \tag{3.30}$$

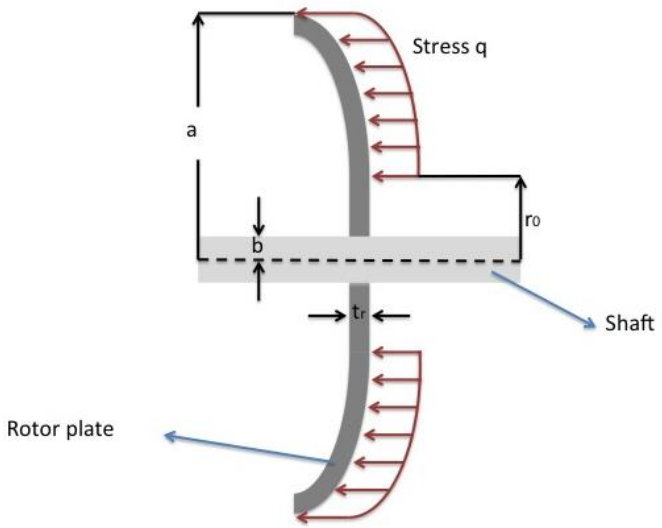


Figure 3.4: Circular plate models. Re-adapted from (Mueller et al. 2005)

The stress applied to the circular plate is shown in Figure 3.4. The normal stress of the rotor disc is uniformly distributed along the rotor plate apart from the

centre of the shaft to r_o (the starting point of the stress applied). The deflection, y_a, of the rotor disc is given by,

$$y_a = M_{rb}\frac{a^2}{D}C_2 + Q_b\frac{a^3}{D}C_3 - \frac{qa^4}{D}L_{11} \tag{3.31}$$

where M_{rb} is the unit radial bending moment, Q_b is the unit shear force (the force per unit of the circumferential length), D is a plate constant given below, C is the plate constants dependent upon the ratio a/b, where b is the shaft radius (which assumed as 20% of the outer diameter of the machine (Mueller et al. 2005) and L is the loading constants dependent upon the ratio a/r_0. The equations to evaluate the constants C_2, C_3, C_8, C_9, L_{11} and L_{17} are given in Appendix I. M_{rb}, Q_b and D are given by equations (3.32-3.34) respectively.

$$M_{rb} = \frac{-qa^2}{C_8}\left[\frac{C_9}{2ab}(a^2 - r_0^{\,2}) - L_{17}\right] \tag{3.32}$$

$$Q_b = \frac{q}{2b}(a^2 - r_0^{\,2}) \tag{3.33}$$

$$D = \frac{Et^3}{12(1-v^2)} \tag{3.34}$$

where E is the modulus of elasticity, v is the Poisson's ratio and t is the plate thickness.

The minimum rotor thickness, t_r, can be found by specifying the maximum allowable deflection, y_a. This can be derived by re-arranging the equation (3.31),

$$t_r = \sqrt[3]{\frac{12a^2(1-\nu^2)}{Ey_a}[M_{rb}C_2 + Q_b aC_3 - qa^2 L_{11}]} \tag{3.35}$$

The mass of the rotor discs can be calculated from the thickness of the rotor disc,

$$m_r = n_{disc}\rho_{ms}(a^2 - b^2)t_r \tag{3.36}$$

where the ρ_{ms} is the density of mild steel.

3.4 Optimisation process

The aim of an optimisation process is to determine a most suitable design that fulfils the application requirements and constraints, such that the number of machines for FEM is reduced. The application requirements and the key parameters of the YASA generator for wind turbines are shown in Table 3.4.

Table 3.4: The application requirements and the key parameters of the YASA generator.

Parameter	Symbol	Value	Unit
Rated power	P	1	MW
Rated rotational speed	ω	25	rpm
Number of pole pairs	p	50	-
Number of stator cores	N	120	-
Phase number	m	3	-
Current density	J	6×10^6	A/m^2
Length of air gap	g	0.005	m
Flux density of stator tooth	B_t	1.6	T
Flux density of stator shoe	B_{sh}	1.9	T
Remanent flux density of permanent magnet (NdFeB)	B_r	1.235*	T
Flux density of rotor back iron	B_{bi}	1.9	T
Recoil permittivity	μ_r	1.05	F/m
Leakage factor	k_l	0.9	-
Magnetic path reluctance factor	k_r	1.1	-
Magnet concentration factor	C_Φ	0.9	-

* Data obtained from Arnold Magnetic Technologies (2013).

3.4.1 Objective functions and variables

The objective functions considered in this optimisation process in the design of a MW-scale YASA generator are the outer diameter, the structural weight, the cost of active materials and the power losses. These objective functions are calculated with equations (3.3) for outer diameter, (3.36) for structural weight, (3.24) and (3.27) for active materials cost and (3.28) for power losses. Three variables used to calculate the objective functions are the air gap flux density B_g, the ratio of the outer-to-inner machine diameter k_d and the current loading A_s.

The outer diameter is chosen as an objective function because the generator must be able to fit into a nacelle, the size of which is limited by the length of the blades. A smaller outer diameter and lighter weight would also be beneficial during the transportation and the installation of the machine. The weight of a generator is mainly determined by the structural weight, while the cost of a generator is mainly driven by the cost of active materials, predominantly the permanent magnets. The power losses are important to be kept low to achieve a good efficiency. It is important to note that some of these objective functions are in conflict. For example, a machine with a smaller outer diameter will require more permanent magnets to generate the same torque. Therefore, reducing the generator size and the active material costs may not be achieved at the same time.

B_g and A_s are considered as variables because B_g is an important parameter that determines a machine's performance under no load condition while A_s determines the performance under full load condition. k_d decides the surface area of the permanent magnets which is especially crucial for a machine with a large diameter. The maximum B_g of a permanent magnet generator is limited by the residual flux density of permanent magnets, which is around 1.235 T for the NdFeB magnet and the air gap length (5 mm). Due to losses through the air gaps and the magnet slots, the upper limit of B_g is considered at 1 T.

According to equation (3.1) and (3.2), a generator with a higher current loading requires a smaller outer diameter to achieve the same output power. The current loading is limited by the dimension of the stator slot. The allowed current in the stator winding is also subject to the temperature limitation of the winding insulation and the effectiveness of the cooling system (Toliyat & Kliman, 2004; Bil, 2008). A typical range of the current loading for wind turbines suggested by Li *et al.*(2009) is between 4×10^4 and 6×10^4 A/m. However, in this optimisation process, a wider range from 1×10^4 to 10×10^4 A/m is considered.

3.4.2 Design reference map

Taking into account of these objective functions and variables, a design reference map can be generated shown in Figure 3.5. This design reference map visualises how these objective functions (the outer diameter, the power losses, the cost of active materials and the structural weight) change with the air gap flux density B_g and the outer-to-inner diameter ratio k_d under a constant current loading A_s.

To better understand how these objective functions are influence by B_g and k_d, A, B, C and D four points are chosen from the four corners of the design reference map. Each point represents a machine design with different B_g and k_d combinations (A-low B_g low k_d, low B_g high k_d, C- high B_g high k_d, and D- high B_g low k_d). It can be seen that the machine outer diameter and the structural weight

are low at high B_g and low k_d such as point D. However, more permanent magnets are needed to generate the same amount of B_g. An increase in the usage of more rare-earth magnets is expected to drive up the costs. A design that requires less active materials can be achieved by minimising B_g and maximising k_d such as machine design B. This results in an increase in the machine outer diameter and the copper losses. Machines with larger diameters usually have longer end windings and thus the copper losses increases proportionally. With the same B_g, machine design A has a higher power losses than B does as the machine with lower k_d will need to use more iron and hence the iron losses increase. Therefore, it is clear that to design a machine with a high efficiency and a small outer diameter, a large B_g should be chosen, such as designs C and D. If reducing the cost of active materials and power losses are desired, a high k_d is preferred. For example, a design with requirements on the outer diameter less than 5 m and the active materials cost within €100,000, B_g should be chosen between 0.3 T and 0.95 T and k_d between 0.01 and 0.92. In this case, only machine C is able to fulfil such requirements.

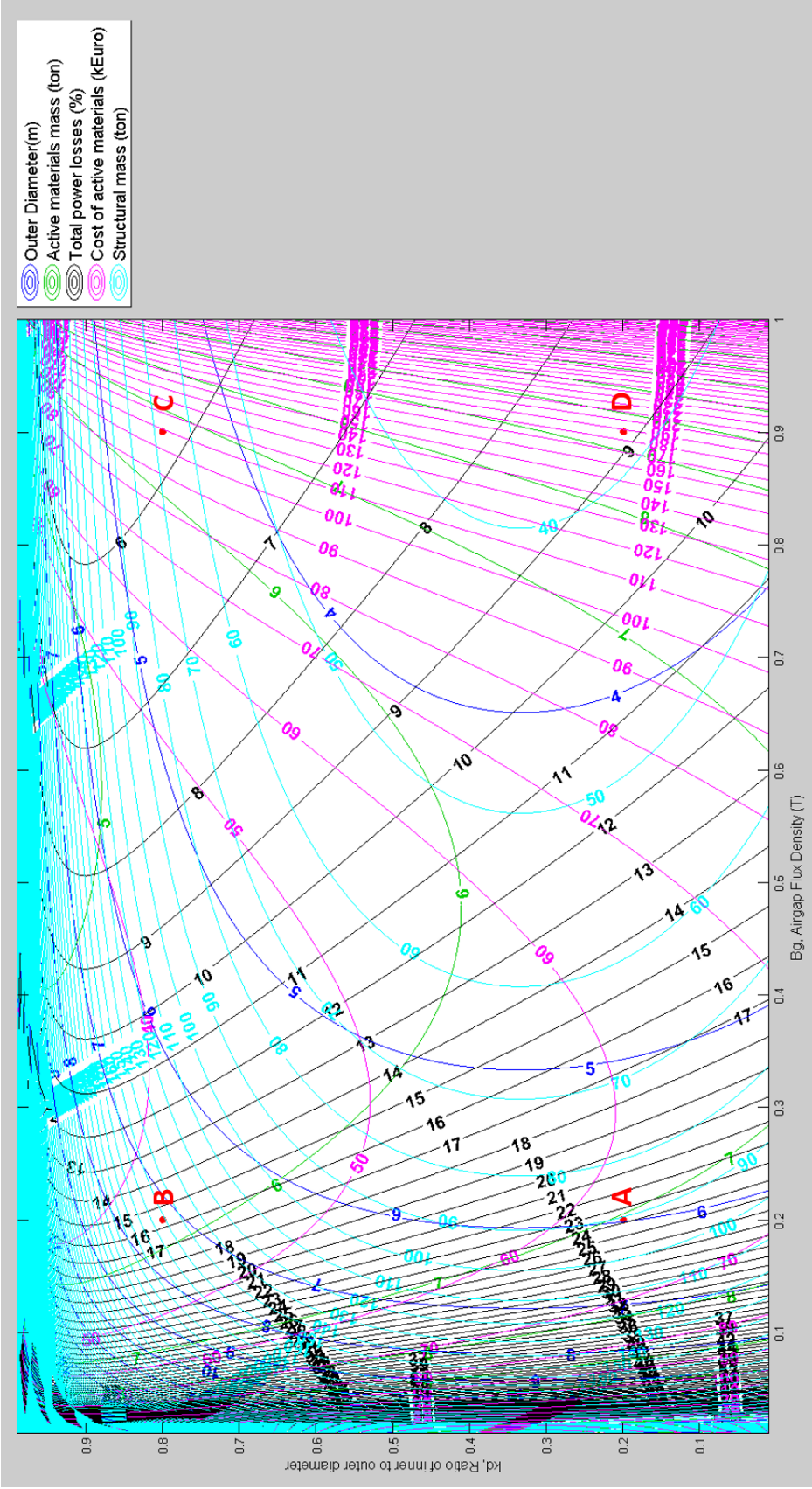


Figure 3.5: A typical design reference map.

3.4.3 Optimisation with pseudo-weight vector approach

To solve these conflicting objective functions in the design optimisation of a YASA generator, a multi-objective optimisation tool should be incorporated.

It is thought that a good optimisation tool should allow users to prioritise one or more objective functions based on their requirements. This can be achieved by using a pseudo-weight vector approach (Deb 2009; Hillier & Hillier 2002). This method allows different weights to be placed onto each objective function. First, the weight w_i for the i-th objective function is computed using the following equation,

$$w_i(x) = \frac{\left(f_i^{max} - f_i(x)\right)/\left(f_i^{max} - f_i^{min}\right)}{\sum_{m=1}^{M}\left(f_m^{max} - f_m(x)\right)/\left(f_m^{max} - f_m^{min}\right)} \tag{3.37}$$

where f^{max} is the maximum value of an objective function f^{min} the minimum value of an objective function, $f_i(x)$ is the value of an objective function value at point x, and M is the total number of objective functions.

An example to find the weight of D_o is used here to explain this method in detail. Assuming D_o is the first objective function and there are totally four objective functions (D_o, C_{act}, P_{tot} or W_{struc}) to be optimised, thus $i = 1$ and $M = 4$. The weights of D_o within the constraints are calculated from $x = 1$ to n (Table 3.5) using equation (3.37) and is written as,

$$w_{D_o}(n) = \frac{[f_{D_o}^{max} - f_{D_o}(n)]/[f_{D_o}^{max} - f_{D_o}^{min}]}{\{[f_{D_o}^{max} - f_{D_o}(n)] + [f_{D_o}^{max} - f_{D_o}(n)] + [f_{D_o}^{max} - f_{D_o}(n)] + [f_{D_o}^{max} - f_{D_o}(n)]\}/[f_{D_o}^{max} - f_{D_o}^{min}]} \quad (3.38)$$

Table 3.5: Representation of $f_i(x)$ and $f_m(x)$ at x from 1 to n.

m	1	2	3	M=4
i	Outer diameter, D_o	Cost of active materials, C_{act}	Total power loses, P_{tot}	Structural mass, W_{struc}
x=1	$f_{D_o}(1)$	$f_{C_{act}}(1)$	$f_{P_{tot}}(1)$	$f_{W_{struc}}(1)$
x=2	$f_{D_o}(2)$	$f_{C_{act}}(2)$	$f_{P_{tot}}(2)$	$f_{W_{struc}}(2)$
x=3	$f_{D_o}(3)$	$f_{C_{act}}(3)$	$f_{P_{tot}}(3)$	$f_{W_{struc}}(3)$
x=4	$f_{D_o}(4)$	$f_{C_{act}}(4)$	$f_{P_{tot}}(4)$	$f_{W_{struc}}(4)$
x=5	$f_{D_o}(5)$	$f_{C_{act}}(5)$	$f_{P_{tot}}(5)$	$f_{W_{struc}}(5)$
…	…	…	…	…
x=n	$f_{D_o}(n)$	$f_{C_{act}}(n)$	$f_{P_{tot}}(n)$	$f_{W_{struc}}(n)$

Now the same calculation is applied to calculate the weights of all other three objective functions (C_{act}, P_{tot} or W_{struc}). Once the weights of all objective functions are obtained, they are compared with a standard weight for each objective function defined by a user. The total deviation of the weights of the objective functions from their corresponding standard weights (sw_m) is calculated by,

$$Total\ weight\ deviation = \sum_{m=1}^{M} |w_m - sw_m| \quad (3.39)$$

It is important to note that the sum of the standard weights for all objective functions should be equal to 1.

Using this method, designers can set the standard weight for each objective functions. How this optimisation tool works is explained in the following examples. First, the constraints are set for the design: the outer diameter below 5 m and the cost of active materials below €100,000. All four objective functions are considered equally important; that is, each objective function is given a standard weight of 0.25. The total weight deviations are the blue lines plotted in the design reference map (Figure 3.6 and Figure 3.7). The red dot on the map has the lowest total weight deviation to the standard weight, thus the optimum. In this case, this optimum is produced when all objective functions are treated equally.

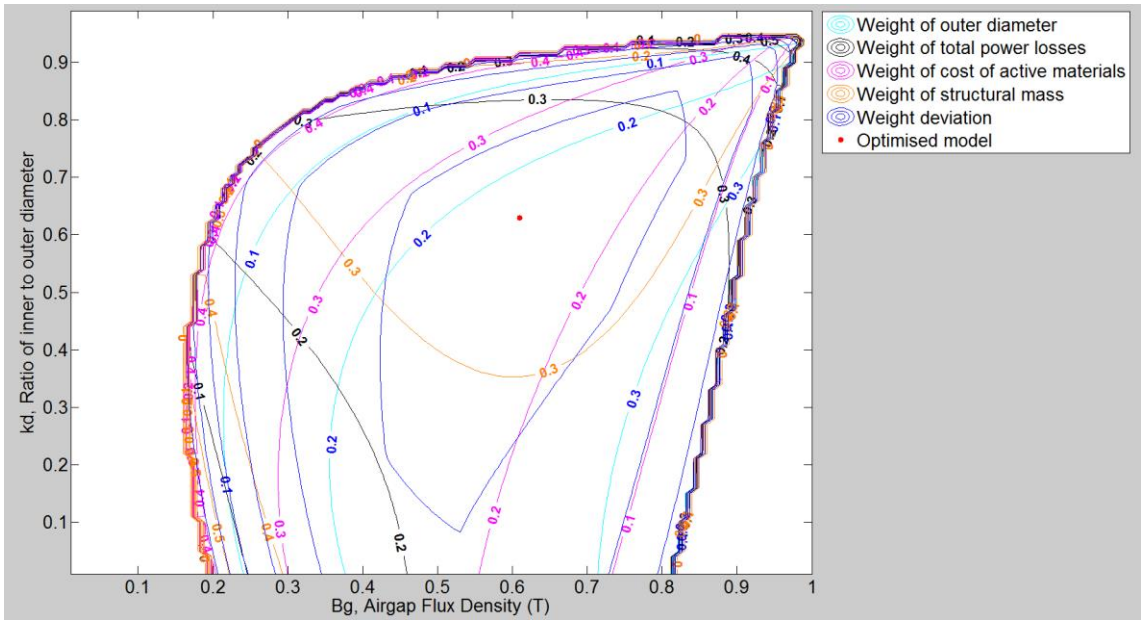


Figure 3.6: Contour graph of weight of objective functions and weight ratio of 1MW YASA at 1×10^5 A/m with weight ratio and the optimised YASA machine (Bg=0.63T and kd=0.61) plotted. (The aimed weights on the objective functions are: Aimed weight of total power losses is 0.25, structural mass is 0.25, cost of active materials is 0.25 and outer diameter is 0.25. Constraints are outer diameter ≤ 5 and cost of active materials ≤ €100,000.).

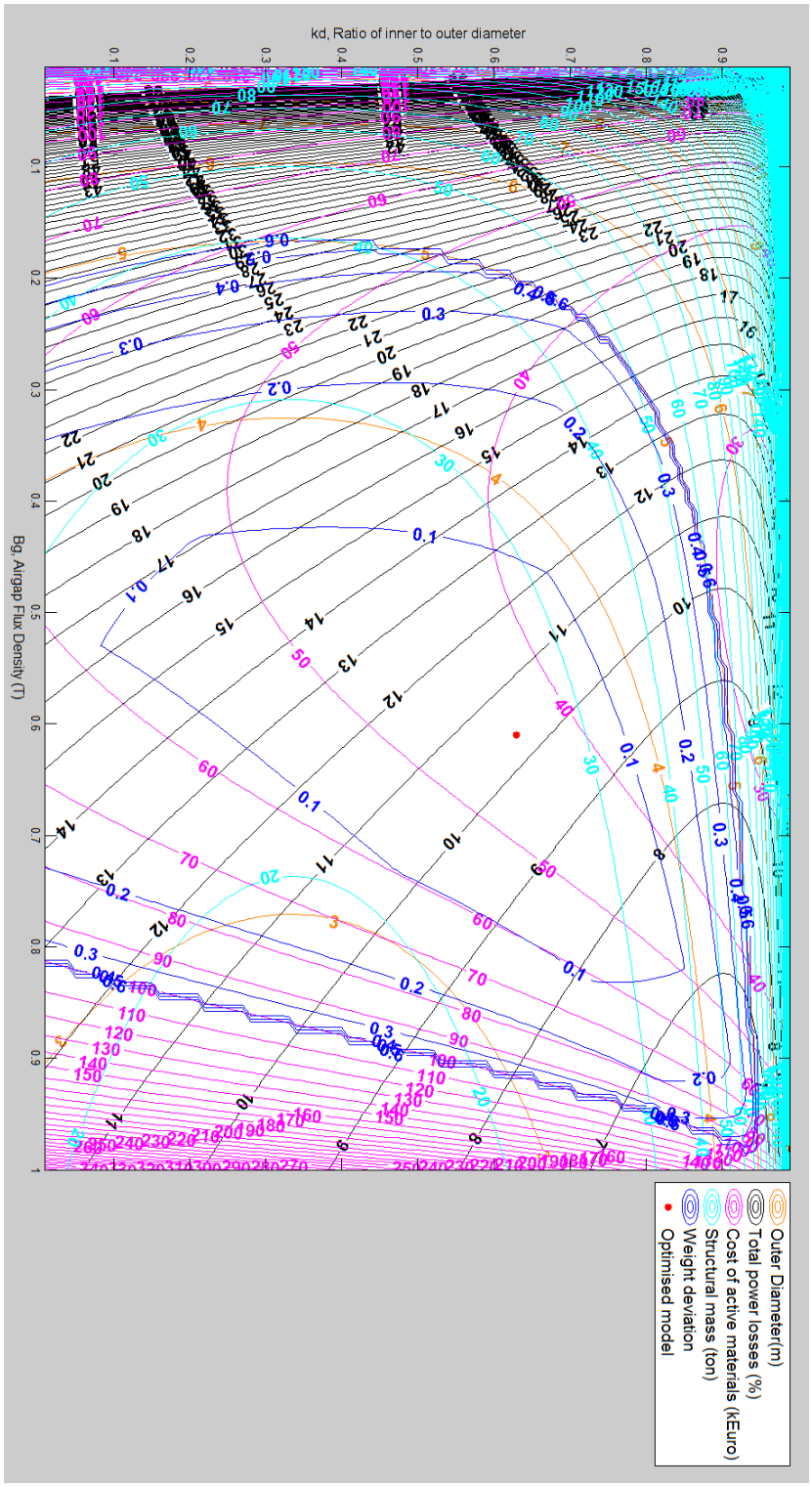


Figure 3.7: Design reference map of 1 MW YASA at 1×10⁵ A/m with weight ratio and the optimised YASA machine (Bg=0.63T and kd=0.61) plotted. (The aimed weights on the objective functions are: Aimed weight of total power losses is 0.25, structural mass is 0.25, cost of active materials is 0.25 and outer diameter is 0.25. Constraints are outer diameter ≤ 5 and cost of active materials ≤ €100,000.).

It is more common that some objective functions can be justified as being more important than the others. In this example, the power losses are prioritised as they not only determine the generator's efficiency but also will affect the design of the cooling system. The structural weight follows, considering these generators may be used in an offshore wind farm, in which heavy weight may be problematic. The same constraints are given to the outer diameter and the cost of active materials. All values within the constraints are acceptable but lower values are preferred. If a model has an objective function out of the constraint values, that model will be eliminated. Therefore, the standard weights set for the objective functions are: power losses - 0.6, structural mass - 0.2, outer diameter - 0.1 and cost of active materials - 0.1. A design reference map with the weight ratios and an optimised YASA design (red dot) is shown in Figure 3.8 and Figure 3.9. The parameters of the optimised design are listed in Table 3.6. The electromagnetic performance of this design will be studied using an analytical method in the following sections and using FEM in the next chapter.

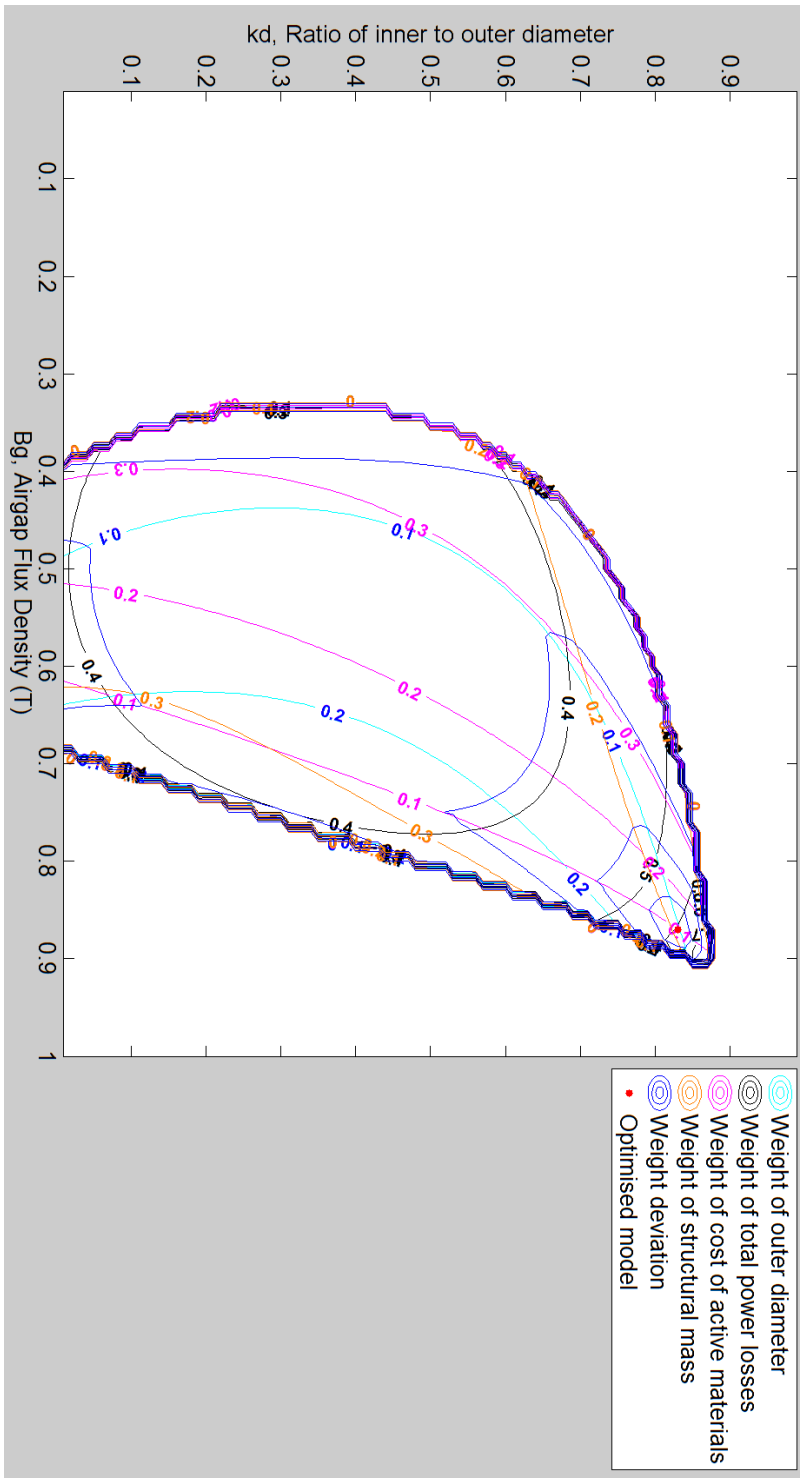


Figure 3.8: Contour graph of weight of objective functions and weight ratio of 1MW YASA at 5×10⁴ A/m and the optimised YASA machine (Bg=0.87T and kd=0.83) plotted. (The aimed weights on the objective functions are: Aimed weight of total power losses is 0.6, structural mass is 0.2, cost of active materials is 0.1 and outer diameter is 0.1. Constraints are outer diameter ≤ 5 and cost of active materials ≤ €100,000.)

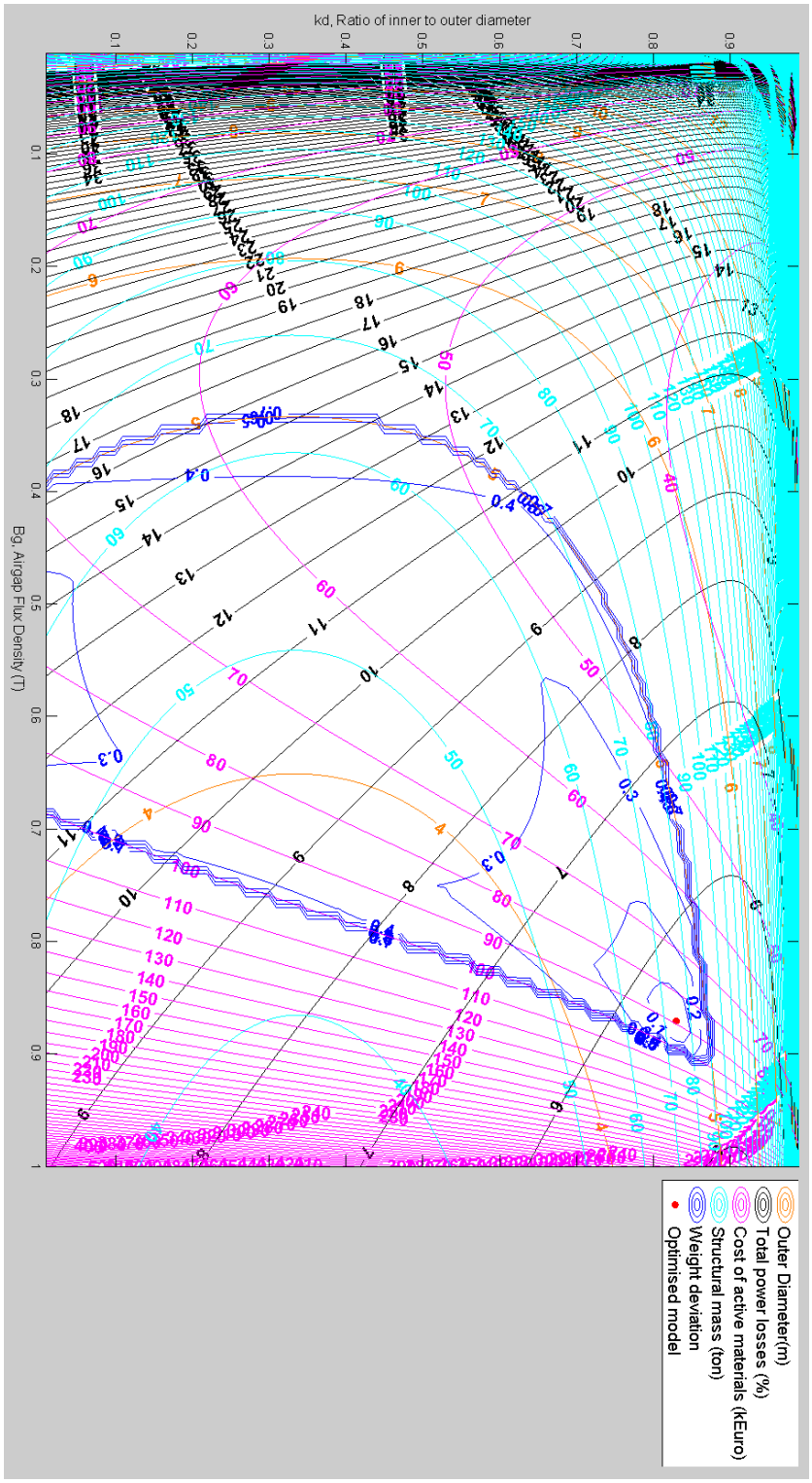


Figure 3.9: Design reference map of 1MW YASA at 5×10⁴ A/m with weight ratio and the optimised YASA machine (Bg=0.87T and kd=0.83) plotted. (The aimed weights on the objective functions are: Aimed weight of total power losses is 0.6, structural mass is 0.2, cost of active materials is 0.1 and outer diameter is 0.1. Constraints are outer diameter ≤ 5 and cost of active materials ≤ €100,000.)

Table 3.6: The optimised 1MW YASA generator design parameters.

Parameters	Values
Power rating (MW)	1
Rated rotational speed (rpm)	25
Air gap flux density, B_g (T)	0.87
Ratio of outer to inner diameter, k_d	0.83
Current loading, A_s (A/m)	5×10^4
Number of poles	100
Number of stator cores	120
Outer diameter (m)	4.64
Inner diameter (m)	3.85
width of stator slot (m)	0.01
width of copper winding (m)	0.0192
length of stator bar (m)	0.0302
width of stator shoe (m)	0.111
length of stator shoe (m)	0.0075
length of permanent magnet (m)	0.0243
width of permanent magnet (m)	0.120
length of back iron (m)	0.0305
copper losses (W)	5.05×10^4
Iron losses (W)	1.47×10^3
Electrical frequency (Hz)	20

3.4.4 Sensitivity test

There are nine constants ($\underline{k_f}$, α_{sh}, α_{cg}, α_t, k_r, k_l, C_Φ, α_p and g) used in the sizing equations to calculate the geometry of the YASA machines. The values of these constants are selected based on assumptions or previous report. The values of these nine constants may influence the optimisation results and the sensitivity of these constants to the optimisation algorithms is worth investigation. The two case studies discussed above in section 3.4.3 are used to test the sensitivity of the constants. Both case studies are set with same constraints, which are the outer

diameter ≤ 5 m and the cost of active materials ≤ €100,000. In Case Study 1, all four objective functions are treated equally and given weight ratio 0.25, while in the second case study, the weight ratios are: total power losses - 0.6, structural mass - 0.2, cost of active materials - 0.1 and outer diameter - 0.1.

To test the sensitivity of each constant, the value of each constant is varied by ±2% from its original value. The new values of these nine constants are used to obtain the optimised results of the variables (B_g, k_d and the current loading A_s) and the objective functions (the outer diameter (D_o), the total power losses (P_{tot}), the cost of active materials ($C_{_act}$) and the structural mass (Strucmass)). Their sensitivities are compared by normalising the change of the calculated results against the change of the constants. For example, when k_f is increased to k_f^+ by 2% and reduced to k_f^- by 2%, the change of k_f is,

$$\Delta k_f = \frac{k_f^+ - k_f^-}{k_f} \tag{3.40}$$

In this case, $\Delta k_f = 0.04$.

The change of B_g is,

$$\Delta B_g = \frac{B_g^+ - B_g^-}{B_g} \tag{3.41}$$

where B_g^+ and B_g^- are the optimised results calculated using k_f^+ and k_f^-, respectively.

This value is normalised against Δk_f to calculate the sensitivity of varying k_f by ±2% to the final result of B_g,

$$\Delta B_g / \Delta k_f \tag{3.42}$$

These normalised values for both case studies are shown in Table 3.7 and Table 3.8. The higher the normalised value is, the bigger role the constant plays in the optimisation.

Table 3.7: Sensitivity test results based on the weight ratio of the objective functions: Strucmass=0.25, Ptot=0.25, Do=0.25, C_act=0.25.

Symbol	*Bg*	*kd*	*As*	*Do*	*Ptot*	*C_act*	*Strucmass*
k_f	0	0	0	0	0.00726	0.0569	0
α_{sh}	0	0	0	0	0	0	0
α_{cg}	0	0	0	0	0.00242	0.00517	0
α_t	0	0	0	0	0.00242	0.00747	0.0349
k_r	0.410	0	0	0.138	0.273	0.232	0.194
k_l	0.820	0	0	0.273	0.537	0.646	0.384
C_Φ	0.820	0.397	0	0.147	0.726	0.358	0.0642
α_p	0.410	0	0	0.138	0.273	0.232	0.194
g	0.410	0	0	0.138	0.273	0.232	0.133

Table 3.8: Sensitivity test results based on the weight ratio of the objective functions: Strucmass=0.2, Ptot=0.6, Do=0.1, C_act=0.1.

Symbol	*Bg*	*kd*	*As*	*Do*	*Ptot*	*C_act*	*Strucmass*
k_f	0	0	0	0	0.0152	0.0264	0
α_{sh}	0	0	0	0	0.0246	0.0419	0.103
α_{cg}	0	0	0	0	0.00223	0.00394	0
α_t	0	0	0	0	0.00268	0.00422	0.0692
k_r	0.287	0	0	0.0922	0.176	0.583	0.140
k_l	0	1.20	5	0.356	0.809	0.383	0.463
C_Φ	0	1.20	5	0.356	0.809	0.420	0.463
α_p	0.287	0	0	0.0922	0.176	0.583	0.140
g	0.287	0	0	0.0922	0.176	0.583	0.181

From the tables for both case studies, it can be clearly seen that the optimisation is not sensitive to $\underline{k_f}$, α_{sh}, α_{cg} and α_t, but to k_r, k_l, C_Φ, α_p and g. This is interesting as it implies that the optimisation is not sensitive to the constants that are related to the stators but to the ones that associates with the rotors and the air gap. This is because the rotor-related constants (k_r, k_l, C_Φ and α_p) and the air gap will affect the strength of the air gap flux density B_g. Among these five constants, the flux leakage, k_l and the magnet concentration factor, C_Φ, are the most influential constant. Although A_s seem to be very sensitive to k_l and C_Φ but not to the other constants at all, it is important to stress the data points for A_s are coarse with only 10 data points, between which the gap is $1\text{x}10^4$ A/m^2. For example, in the second case study, $A_s(C_\Phi^-)$ is $6\text{x}10^4$ A/m^2, $A_s(C_\Phi)$ is $5\text{x}10^4$ A/m^2 and $A_s(C_\Phi^+)$ is $5\text{x}10^4$ A/m^2. A small shift in C_Φ cause a change in A_s by one data point, and hence the final

sensitivity value is unrealistically high. Testing sensitivity on a parameter with large data gap is not accurate.

The ranges of these constants are also considered and shown in Table 3.9. The minimum value of k_f is considered to be 0.5, lower than which is not practical as the use of copper coils becomes inefficient and losses will be very high. The upper limit is set to 0.9 as winding copper coils tighter than this is impossible, especially for MW machines with thick copper wires. The minimum value of a_{sh} is believed to be around 0.7 because it is unlikely to have such a big gap between stator shoes, as it will cause a high leakage flux, while the highest value is believed to be 0.9, because if the gap is too small or the stators shoes are in contact, the flux leakage will be high. The minimum value of a_{cg} is considered to be 0.01, as some gaps needs to be reserved for cooling, while the highest value is set to 0.1 because if the gaps are too wide they will reduce the conductivity between the iron core and the copper coil, which increases the leakage inductance. The minimum value of a_t is set to 0.8 because if radii corner are too big, too much iron is removed and hence it will have less flux going through the iron core, while the maximum is 0.99, as this will reduce radii corners to reduce the end windings and leakage inductance. The typical magnetic path reluctance factor of a machine is $1<k_f\leq1.2$. The typical leakage factor in machine design is $0.9\leq k_l<1$. However, in the sensitivity test, this is dropped to 0.7, while the maximum value is 0.99, which is practically difficult to achieve. For k_l, the cost of active materials goes up to very high when it

is set to 0.7, as magnets are not efficiently used at this value and the leakage of flux passing through iron cores is high. The minimum value of C_Φ is set to 0.83, because it is the lowest value to generate results within the boundary during the test. The maximum of C_Φ is 0.99 as some gap is to be reserved between two magnets with different pole.

Table 3.9: Minimum and maximum values of the constants.

Constant	Minimum	Maximum
kf	0.50	0.90
αsh	0.70	0.90
αcg	0.01	0.10
αt	0.80	0.99
kr	1.00	1.20
kl	0.70	0.99
CΦ	0.83	0.99
αp	0.70	0.99

3.5 Properties and performance of the YASA machine

3.5.1 Efficiency map of the YASA generator

The efficiency of a generator can be calculated using the input power and the power losses,

$$\eta = \frac{P_{out}}{P_{in}} = \frac{P_{in} - P_{loss}}{P_{in}} \tag{3.43}$$

The input power is determined by the torque and the rotational speed (i.e. $P_{in} = T\omega$). The power losses in this study only consider the two main losses: the

iron losses and the copper losses. The eddy current losses and the mechanical losses in the permanent magnets are not considered in this analytical study. The iron losses are calculated by equation (3.27). The frequency of the field in the stator iron, f_e, is not fixed to 20 Hz but varies according to the change of the angular speeds. The copper losses is calculated by,

$$P_{cu} = m_1 I^2 R_{ph} \tag{3.44}$$

where R_{ph} is the AC phase resistance of the stator windings. The phase current,

$$I = \frac{k_i A_s \pi D_o (1 + k_d)}{2 m_1 N_{ph}} \tag{3.45}$$

The AC phase resistance is (Hanselman 2003),

$$R_{ph} \approx R_{dc} \left(1 + \frac{1}{9}\left(\frac{w_{sd}}{\chi}\right)^2 \left(\frac{d_w}{\chi}\right)^2\right) \tag{3.46}$$

where χ is the skin depth of the conductor in free space, d_w is the diameter of a single conductor and the DC phase resistance of the coil,

$$R_{dc} = \frac{l_{turn}(1 + r_{Cu}(T - 20))}{\sigma_{Cu} A_w N_{turn}} \tag{3.47}$$

where T is the temperature of the coil in degree Celsius (°C), σ_{Cu} is the electric conductivity of the copper at 20 °C temperature, A_w is the cross-sectional area of copper in one coil turn and N_{turn} is the number of turns per coil.

The efficiency map of the optimised 1 MW YASA generator is shown in Figure 3.10. The design operating ranges of the rotational speed and the torque are 1 to 25 rpm and 6.4×10^3 to 3.8×10^5 Nm, respectively. The copper losses are calculated at the temperature of 155°C. This is considered as the maximum operating temperature of the copper windings in the 1 MW YASA generator at the temperature rating Class F(155°C) and it is below the temperature limit of Class H insulation. Whether this temperature can be achieved by fitting a cooling system will be discussed in Chapter 6. The peak efficiency of the YASA generator is 98.6% at 25 rpm and 7.44×10^4 Nm. The efficiency map also shows that the generator can deliver efficiencies over 97% at above 5.5 rpm, suggesting that it is able to cope with a low wind speed condition.

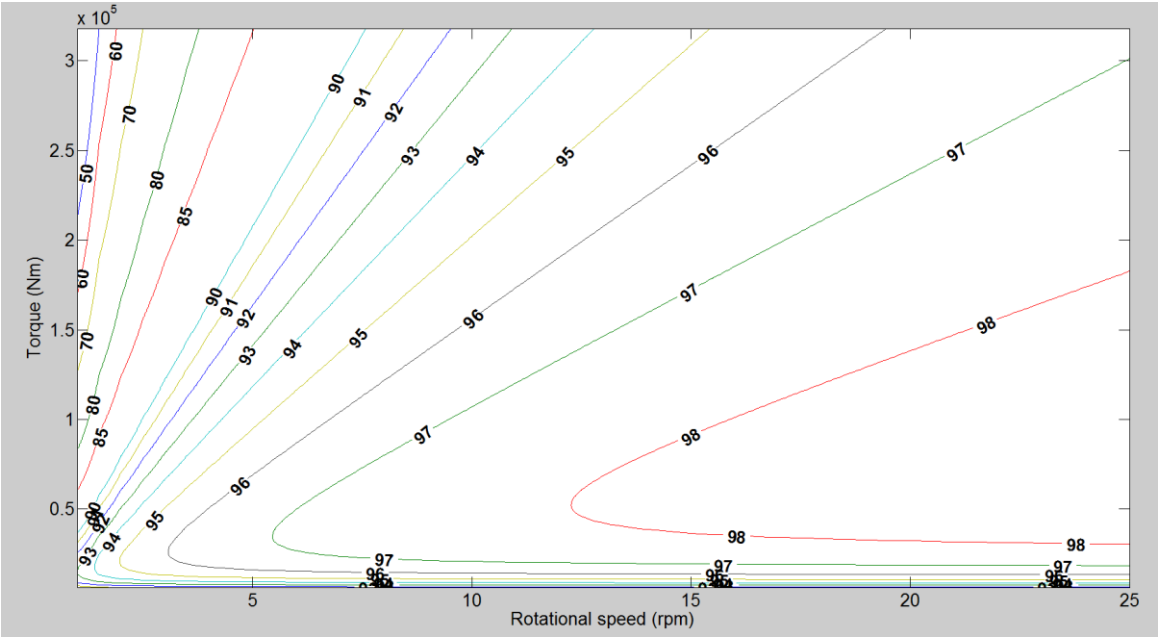


Figure 3.10: Efficiency map of 1MW YASA generator at working temperature at 60°C.

3.5.2 Validation of efficiency map calculation

To validate the above calculation, an efficiency map of a 50 kW YASA machine that has the same parameters as the existing YASA prototype was calculated. The analytical results are compared with the efficiency measured on the prototype. The experimental results at an operating temperature of 55°C under different rotational speeds and torques were measured by Woolmer (2009) and are shown in Table 3.10. The majority of the readings are within 2% deviation of the calculated efficiencies, with 2.28% being the largest deviation from the calculation. These small errors are expected as the calculated efficiencies only considered the main power losses from the stator but does not consider the rotor power losses and mechanical power losses of the machine.

Table 3.10:Comparison between the calculated efficiencies and the measured efficiencies from 50kW YASA machine (Woolmer 2009).

Speed (RPM)	Torque (Nm)	Experimental Efficiency (%)	Simulated Efficiency (%)	deviation
876	13.2	94.7	94.7	0.0
890	27.4	94.5	92.9	1.6
926	40	93.1	90.8	2.3
908	52.3	91	88.2	2.8
1040	67.9	88.4	86.9	1.5
2008	66.7	92.9	93.1	0.2
1752	51.3	94.4	93.7	0.7
1811	39.8	95.2	94.9	0.3
1825	27.5	95.4	95.9	0.5
1757	14.7	95	96.2	1.2
3582	61.5	94.6	96.1	1.5
3595	48.3	95.6	96.7	1.1
3537	28.7	95.9	97.3	1.4

Figure 3.11 is an efficiency map as functions of rotational speeds from 0 to 3600 rpm and torques from 0 to 120 Nm. The measured peak efficiency of 95.9% occurred at the machine torque of 28.7 Nm and the speed of 3537 rpm, while the peak simulated 97.4% occurred at a machine torque of 24.1 Nm and speed of 3600 rpm. The good correlation between the calculated and measured results gives confidence that the analytical design of the YASA machine gives a reasonable degree of accuracy.

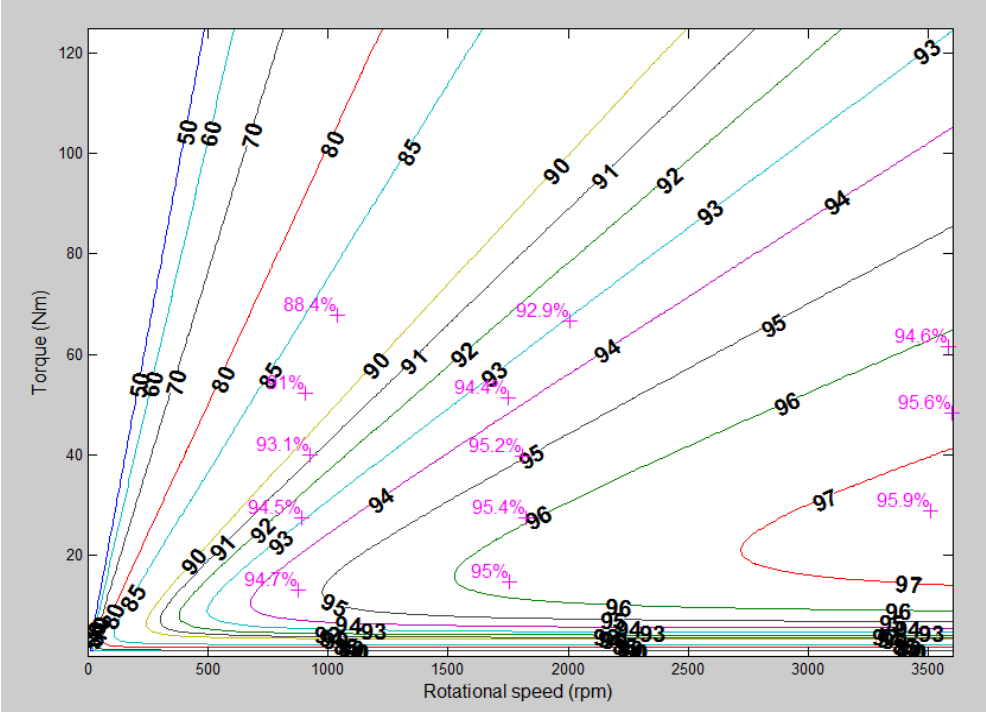


Figure 3.11:Simulated efficiency map for the 50kW YASA machine with experimental data measured with 50 kW YASA prototype by (Woolmer 2009). Machine temperature=55°C.

3.5.3 No load air gap flux density

The waveforms of the air gap flux density not only depends on the strength of the permanent magnets but also depends on the geometry of the machine and the air gap length. The geometry-dependent magnetic flux density for an axial flux machine can be computed as an linear machine using the equation proposed by Chung & Gweon (2002) ,

$$B_{PM}(x) = -\sum_{n=1,3,5,\ldots}^{\infty} \frac{\left(\frac{8B_r}{n\pi} sin\frac{k_{PM} n\pi}{2}\right)\left(e^{\frac{-n\pi g_e}{\tau}} cos\frac{n\pi x}{\tau}\right)}{\left(e^{\frac{-2n\pi g_e}{\tau}}+1\right)+\frac{\mu_{PM}\left(-e^{\frac{-2n\pi g_e}{\tau}}+1\right)\left(-e^{\frac{-2n\pi l_{PM}}{\tau}}+1\right)}{\mu_0\left(e^{\frac{-2n\pi l_{PM}}{\tau}}-1\right)}} \tag{3.48}$$

where B_r is the remanent magnetic flux density, μ_0 is the free space recoil permeability, μ_{PM} is the PM recoil permeability, n is the number of harmonic, τ is the pole pitch, k_{PM} is the ratio of magnet width to pole pitch, l_{PM} is the magnet height and g_e is the effective air gap length which is given as (Chung & Gweon 2002),

$$g_e = K_c\left(g + \frac{l_{PM}}{\mu_r}\right) \tag{3.49}$$

where μ_r is the relative permeability, and K_c is the Carter's Coefficient (Hanselman 2003) and given by,

$$K_c = \left[1 - \frac{w_s}{\tau_s} + \frac{4\left(g + \frac{l_{PM}}{\mu_r}\right)}{\pi\tau_s} ln\left(1 + \frac{\pi w_s}{4\left(g + \frac{l_{PM}}{\mu_r}\right)}\right)\right]^{-1} \tag{3.50}$$

The YASA machine has slotted stator cores, which cause changes in the resistance to the air gap flux density. This is called the slotting effect. The impact of the slotting on the air gap flux density can be considered by multiplying the permeance (λ) changes in the air gap due to the slots with the magnetic flux density. This is given by,

$$B_{ag}(x) = \lambda B_{PM}(x) \tag{3.51}$$

The relative permeance value is assumed equal to 1 at the locations where the stator core faces the air gap. At the locations where the slot faces the air gap, the relative permeance is assumed to be (Proca et al. 2003),

$$\lambda = \frac{g + \frac{l_{PM}}{\mu_r}}{g + \frac{\pi}{2}\omega + \frac{l_{PM}}{\mu_r}} \tag{3.52}$$

The waveform of the air gap flux density of the 1 MW YASA machine is computed and shown in Figure 3.12.

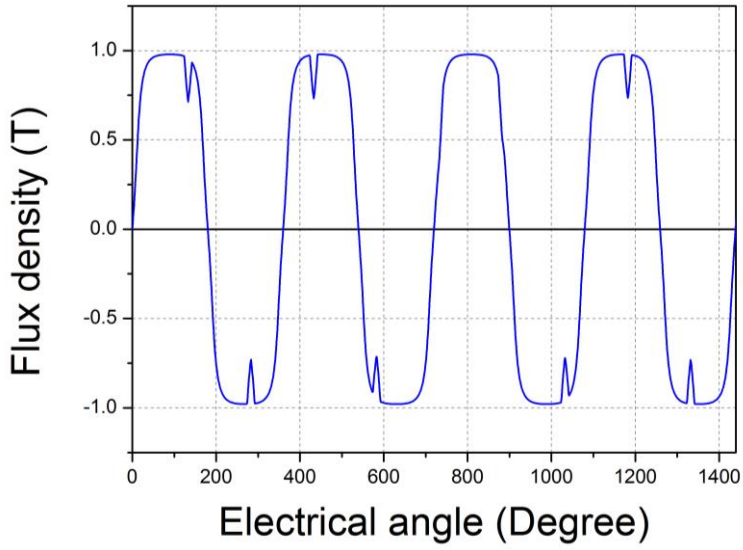


Figure 3.12: The waveform of the air gap flux density waveform of the 1MW YASA machine that is calculated using the analytical method.

3.5.4 Winding design

The YASA generator is designed to have fractional slot concentrated windings, in which the number of slots per pole per phase of a winding is a

fraction. The fractional slot winding design becomes more popular in synchronous permanent magnet machines (Bianchi & Dai Pre 2006; Cros & Viarouge 2002; Hörz et al. 2006; El-refaie 2010; Nicola Bianchi et al. 2006), because it has the following advantages over the conventional integral slot windings: 1) a smoother torque can be generated due to the elimination of the periodicity between the poles and the slots (Nicola Bianchi et al. 2006); 2) a higher fault tolerance that allows the machine to work even during faulty conditions (Nicola Bianchi et al. 2006); 3) the windings concentrated around the stator teeth reduces the effect of end windings, hence reducing the copper losses (Magnussen & Sadarangani 2003; Cros et al. 1998); 4) it has good flux weakening which allows the machine to achieve wide constant power operation (Zhu 2009; El-Refaie et al. 2006).

The single layer fractional slot concentrated winding layout of the 120 slots and 100 poles, 1 MW YASA machine is analysed base on the methods presented by Hanselman (1994); Hendershot & Miller (1994) and Pyrhnen, Jokinen, & Hrabovcov (2008). The detailed calculation process is shown in Appendix II. The base winding phasor diagram of this machine is obtained and shown in Figure 3.13 with the winding layout shown in Table 3.11.

Table 3.11: Winding layout of the 1MW YASA machine with 120 stator cores and 50 pole pairs.

Coil No.	Coil Angle (Electrical degree)	Phase U		Phase V		Phase W	
		In	Out	In	Out	In	Out
1	0	1	2	5	6	4	3
2	-30	3	2	7	6	4	5
3	0	8	7	12	11	9	10
4	-30	8	9	12	13	11	10
5	0	13	14	17	18	16	15
6	-30	15	14	19	23	16	17
7	0	20	19	24	23	21	22
8	-30	20	21	24	25	23	22
9	0	25	26	29	30	28	27
10	-30	27	26	31	35	28	29
11	0	32	31	36	35	33	34
12	-30	32	33	36	37	35	34
13	0	37	38	41	42	40	39
14	-30	39	38	43	47	40	41
15	0	44	43	48	47	45	46
16	-30	44	45	48	49	47	46
17	0	49	50	53	54	52	51
18	-30	51	50	55	59	52	53
19	0	56	55	60	59	57	58
20	-30	56	57	60	61	59	58
21	0	61	62	65	66	64	63
22	-30	63	62	67	71	64	65
23	0	68	67	72	71	69	70
24	-30	68	69	72	73	71	70
25	0	73	74	77	78	76	75
26	-30	75	74	79	83	76	77
27	0	80	79	84	83	81	82
28	-30	80	81	84	85	83	82
29	0	85	86	89	90	88	87
30	-30	87	86	91	95	88	89
31	0	92	91	96	95	93	94
32	-30	92	93	96	97	95	94
33	0	97	98	101	102	100	99
34	-30	99	98	103	107	100	101
35	0	104	103	108	107	105	106
36	-30	104	105	108	109	107	106
37	0	109	110	113	114	112	111
38	-30	111	110	115	119	112	113
39	0	116	115	120	119	117	118
40	-30	116	117	120	1	119	118

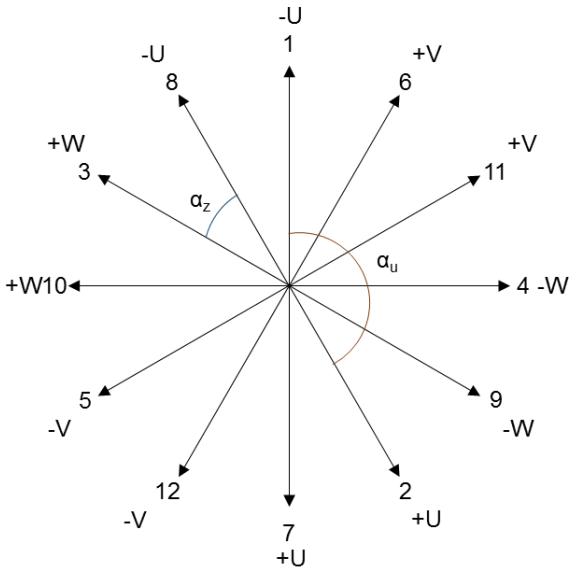


Figure 3.13: Base winding phasor diagram.

3.5.5 Back EMF

The back EMF is the voltage induced by permanent magnets under no load condition. The phase back EMF can be calculated by,

$$EMF = \frac{-N_{ph} k_w \frac{d\varphi}{dt}}{\sqrt{2}} \tag{3.53}$$

where ϕ is the magnetic flux which can be evaluated by the air gap flux density evaluated with (3.43) by integrating the air gap flux density against the air gap surface area (S_{ag}). The magnetic flux is given by,

$$\varphi = \int B_{ag}\, dS_{ag} \tag{3.54}$$

To generate a back EMF to achieve a rated voltage of 3.3 kV, the number of turns of winding per phase is calculated to be 870. This means that, each core requires 29 turns per coil. To have this number of windings fit into the winding slot (height = 0.0302 m and width = 0.0192 m), the square copper wire with a size of AWG 6 is adequate. The specifications of AWG 6 is shown in Table 3.12. The back EMF waveform of the 1 MW YASA machine is shown in Figure 3.14.

Table 3.12: Specification of square copper wire.*(MWS Wire Industries 2014b)*.

	Bare Copper			With Insulation			
size (AWG)	Dimensions (m)			Diameter (m)			
	min	nom	max	min inc	min o.d	nom o.d	max o.d
6	0.0040742	0.004115	0.004155	7.62E-05	0.00415	0.004216	0.004282

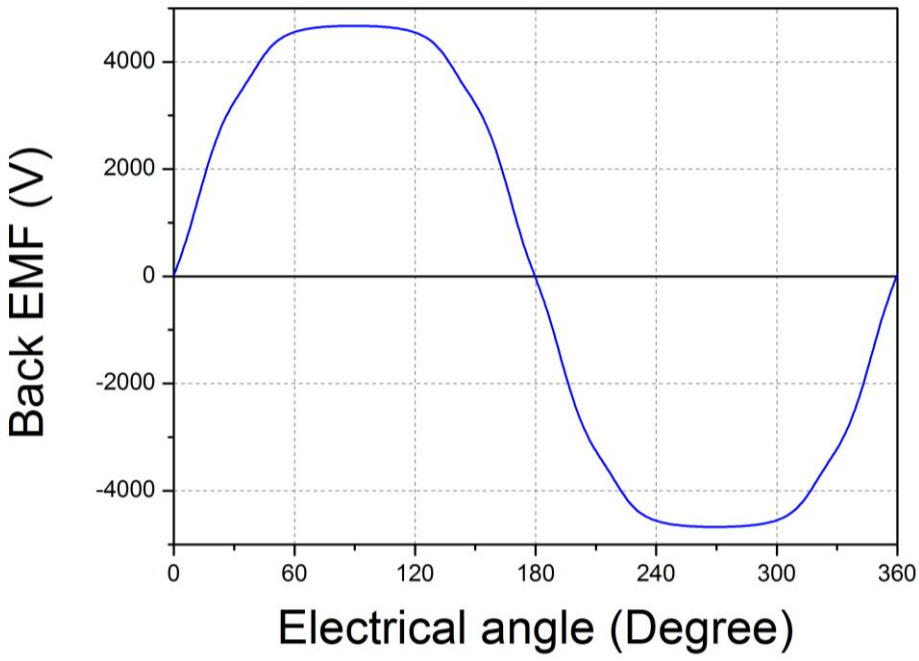


Figure 3.14: Back EMF waveform of the 1 MW YASA machine generated from the analytical method.

3.5.6 Cogging Torque

Cogging torque causes speed pulsations, vibration and acoustic noise. This occurs due to the rotor attempting to line up with the stator cores in a particular direction and hence the permeance of the air gap seen by the magnets is reduced. The cogging torque of the YASA machine can be calculated with a virtual work method using the air gap flux density (Barakat et al. 2001),

$$T_{cog} = \frac{\partial W}{\partial \theta} = \frac{1}{2\mu_0}\frac{\partial}{\partial \theta}\left(\iiint {B_{ag}}^2 dV\right) \tag{3.55}$$

where W is the total air gap coenergy, θ is the electrical angle and V is the air gap volume. The cogging torque waveform of the 1 MW YASA machine is shown in Figure 3.15.

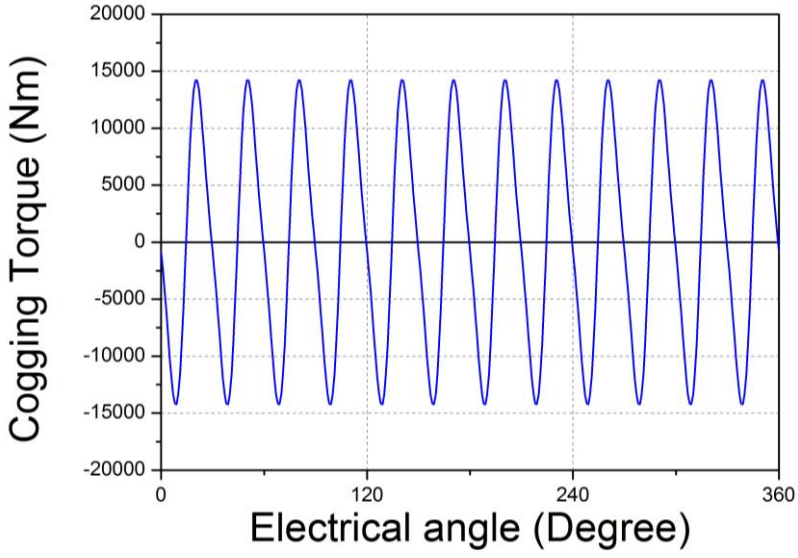


Figure 3.15: Cogging torque waveform of 1MW YASA machine that generates with analytical method.

3.6 Comparison of a MW-scale YASA machine with the transverse flux and radial flux machines.

Table 3.13: Table of comparison of YASA, TFPMG-U and RFPM generators.(Light blue cells are constants)(Bang & Polinder 2010)

Type of generator	TFPMG-U	RFPMG	YASA	TFPMG-U	RFPMG	YASA
Rated Power (MW)	5	5	5	10	10	10
Turbine rotor diameter (m)	126	126	126	178	178	178
Rated rotor speed (rpm)	12.1	12.1	12.1	8.6	8.6	8.6
Outer diameter of generator (m)	6.370	6.370	6.370	8.699	8.699	8.699
Axial length of generator (m)	1.030	1.720	0.207	1.464	2.610	0.326
Air gap length of generator (mm)	6.360	6.360	6.360	8.680	8.680	8.680
Magnet height (mm)	25.400	15.900	13.800	34.700	21.700	41.100
Number of phases	3	3	3	3	3	3
Number of slots per pole per phase	0.134	1	0.2	0.2	1	0.2
Pole pitch (mm)	63.6	100.0	100.0	86.9	99.7	97.6
Number of pole pairs	157	100	100	157	137	140
Rotor pole width (mm)	50.90	80.00	68.40	69.50	80.00	70.30
Stator slot width (mm)	80.80	15.00	63.40	94.40	14.96	65.10
Stator tooth width (mm)	130.40	18.00	42.60	196.80	18.00	47.90
Stator slot height (mm)	80.80	80.00	127.00	94.40	80.00	181.00
Stator yoke height (mm)	130.40	40.00	0.00	196.80	40.00	0.00
Rotor height (mm)	130.40	40.00	15.50	196.80	40.00	19.00
Air gap area (m^2)	20.47	34.29	23.25	39.93	71.04	38.04
Nominal current (A)	606.20	606.20	606.20	551.90	551.90	551.90
Number of conductors per slot (turns)	20.98	3.35	6.00	31.46	3.35	6.77
Peak air gap flux density (T)	1.59	0.97	0.77	1.60	1.07	0.93
Volume (m^3)	20.61	34.42	4.15	40.01	71.33	8.90
Active materials weight (ton)						
Iron	23.61	32.97	21.00	67.51	68.21	51.13
Copper	2.29	7.49	8.26	4.27	14.96	13.46
PM	8.11	3.31	4.40	23.89	9.37	21.40
Generator active materials	34.02	43.78	33.66	95.66	92.55	86.00
Components cost (k€)						
Copper Cost	34.41	112.37	123.92	64.04	224.42	201.93
Permanent magnets cost	324.56	132.56	175.90	955.52	374.96	856.12
Iron cost	70.84	99.00	63.01	202.52	204.63	153.40
Total active materials cost	429.81	343.93	362.84	1222.07	804.01	1211.45

This case study compares the YASA generator with single-sided transverse flux permanent magnet generators with U-core (TFPMG-U) and slotted surface-mounted radial flux permanent magnet generators with C-core (RFPMG) based on the criteria of the volume, the active material weight and the active material costs. These two generators are mainly designed for wind turbine applications with power ratings of 5 MW and 10 MW. Both the TFPMG-U and RFPMG are optimised and verified by Bang & Polinder (2010).

In order to have a fair comparison between different topologies, the rated power, the rated speed, the outer diameter, the air gap length, the current density and the unit cost of the active materials remain constant. The values of these parameters and the comparison parameters of each generator topology under 5 MW and 10 MW are shown in Table 3.13.

It can be seen that the YASA machine is the smallest in volume and lowest in active material weight. The YASA machine is about 88% smaller in volume than the conventional radial flux machine and about 78% smaller than the transverse flux machine. This is because under a constant outer diameter, the axial length of the transverse flux machine is around 5 times longer than the YASA machine. While the axial flux length of the radial flux machine is around 8.3 times longer than that of the YASA machine. Although the YASA machine is 7% lighter than the radial flux machine but YASA machines cost 50% more in active materials. This

is because the diameter of the YASA machine is restricted to be the same as the radial flux machine, and hence it requires more permanent magnets to generate more power.

3.7 Summary

An analytical design tool considering the electromagnetic and structural designs is developed to assist the design of a megawatt-scale YASA generator for direct-drive wind turbines. A design reference map was generated to graphically present the relationships between different machine parameters. For design optimisation, a pseudo-weight vector approach is developed giving a machine designer the freedom to place a weight on each parameter based upon application requirements. An optimised model was chosen for further studying its electromagnetic performance including the efficiency, the air gap flux density, the winding layout, the cogging torque and the back EMF using the analytical methods. Comparison of the YASA machine with other machine topologies show advantages of applying the YASA topology to MW-scale generators for wind turbines. The finite element study of the electromagnetic design will be carried out in the next chapter to compare with the analytical results.

Chapter 4 – Electromagnetic Design

This chapter studies the electromagnetic properties of a 1 MW YASA generator using the finite element method. The analytical study has produced an optimised YASA design, which is an initial model to be created in the 3-D finite element method (FEM). The inherent 3-D electromagnetic structure of an axial flux machine is more appropriate to be studied with the 3-D FEM as the flux cannot be fully modelled on a single plane. This study generates the electromagnetic performance of a MW-scale YASA generator for the first time. The FEM in this chapter has three purposes: 1) to verify the analytical calculations; 2) to determine the electromagnetic performance of a MW-scale YASA topology when the 3-D geometry is considered; 3) to optimise the geometries of the electromagnetic components to achieve the best performance.

The YASA topology has been previously studied with the FEM by Woolmer (2009) on a much smaller scale (50 kW), high-speed machine with only 5 pole pairs and 12 stator slots. The MW-scale YASA is a low-speed machine and therefore the numbers of poles and slots have to be increased to achieve a high torque density. The 1 MW YASA generator is designed to have 50 pole pairs and 120 stator slots. This results in a machine with a large diameter. A model with a large diameter-to-

axial length ratio poses a big challenge to using fine meshing in the FEM. Therefore, assigning an appropriate mesh size to each machine component needs to be considered carefully to reduce the analysis time and to improve the accuracy. The machine performance data of the 1 MW YASA generator, such as the torque, the back EMF and the cogging torque are produced. The FEM was validated with the existing 50 kW prototype. At the end of this chapter, a new low cost method to fabricate segmented stator cores with laminated electrical steel is proposed.

4.1 Finite element modeling, boundary condition and meshing

The finite element modelling of the electromagnetic behaviour of the YASA generator was performed on a commercial software package, Opera 3D (Cobham Technical, 2012). The magnetostatic and electrostatic fields are analysed using a static solver, TOSCA. The TOSCA solver can also be used to rotate the machine by using a position stepping analysis to calculate the waveforms of back EMFs and torques. The process of Opera 3D is divided into three stages - a geometries modeller, a pre-processor and a post-processor.

To model a MW-scale YASA generator is a challenging task. In an electrical machine, the air-gap is an important part to be modelled to analyse the magnetic flux density. Therefore, the air-gap is expected to be modelled with a smallest possible mesh size. However, the ratio of the largest to the smallest features (ratio of features) of the MW-scale YASA machine is large. The largest feature is the

machine diameter (4.64 m) and the smallest feature is the air gap (5 mm). This results in the 1 MW YASA machine having a ratio of features of 928, nearly 7 times larger than that of the 50 kW one. As the mesh size should be close to the smallest dimension of the geometric feature to avoid a high aspect ratio (Figure 4.1). In the case, the maximum mesh size for modelling the air gap is 5 mm and the air gap is sectioned to avoid forming high aspect ratio meshes at the larger surfaces of the air gap. In addition, a large mesh size transition at the boundary can produce numerical error, and hence for two neighbouring components, the mesh size should be similar. For example, the magnet next to the air gap has a thickness of 30 mm. Transition errors have occurred in meshing when 30 mm was used, while when 5 mm mesh size is used for this less important geometry, it generates an unnecessarily large amount of elements, leading to considerable increase in computational time. The ability to compute such a large number of elements is limited by the available computing capability, mainly the core frequency of the central processing unit (CPU) and the amount of the random accessed memory (RAM). After multiple trial-and-error experiment, a mesh size setting for each component are carefully chosen (Table 4.1). This is determined by the smallest mesh size that the computer can perform simulation. This will yield 300,000 elements on a 1 MW model. On a computer with an Intel Core™ i7 3.4 GHz CPU and 16 GB RAM, this takes about 5 hours for the analysis to complete. To simulate a full 360° electrical angle, the machine needs to be rotated by 7.2° mechanical

angle. To obtain a reasonably smooth curve requires at least 18 data points. This takes about a total of 4 days to compute. When a current density is applied to the windings to simulate full load condition, the computational time increases significantly. To reduce the computing demand, modelling only 1/10 of the model is sufficient, as the rest of the model is symmetrical (Figure 4.2).

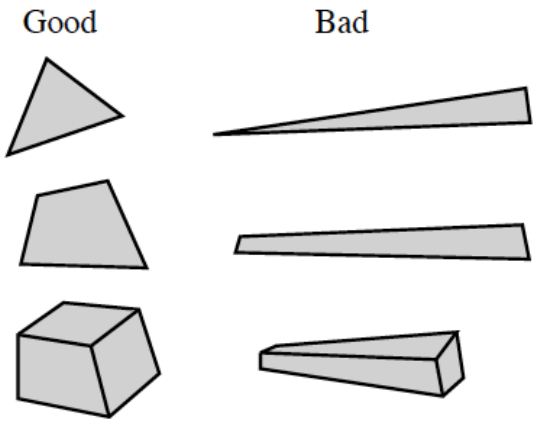


Figure 4.1: meshing elements with low and high aspect ratios (University of Colorado at Boulder 2013).

Table 4.1: Mesh size comparison between modelling the 1 MW YASA and the 50 kW YASA.

Component	1 MW	50 kW
	Mesh size (mm)	Mesh size (mm)
Stator cores	5	2
Stator reduced air	10	6
Air-gaps	5	1.5
Permanent magnets	10	2
Rotor air	15	6
Rotor back iron	10	2

Setting correct boundary conditions in the FEM is important. A boundary condition can 1) create symmetrical models, 2) approximate the magnetic field at large distances from the model, 3) provide the voltage or current drive of the model and 4) represent the material inside a boundary (Cobham Technical Services 2012). The boundary conditions imposed on this model are Dirichlet boundary condition, Neumann boundary condition and rotational symmetry as shown in Figure 4.3. The Dirichlet boundary condition (Ida 2000) is applied to the outer surface of the model to fix the magnetic vector potential to a prescribed value and force flux lines to be parallel to the boundary edges, hence no flux leakage beyond the surface. The Neumann boundary condition (Ida 2000) is applied to the centre of the stator cores as shown in Figure 4.3. It sets the symmetry of the machine along Z-axis with opposite polarities, as the magnetic potential on both side are the same. The magnetic vector potential along this line is equal to zero. Rotational symmetry boundary condition is applied to the left and right of this model as seen in Figure 4.3. This boundary condition forces the potential vector either the same as the part that wants to be symmetry (positive) or in the opposite way to that part (negative). This boundary condition is very useful especially for a large machine to reduce it into a small fraction during meshing and analysing. In this model, the rotational symmetry is set as positive and 1/10 of the model will be periodically rotated to form a full model.

The red components in Figure 4.2 are the stator windings of the YASA machine. The windings used in the TOSCA solver are Biot-savart conductors with a pre-defined current density, which is evenly distributed over the cross-section surface of the conductors. The conductors are not part of the mesh.

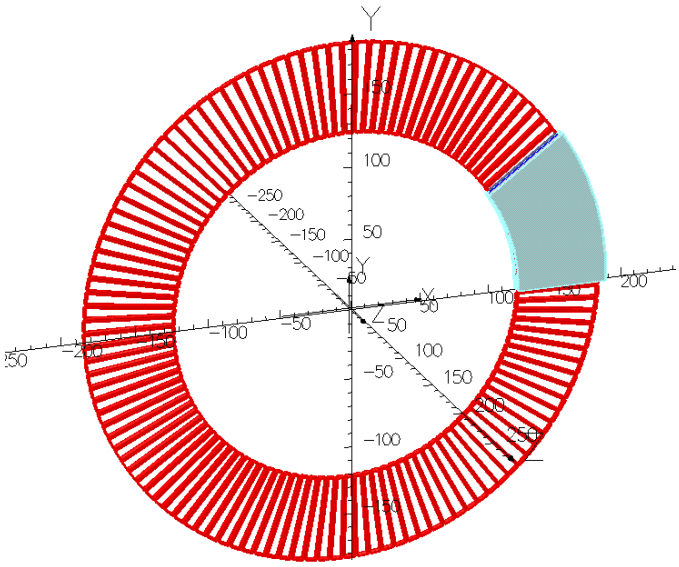


Figure 4.2: The 1 MW YASA generator modelled in the geometries modeller of Opera 3D. The shaded part is 1/10 of the model section.

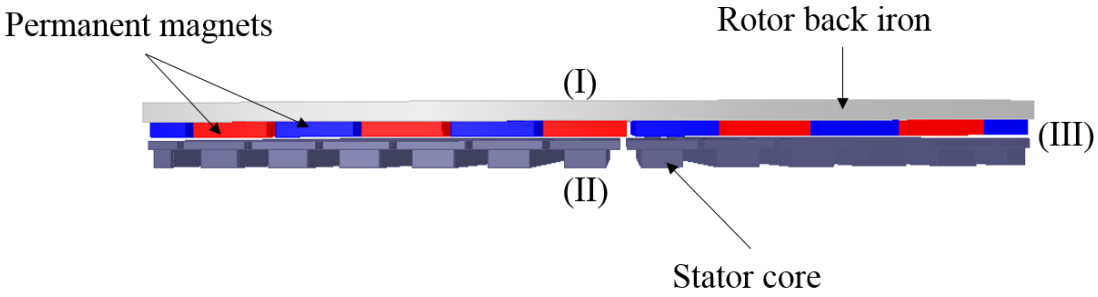


Figure 4.3: 1/10 of the 1 MW YASA machine without windings. Dirichlet boundary condition applied on area (I), Neumann boundary condition applied on area (II) and rotational symmetry applied on (III).

4.2 Flux density allowance on the magnetic materials

In the FEM optimisation of the 1 MW YASA machine model, the no-load flux density is limited to 1.8 T, well below the saturation point of the electrical steel (M270-35A) 2.35 T, while the full-load flux density limit is set to 2.1 T. Figure 4.4 shows the flux densities of the stator cores of the 1 MW YASA machine.

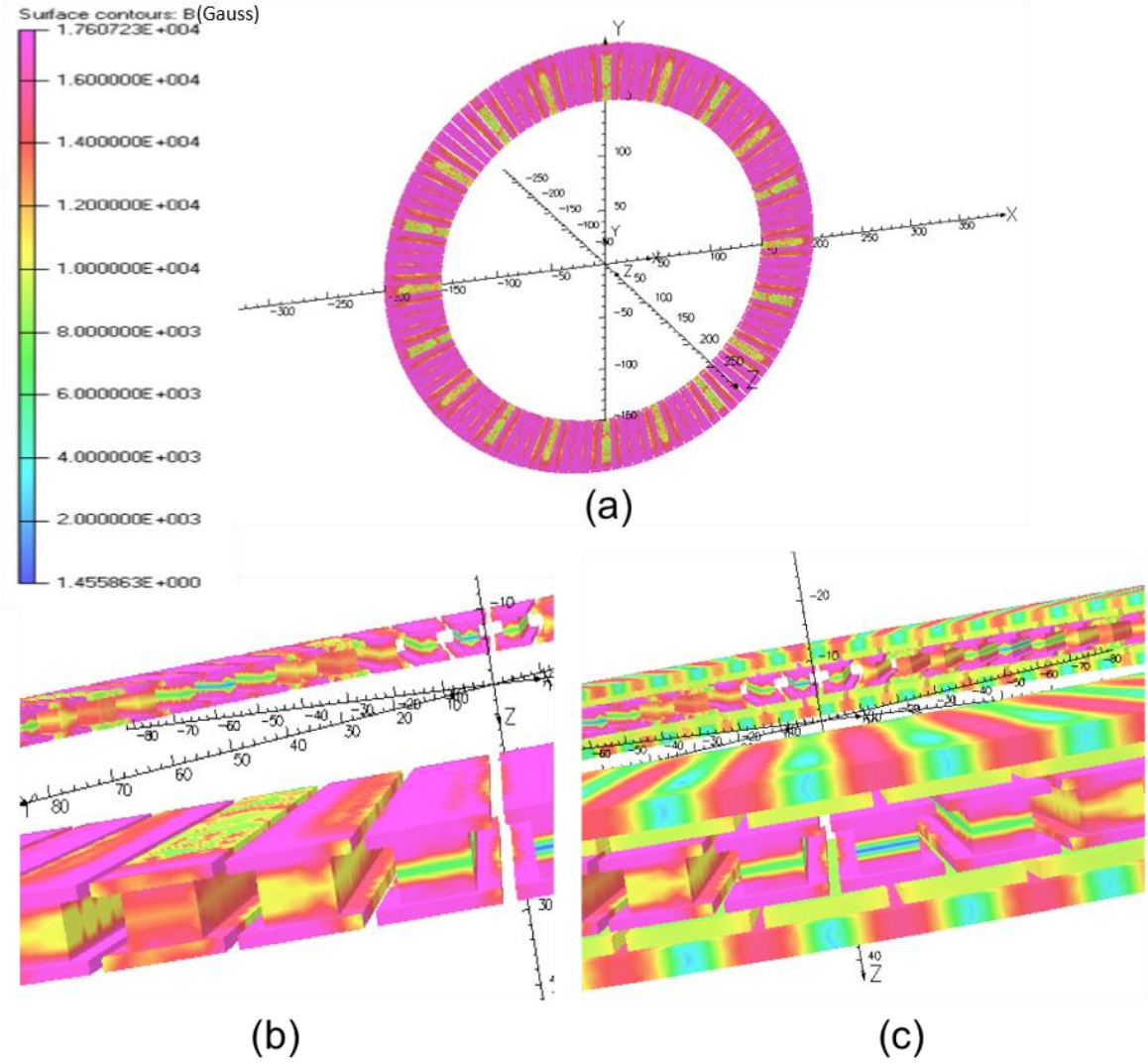


Figure 4.4: (a) Contour display of the flux density of the full stator produced in the 1MW YASA machine under a no-load condition; (b) contour display of no-load flux density of a section view of the stator cores only; (c) contour display of the no-load flux density of a section view of the YASA machine.

The maximum no-load flux density produced by this model is just below the set limit. Therefore, no adjustment to magnetic parts is needed. However, in many cases, analytical calculations would overestimate the flux density allowed to enter the stators as it does not consider the geometric variation of the stator cores, the flux leakage and non-linear material behaviours as the FEM does. Further iterative optimisation would then be required by altering the thicknesses of the stator cores, the permanent magnets or the axial length of the air gap. It is important to ensure that the alteration keeps the flux density below saturation and does not lower the torque performance of the machine.

4.3 No-load steady state electromagnetic analysis

This section studies the no-load electromagnetic behaviours of the 1 MW YASA machine, including the air- gap flux density, the back EMF and the cogging torque. Under no-load condition, the current density of the windings is set to zero.

4.3.1 Air gap flux density

The air gap flux density is measured at the mid-air gap on a circle along the circumference of the YASA machine (Figure 4.5). The circle is on the middle of the depth of the stator core, and has a radius of $(D_{out}+D_{in})/2$.

The air gap magnetic flux density of the 1 MW YASA machine obtained from both the FEM and the analytical calculation is shown in Figure 4.6. The

waveforms obtained from both methods follow a same trapezoidal waveform, with notches appearing at the exact locations where the slotting of the stator cores occur. There is a 14% deviation between both methods. In the FEM simulated waveform, there are extra notches near the slots due to fringing flux leakage at the slotting, while the analytical method has assumed that in the effect of slotting, all leakage flux is following a circular arc into the stator cores. The flux density of the 50 kW machine in Figure 4.7 shows less deviation between the analytical and the finite element methods due to less leakage flux as a result of smaller stator slots.

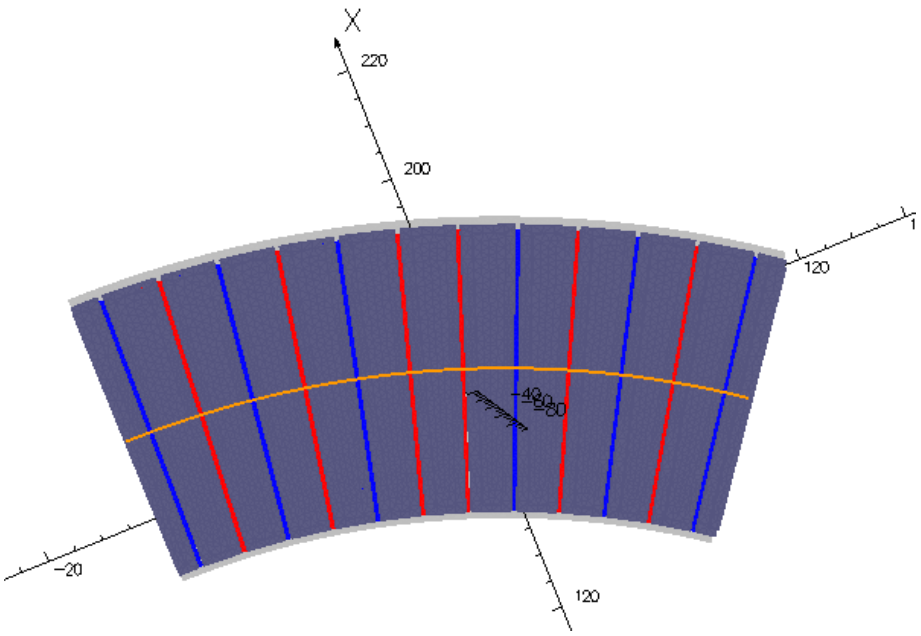


Figure 4.5: The circle line in the average radius of the machine for the flux density measurement.

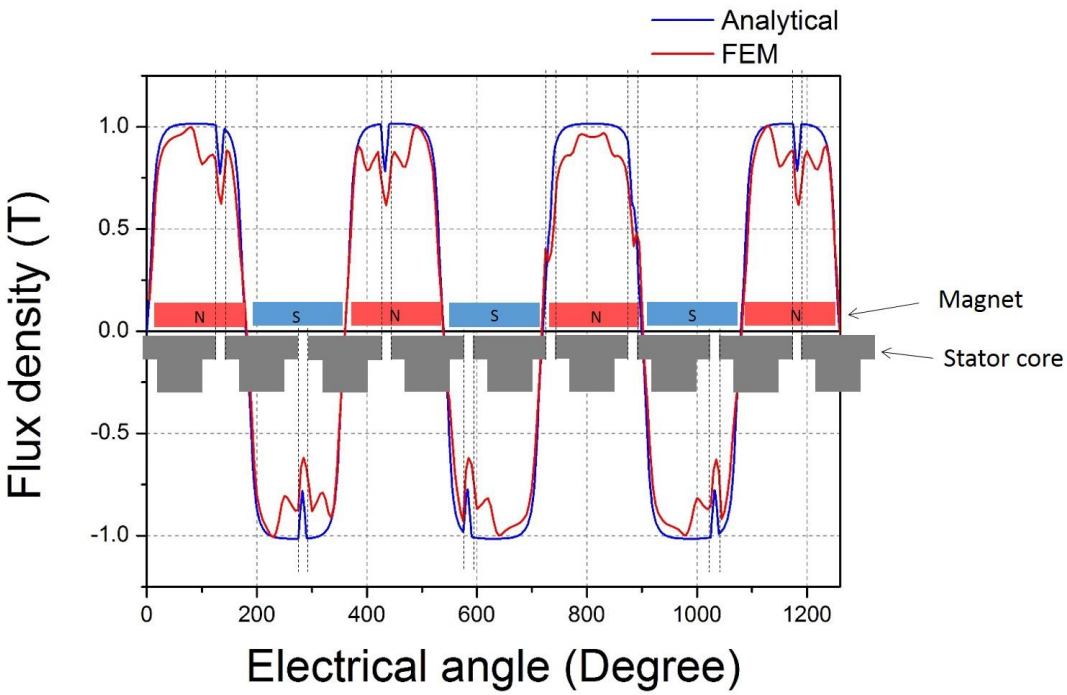


Figure 4.6: The air gap magnetic flux density of the 1 MW YASA machine.

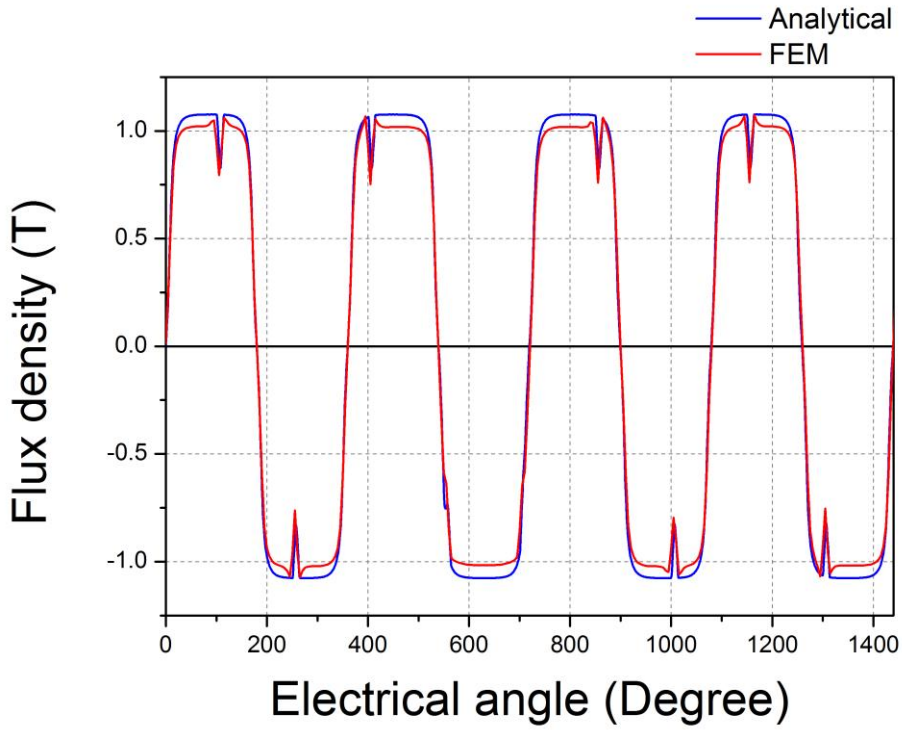


Figure 4.7: The air gap flux density waveforms of the 50 kW YASA machine.

4.3.2 Back EMF waveforms

The induced back EMF waveform of the 1 MW YASA machine can be calculated from the flux linkages at different angular positions of the rotor. The flux linkage of a stator core is calculated by integrating the Z-component flux densities over an area of a polar patch that mirrors the shape of the stator core (Figure 4.8). The static analysis solver, TOSCA, enables the computation of the flux linkage at each rotating angle, by snapshotting the fields in the machine.

The back EMF is calculated by,

$$EMF = N_{turn} \cdot \frac{d\phi}{d\vartheta_e} \cdot \omega \tag{4.1}$$

where N_{turn} is the number of turn of the stator windings, which is 29, φ is the flux linkage, ϑ_e is the electrical angle and ω is the rotational speed (25 rpm) of the machine in rad per second. The comparison of the back EMF waveforms between the analytical approach and the 3-D FEM is shown in Figure 4.9. The waveform obtained from the FEM generally follows a trapezoidal shape with some departure from the analytical one. The most apparent difference is that the FEM simulated waveform shows harmonics, which can be caused by the slot harmonics (Dosiek & Pillay 2007).

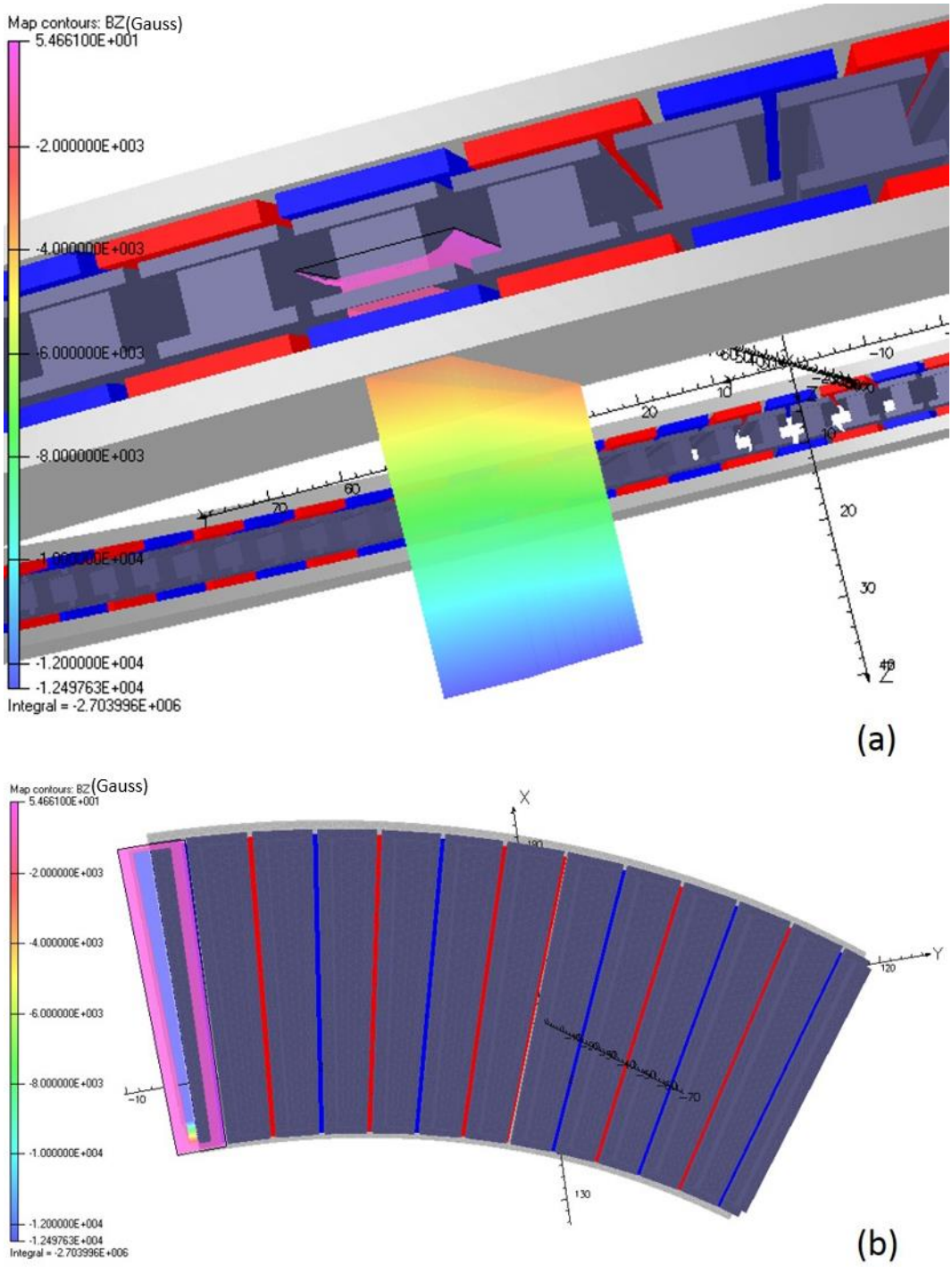


Figure 4.8: (a) Polar patch of Z-component of surface of a stator core; (b) a polar patch (in pink) of Z-component of surface of a stator core.

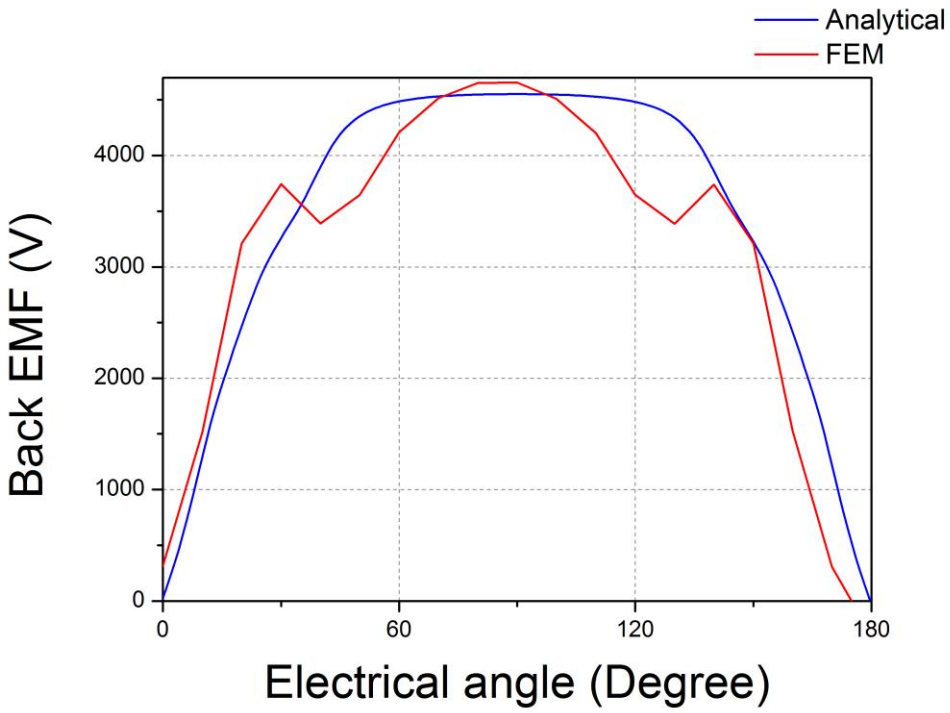


Figure 4.9: Comparison of the back EMF waveforms of the 1 MW YASA machine between analysis from the analytical and the FEM methods.

4.3.3 Cogging Torque

The cogging torque of the YASA machine can also be computed by integrating the Z-component Maxwell stress of the rotors and the permanent magnets. The cogging torque of the 1 MW YASA machines is shown in Figure 4.10 and compared with the analytical result. The cogging torque produced by the FEM shows a similar waveform of the one calculated from the analytical method, except that the analytical result shows higher amplitude. The difference may be due to the saturation effect of different parts of the stator and also a more detailed account for the slotting effect by the FEM. The cogging torque waveform from the FEM is sharp due to a relatively large distance between each data point that was taken.

The graph is constructed from only 18 data points across 180° electrical degree, as this is limited by the computer resource. For a fast comparison, the analytical method has certain advantage over the 3-D FEM and can generate results with reasonable accuracy (Barakat et al. 2001; Zarko et al. 2008). According to the FEM results, the 1 MW YASA machine has produced a large peak cogging torque of 20,000 Nm. It is possible to reduce the cogging torque by 1) using parallel teeth instead of trapezoidal teeth; 2) alternating the pole-arc ratio of the permanent magnets; 3) skewing of the stator teeth or the magnets (Aydin et al. 2003; Chuang 2009; Eom et al. 2001; Wanjiku et al. 2011). The comparison of the cogging torque between the FEM and the analytical results of the 50 kW machine is shown in Figure 4.11.

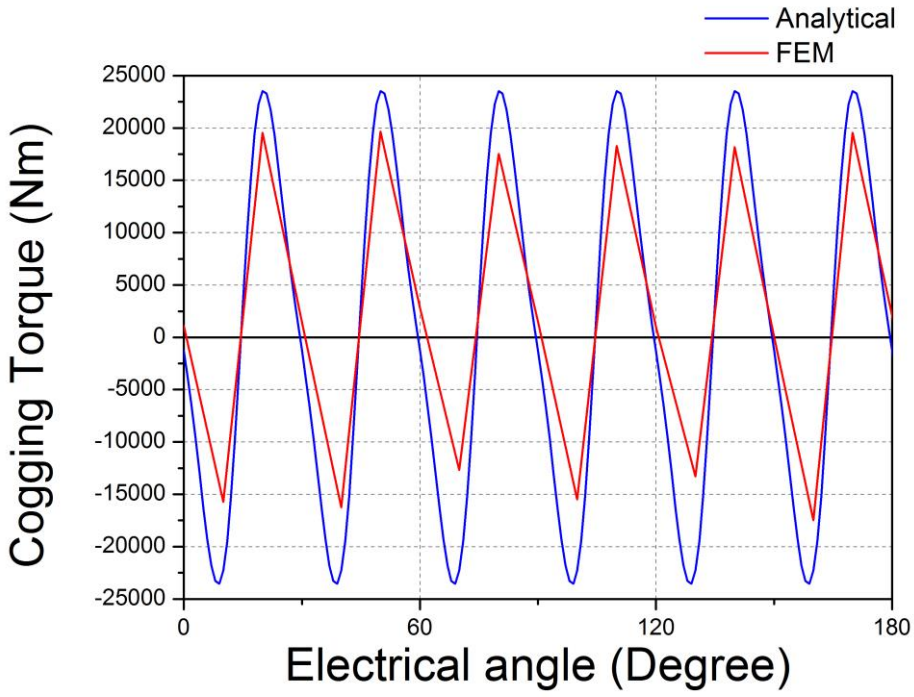


Figure 4.10: Cogging torque waveform of 1MW YASA calculated with FEM.

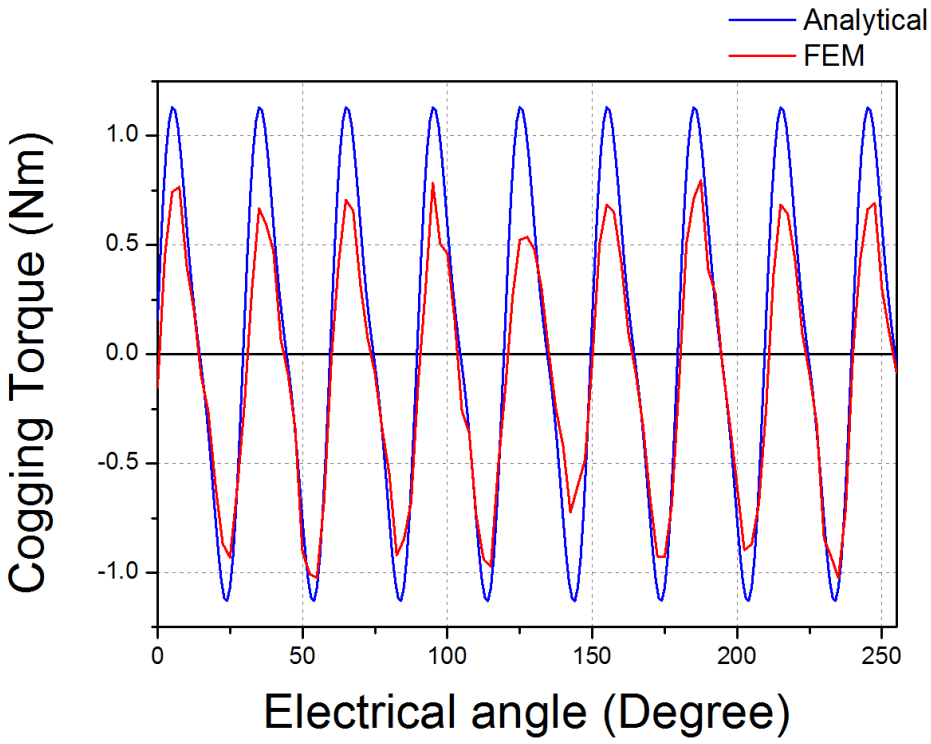


Figure 4.11: Cogging Torque waveform of 50kW YASA calculated with FEM.

4.3.4 Validation of FEM with an existing 50 kW YASA machine.

In order to validate the FEM of the 1 MW YASA model, a 50 kW YASA FEM model is created to compare with an experimental study. The dimensions and materials used to create this model is based on the existing prototype.

A schematic diagram of the experimental set-up to measure the electromagnetic properties of the YASA prototype is shown in Figure 4.12. This testing set-up has two same size YASA machines connected in series via a torque sensor. One of the YASA machine works as a motor to rotate the other YASA machine that works as a generator. The motor speed is controlled by a power

regulator that regulates a three-phase voltage and can obtain speed feedback from an optical speed sensor.

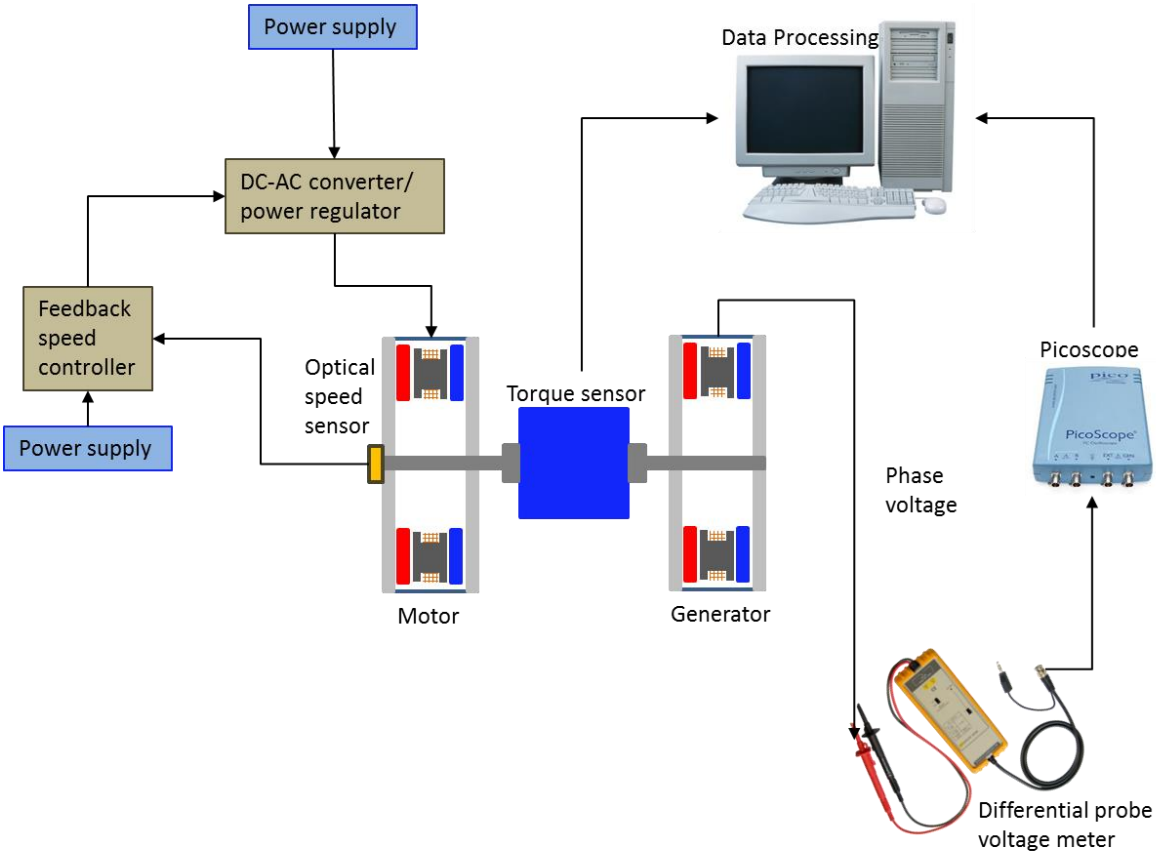


Figure 4.12: Schematic diagram of the experiment set-up to measure the back EMF waveform of the 50 kW YASA prototype.

In this experiment, the YASA generator is rotated at 200 rpm. The rotational speed is measured with a torque sensor while the phase voltage is measured with a differential probe voltage meter and logged with a picoscope. The phase back EMF is collected by connecting a voltage meter to the neutral point and a terminal of one phase. The no-load phase back EMFs of the 50kW YASA machine at 200 rpm are shown in Figure 4.13. The result shows that the FEM and experimental

waveforms are very similar in shape and magnitude with 4% discrepancy in peak magnitudes. The small deviation is likely due to the discrepancy between the actual air gap length and the designed length. Nevertheless, it is not possible to measure the air gap length on the prototype without tampering with the machine enclosure. An increase in temperature of the NdFeB permanent magnet during measurement may also cause reduction in remnant flux and the energy product produced by the magnet. The analytical waveform shows 14% deviation in magnitude from the experimental results. The result can be improved by introducing a leakage coefficient(Hwang & Cho 2001). Nevertheless, the deviation is acceptable as a preliminary design method and it has accurately predicted the shape of the waveform without heavy computing.

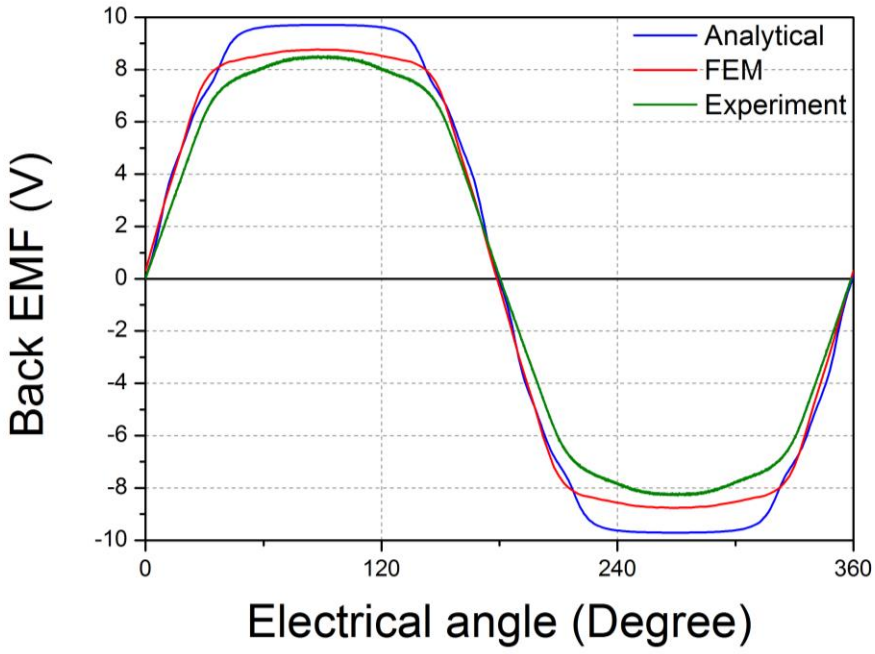


Figure 4.13: Comparison of the back EMF waveforms of a 50 kW YASA between analytical, FEM and experimental methods.

4.4 Full-load steady state electromagnetic design

4.4.1 Saturation of iron under full load condition

Under full-load condition, the flux density will increase with the applied current density. The flux density in the stator cores must not be higher than the saturation point (2.35 T) of the electrical steel (M270-35A). The applied current density is 6×10^{-4} A/m^2. The flux density of the 1 MW YASA machine under full-load condition is shown in Figure 4.14. The peak flux density is 2.23 T. This means that there is some space to increase the current density before it reaches the saturation point. However, whether or not the increased current density demanding better cooling system will also need to be considered. This will be discussed in Chapter 6.

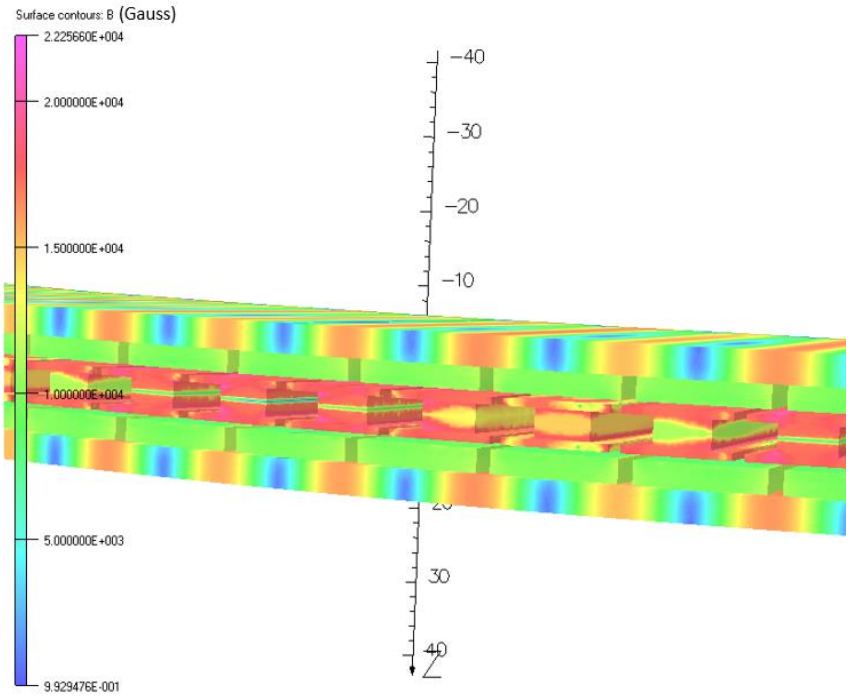


Figure 4.14: Coutour of the flux density under full-load condition.

4.4.2 Magnetic attractive force

The attractive force between the permanent magnets and the stator cores can be computed by integrating $B_z^2/2\mu_0$ on the mid-plane of the air gap in the post-processor. The mid-plane of the air-gap is generated with a polar patch function and this is essential to ensure that the coverage area captures all the flux that is passing through the air gap from the permanent magnets to the stator cores.

The magnetic attractive force calculated with the FEM of the 1 MW YASA machine with an outer diameter of 3.64 m and an air gap flux density of 0.96 T is 1.3×10^6 N. While the magnetic attractive force calculated with the equation (3.29) is 1.74×10^6 N. As expected, there is a high discrepancy of around 30% between both methods. This is because the classical analytical method does not consider 1) the leakage flux at the edge of the magnet; 2) the slotting effect of the magnet and 3) the slotting effect of the stator cores.

4.4.3 Torque

Static analysis of the torque produced by a machine with an applied current density can be computed using an integral of the Z component of the Maxwell stress over a polar patch along the whole air gap. Figure 4.15 shows the curve of the torque at different electrical angles. The torque decreases with fluctuations as the electrical angle increases, caused by the cogging effect. The maximum torque produced by the 1 MW YASA machine is 3.5×10^5 Nm and the cogging torque is

5.7% of the total torque. The full-load machine simulation requires long computational time. The number of data points taken is limited by the available computer resources. The simulated torque on the 50 kW YASA machine is shown in Figure 4.16.

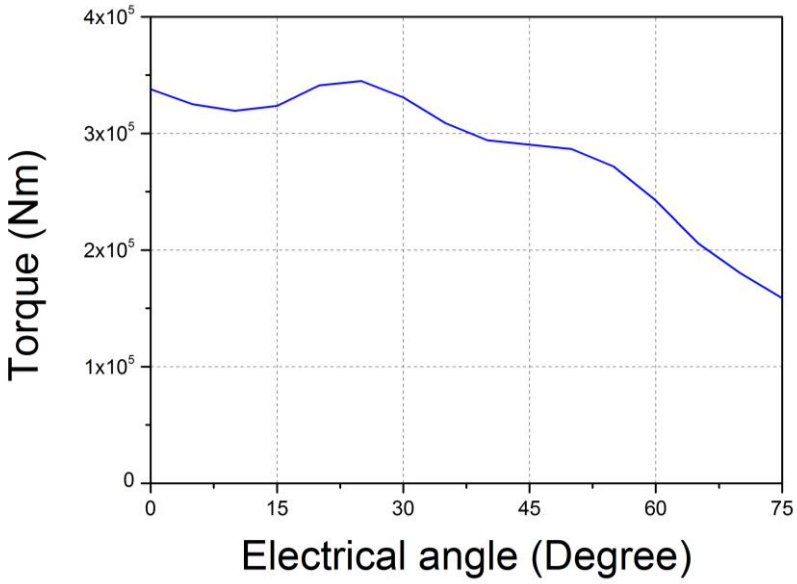


Figure 4.15: Torque waveform of the 1 MW YASA calculated with the FEM versus electrical angle.

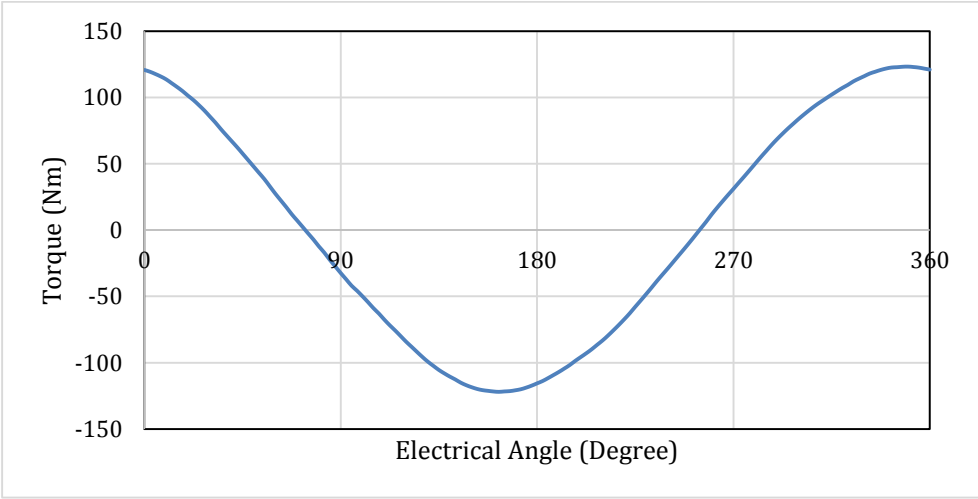


Figure 4.16: Torque waveform of the 50 kW YASA calculated with the FEM versus electrical angle.

4.5 Method to fabricate laminated stator core with electrical steel

The 50 kW YASA motor was designed using soft magnetic composite (SMC) as the materials for its segmented stator core (Figure 4.17). However, this is not a suitable material for a low speed generator as the iron losses is high at low frequency. For a MW-scale YASA generator, electrical steel is a more suitable material. However, the segmented shape of the stator cores in a YASA machine is quite difficult to fabricate with electrical steel. Although Fei (2011) proposed that it is feasible to manufacture a segmented stator core with laminated electrical steel, the author does not consider the manufacturing cost as the process requires different size of cutting moulds to shape all different proportionally sized electrical steel sheets. If this method is applied to manufacture such a long stator core of a MW-scale machine, the manufacturing cost will be considerably higher.

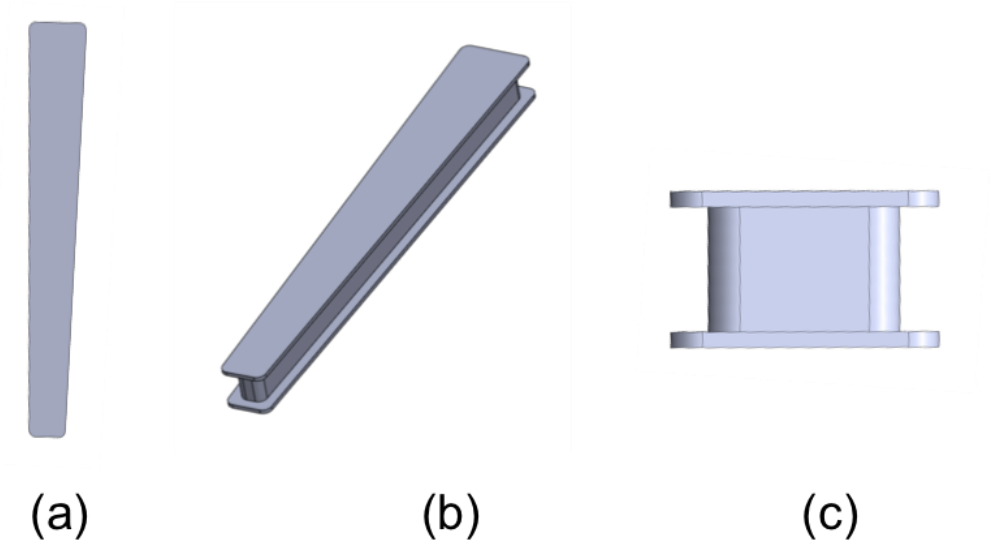


Figure 4.17: Stator core design with soft magnetic composite material. (a) Top view; (b) 2D view and (c) side view.

A new method is proposed here that can significantly reduce the number of moulds required. The stator core is divided into five or more sections with different width as shown in Figure 4.18. To manufacture each section, only a single size of the cutting mould is needed to fabricate each laminated layers. However, the disadvantage of this method is that by not having a continuous stator core reduces the coil packing factor and increases the length of windings.

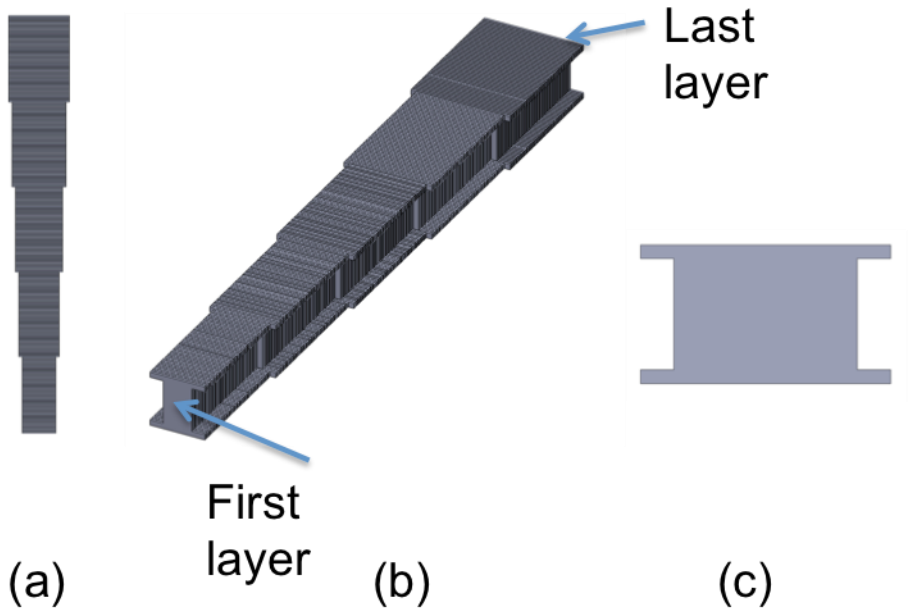


Figure 4.18: A low cost stator core design with laminated electrical steel.(a) top view; (b) 2-D view and (c) side view.

4.6 Summary

This chapter presents the 3-D finite element analysis of the electromagnetic performance of a MW-scale YASA generator. The parameters of an optimised YASA design were used to create a finite element model. The no-load flux densities passing through the magnetic materials are characterised and the maximum

amplitude is below the saturation limit. This is followed by analysing the air gap flux density, the back EMF and the cogging torque, which are used to validate the analytical results. To verify the FEM, a 50 kW model mimicking the existing prototype is created with the FEM and the simulated back EMF is compared with experimental data, which shows good consistency. The generator under full-load condition is also considered, and the generated torque and the magnetic forces are studied. Finally, a low cost method to fabricate the segmented stator core with electrical steel is proposed.

Chapter 5 – Structural Design

The stator of an axial flux machine is usually made of iron. There is a strong attractive force between the stator and the permanent magnets attached to the rotor, separated by a small air gap. Whether the magnetic force would act on both the rotor and the stator depends on the topology of the machine. A YASA machine has a stator positioned between the two rotor plates, on which permanent magnets were mounted. This arrangement results in two opposite attractive forces acting on the stator. The two opposite forces on the stator cancel out if it is positioned in the exact midway between the rotors (Mueller et al. 2005). However, the rotor plates are still subject to these strong attractive forces, which may cause deflection. In addition, the torque produced in a rotating MW-scale YASA generator is large and may also causes deformation of the rotor plates along the tangential direction. Therefore, the rotor plates should be designed with enough stiffness to withstand both attractive forces and torque, avoiding deflection and deformation. Increasing the structural stiffness of the rotor plate is essential. However, if this is simply done by increasing the thickness, extra weight will incur. Therefore, the focus of this chapter is to improve the design of the rotor plate structure, which can be structurally strong and light in weight.

Optimising the structural mass of the rotor plates using analytical calculations has been performed in Chapter 3. The parameters of this optimised design are used to create a rotor plate model in finite element software (Solidworks® Simulation). The model is shown in Figure 5.1. To reduce the weight of the rotor plates, a spider wheel is considered to reconfigure the rotor plate design. This design process is aimed at reducing the weight of the simplified rotor plates by at least 50%, while the structural deflection and deformation are within allowed limits.

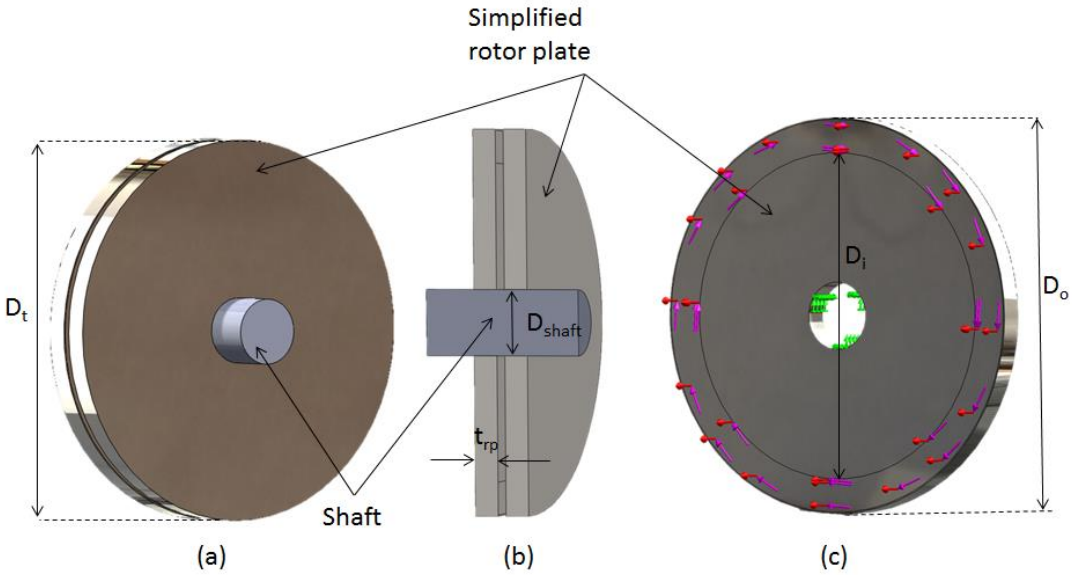


Figure 5.1: (a) 3-D model of two simplified rotor plates fixed onto a shaft; (b) cross-sectional view ; (c) a single simplified rotor plates fixed on the shaft (green arrows) with attractive forces (red arrows) and torque (pink arrows) applied.

5.1 Boundary conditions, meshing and convergence

For the static finite element analysis to simulate the deflection of rotor plates, three boundary conditions were used. The first boundary condition is that the

rotor plate is fixed onto a shaft (green arrows in Figure 5.1(c)) and the outer edge of the rotor plate is free to rotate. The second boundary condition is that the Maxwell stress from the magnetic force is applied uniformly to only the outer part of the rotor plate, to which the magnets are attached (red arrows in Figure 5.1(c)). The torque is also applied uniformly only to the outer part, which is shown as the pink arrows in Figure 5.1(c). The mesh size used for the simulation models is 80 mm with 4 mm tolerance. Using smaller mesh sizes to test convergence found that there is less than 0.01% difference in results.

5.2 Deflection simulation of rotor plates

A YASA machine is a double axial flux machine with two identical rotor plates holding permanent magnets (Figure 5.1 (a) and (b)). The attractive force applied to the rotor plate of the 1 MW YASA machine is around 1.428 MN and the torque is around 3.82 MNm. Simulating only one of the rotors should suffice, as both are symmetrical. The dimensions of the rotor plates and the properties of its material - carbon steel are listed in Table 5.1.

The thickness of the simple rotor plate was determined in Chapter 3 using the Roark's formula by giving a maximum deflection of 0.5 mm, which is 10% of the air gap length. The deflection effect of this rotor plate simulated with the FEM is shown in Figure 5.2. The maximum deflection is 0.496 mm, which is consistent with the analytical results, with only 0.8% difference. Though this deflection value

is within the allowance, the total weight of the two rotor plates is about 77.24 tons, 12.7 times heavier than weight of the active materials (6.08 tons).

Table 5.1: The material properties of Carbon steel and the dimensions of the simplified rotor plate. *(ASM International 1998)

Parameters	Values
Modulus of elasticity of carbon steel *	2.1×10^{11} N/m^2
Poisson's ratio of carbon steel *	0.28
Density of carbon steel *	7800 kg/m^3
Thickness of the plates, t_{rp}	0.2887 m
Total diameter of the rotor plate, D_t	4.67 m
Outer diameter of the rotor plate, D_o	4.64 m
Inner diameter of the rotor plate, D_i	3.85 m
Diameter of shaft, D_{shaft}	0.8 m

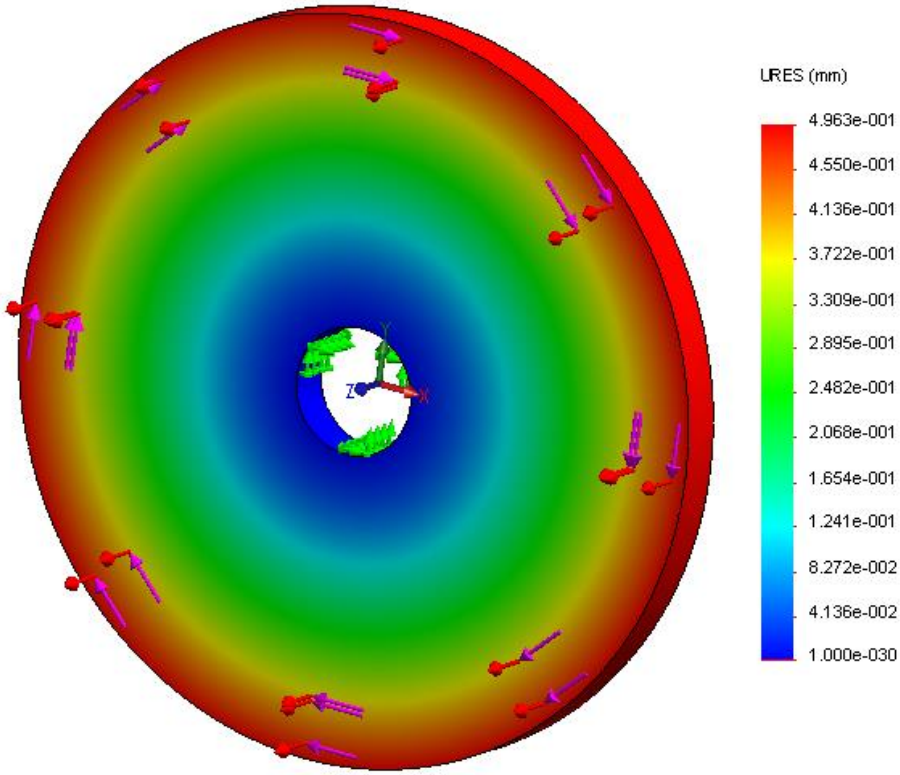


Figure 5.2: Deflection effect of the simplified rotor plate.

5.3 Improving the rotor plate design

For an axial flux YASA machine, the inner part of the rotor plate is not a part of the electromagnetic circuit (Figure 5.3) and it is only used for structural purposes. Therefore, the weight can be reduced by removing some materials from the inner part and this would not have any negative effect on the electromagnetic performance of the machine. A design, inspired by the spider wheel structure is considered here to replace the flat plate structure (Figure 5.4). The boundary conditions to simulate this spider wheel design remain the same. To adapt the spider wheel design to a rotor plate, the number of spokes and their dimensions need to be determined.

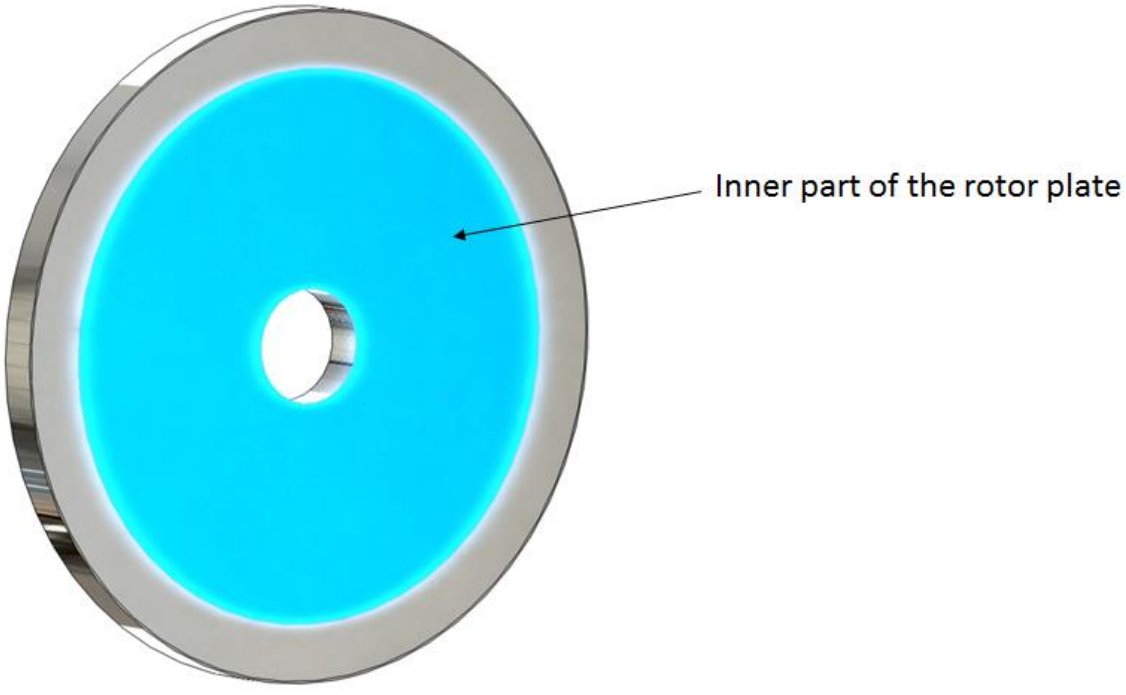


Figure 5.3: Inner part of the YASA rotor plate which does not form part of the electromagnetic circuit.



Figure 5.4: An example of a spider wheel.

5.3.1 Determining the number of spokes

The arrangement of spokes should fulfil the following requirements: 1) the centreline of a spoke should align with the centreline of a permanent magnet such that the resultant magnetic forces are balanced on both side of the beam. Otherwise, the spokes will be subject to torsion due to the forces of different pole directions; 2) the beam should be uniformly distributed along the wheel such that the forces applied to each individual beam is the same. Based on the above requirements, there are only five possible spoke arrangements for a 100-pole YASA generator, shown in Figure 5.5.

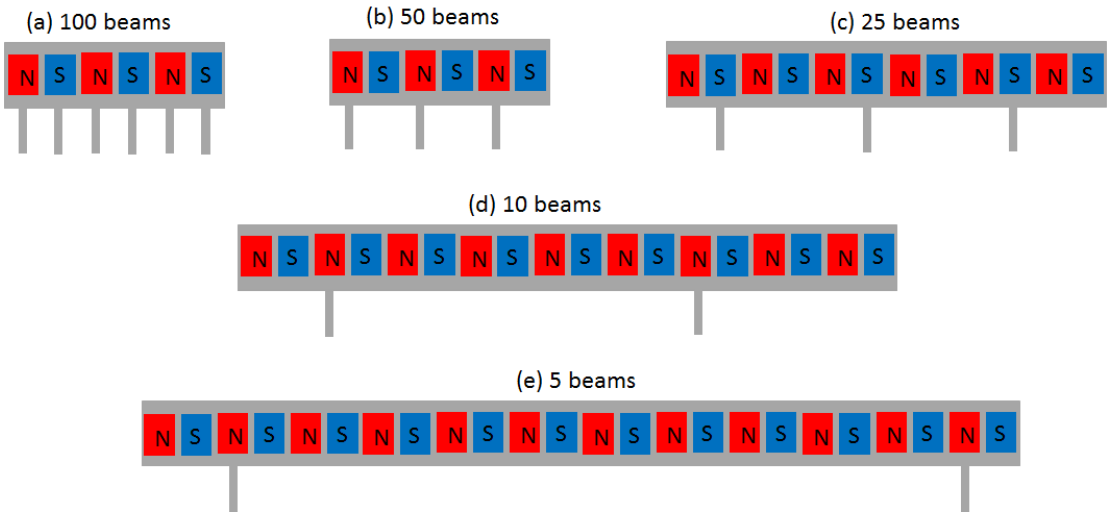


Figure 5.5: The possible spider-wheel spoke arrangements for a 1 MW YASA generator with 100 poles (a) 100 spokes; (b) 50 spokes; (c) 25 spokes; (d) 10 spokes; and (e) 5 spokes.

5.3.2 Analysis of spoke dimensions

The optimal spoke arrangements and the dimensions of each spoke are to be determined, such that a spider wheel will use the least amount of materials to achieve the structural requirement. An extreme condition is considered here that the spoke has one end fixed onto an un-rotatable shaft, while the outer side near to the permanent magnets is free (Figure 5.7). In this scenario, the spoke is analogy to an elastic straight beam that one end is free and the other end is fixed. Roark's formula (Young & Budynas 2002) for this scenario are employed to calculate the maximum deflection and the maximum normal stress of the beam. The maximum deflection of an elastic straight beam is given by (Young & Budynas 2002),

$$y_{max} = -\frac{Wl^3}{3EI} \tag{5.1}$$

where W is the load (force), l is the length of the beam, E is the elastic modulus of the beam material, and I is the area moment of inertia about the centroidal axis of the beam cross section. The moment of inertia of a rectangular beam is given in equations (5.2) and (5.3) (Young & Budynas 2002) when d is greater than b.

$$I_x = \frac{1}{12} b d^3 \tag{5.2}$$

$$I_y = \frac{1}{12} d b^3 \tag{5.3}$$

where I_x is the moment of inertia with respect to the x axis, I_y is the moment of inertia with respect to the y axis, b is the width of the beam, and d is the depth or the thickness of the beam (Figure 5.6).

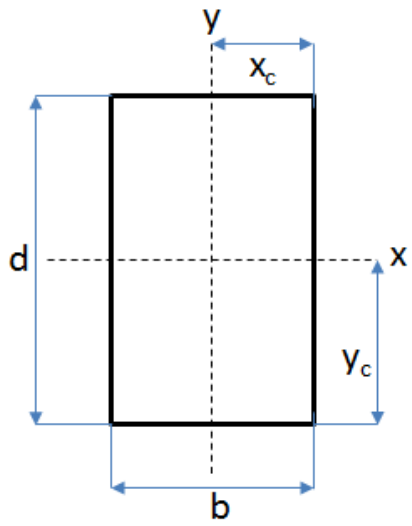


Figure 5.6: Cross-sectional diagram of a rectangular beam.

The maximum normal stress of the beam is given by,

$$Stress_{max} = -\frac{My_{max}}{I} \tag{5.4}$$

where M is the bending moment of a beam.

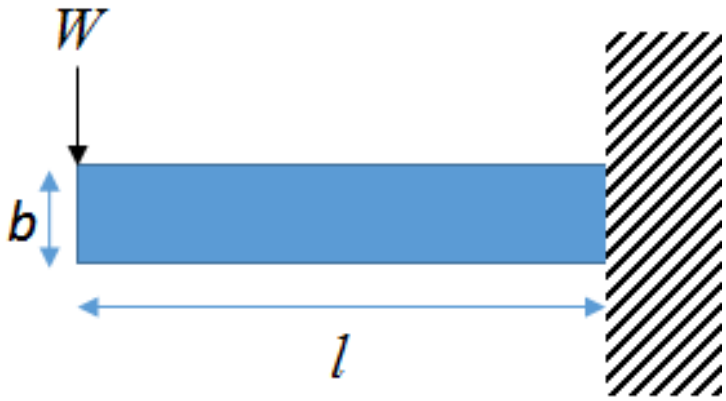


Figure 5.7: The straight beam right end is fixed on the shaft and left end is free. The force is applied to the left end.

There are two force distributions, one given by the attractive force, the other one providing torque. To simplify the calculation, the forces applied to the beam are analysed separately. The width of the beam (b) is limited by the size of the inner ring. The total width of all five beams should be equal to the circumference of the ring on the rotor plate (blue circle in Figure 5.8).

The maximum allowed deflection of the spokes is set to 0.415 mm and the maximum allowed normal stress is set to 1% of the yield strength of plain carbon steel. All possible deflection and normal stress of the spokes fulfilling this

requirement are calculated. As the length of the beams is limited by the diameter of the rotor plate, the calculation will only focus on the cross-sectional area ($b \times d$). For each possible arrangement, the designs with the smallest cross-sectional area are chosen and shown in Table 5.2 (attractive force) and Table 5.3 (rotational torque). In Table 5.3, a spider wheel with 100 spokes is not possible to achieve the allowance with rotational torque applied.

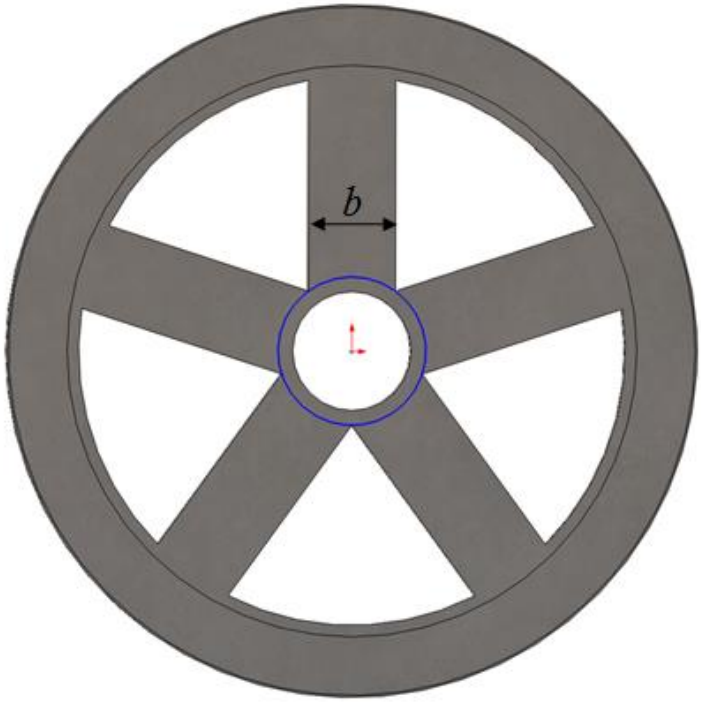


Figure 5.8: Front view of a 5–spoke spider wheel rotor plate.

The results show that a 5-spoke design requires the least amount of materials. Therefore, this design is chosen to be carried forward for the FEM. As the attractive force is about 10 times greater than the tangential force due to rotation, hence the dimensions with a greater depth (0.373 m) are modelled in the FEM. This value is expected to be greater than what it will actually require.

Table 5.2: Analytical results of five possible spider-wheel beams arrangements with the attractive force applied.

Number of beams, n	5	10	25	50	100
Maximum attractive force on each beam, W (MN)	0.286	0.143	0.0571	0.0286	0.0143
Width, b (m)	0.588	0.309	0.126	0.0628	0.0314
Depth, d (m)	0.373	0.367	0.365	0.365	0.365
Total cross-sectional area of the beam, $b \times d \times n$ (m^2)	1.096	1.13	1.15	1.15	1.15
Maximum deflection, y_{max} (mm)	0.415	0.415	0.415	0.415	0.415
Normal stress, $Stress_{max}$ (kN/m^2)	61.7	61.6	61.2	61.6	61.6

Table 5.3: Analytical results of five possible spider-wheel beams arrangements with the rotational torque applied.

Number of beams, n	5	10	25	50	100
Maximum attractive force on each beam, W (MN)	0.036	0.018	0.0072	0.0036	0.0018
Width, b (m)	0.588	0.309	0.126	0.0628	0.0314
Depth, d (m)	0.004	0.011	0.065	0.26	N/A
Total cross-sectional area of the beam, $b \times d \times n$ (m^2)	0.0094	0.0346	0.205	0.816	N/A
Maximum deflection, y_{max} (mm)	2	2.5	2.5	2.5	N/A
Normal stress, $Stress_{max}$ (MN/m^2)	1.65	1.96	2.16	2.2	N/A

5.3.3 Validation of the spider wheel design with the FEM

An individual beam is modelled in the FEM to validate the Roark's formula calculations for the beam dimensions. The numerical results are shown in Table 5.4, Figure 5.9 and Figure 5.10.

Table 5.4: Dimensions of the spider wheel spoke with an applied attractive force and the dimensions of beam with torque.

	Number of spider-wheel beam	Maximum deflection (mm)	Length, *l* (m)	Width, *b* (m)	Depth, *d* (m)
Attractive force	5	0.415	1.325	0.588	0.373
Torque force	5	2	1.325	0.588	0.004

The FEM result in Figure 5.9 shows that the maximum deflection of the beam by the attractive force is 0.457 mm, 10% difference from the analytical result. Figure 5.10 shows that the maximum deformation by torque is about 2.685 mm, which is a significant 34% deviation from the analytical results.

So far the deflection simulations only consider when both forces are applied separately. Whether the beam can withstand both forces is investigated in the FEM and the result is shown in Figure 5.11. The maximum deflection in this scenario is 0.452 mm. There is a slight decrease in the maximum deflection value. This may be due to the cancellation of the force applied in different directions. This simulation result shows that a single beam with the dimensions of the one shown in Figure 5.9 can withstand both the forces.

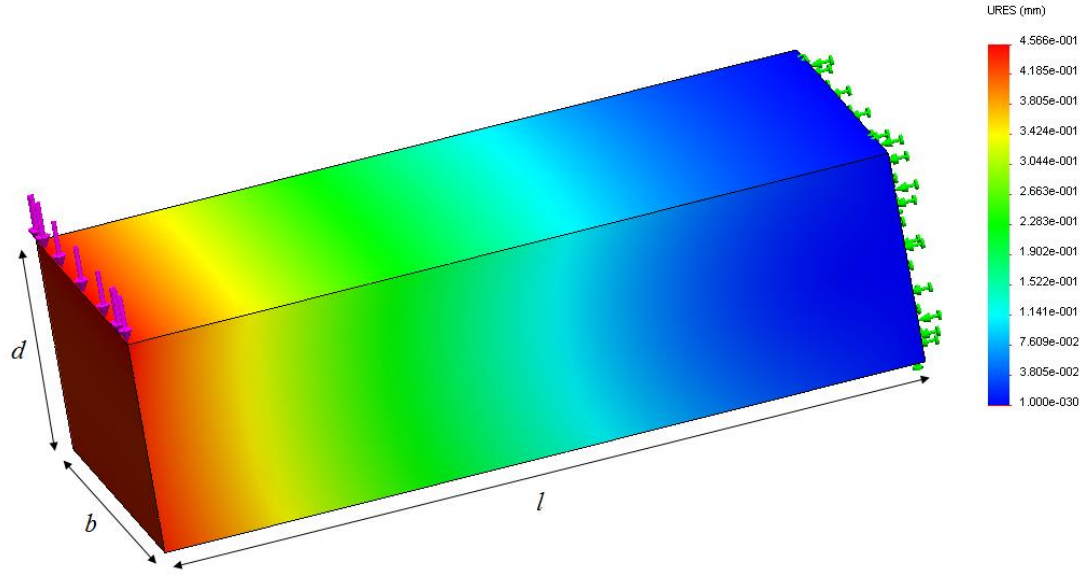


Figure 5.9: Finite element simulation of spider-wheel beam with attractive force applied on the edge of the beam (b=0.588m, d=0.373m and l=1.325m).

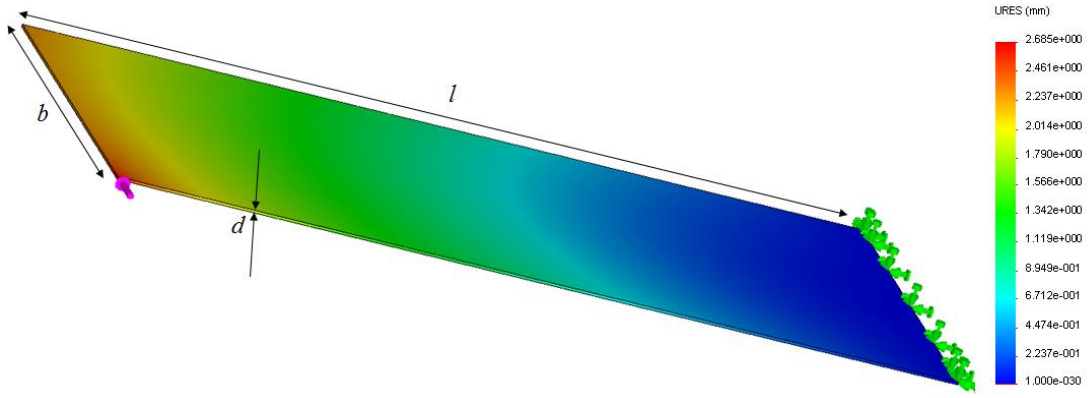


Figure 5.10: Finite-element simulation of spider-wheel beam with torque applied on the edge of the beam (b=0.588m, d=0.004m and l=1.325m).

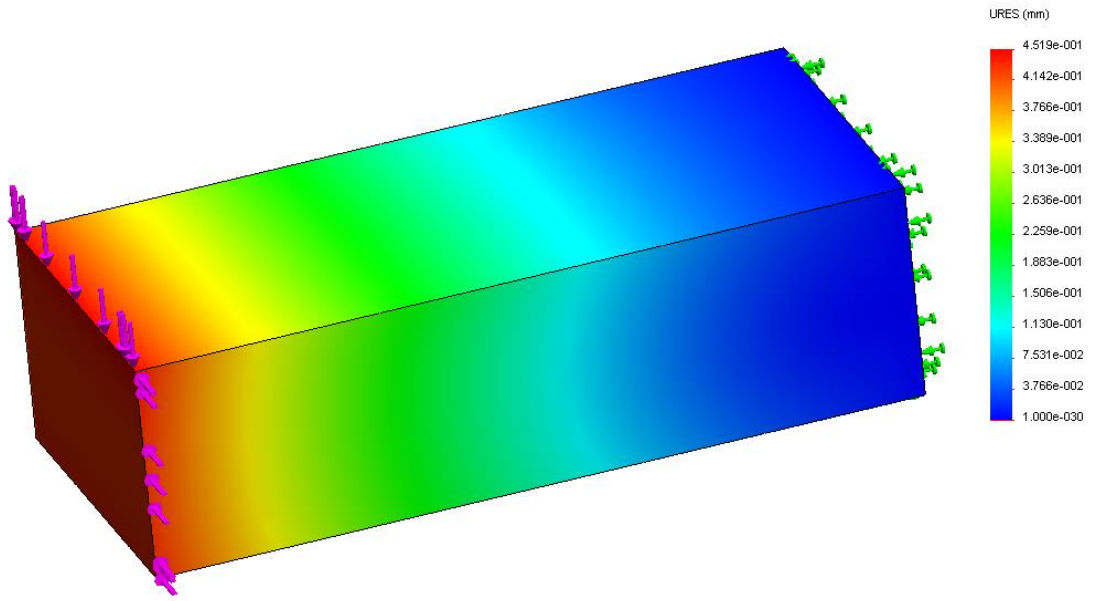


Figure 5.11: Finite element simulation of a spider-wheel beam with both attractive force and torque applied on the edge of the beam (b=0.588m, d=0.373m and l=1.325m).

After determining the number of spokes and their dimensions, a full 5-spoke spider wheel is modelled in the FEM (Figure 5.12). However, the spider wheel structure has weakened the stiffness of the rotor plate and caused a deflection of 0.724 mm on the outer part of the wheel. This is beyond the 10% deflection limit (0.5 mm). At the same time, this design still has a total weight of 62.316 tons, which is only 19.3% lighter than the simple rotor plates.

In this case, there are two possible means to strengthen the rotor plate. The first one is to increase the thickness of the whole plate from 0.373 m to 0.425 m. This will increase the total weight to 71 tons. The second approach is not to increase outer plate thickness where the permanent magnets are attached but only increase the thickness of the beams. To reinforce the outer area of the rotor where the

permanent magnets are attached, the beams are then extended to the back of the permanent magnets (Figure 5.14). The thickness of the plate remains unchanged (0.2887 m) while the thickness of the beams increased to 0.4587 m. The total weight of the two rotor plates is 64.37 tons, 16.66% lighter than the simplified rotor plate design, still far from the 50% target.

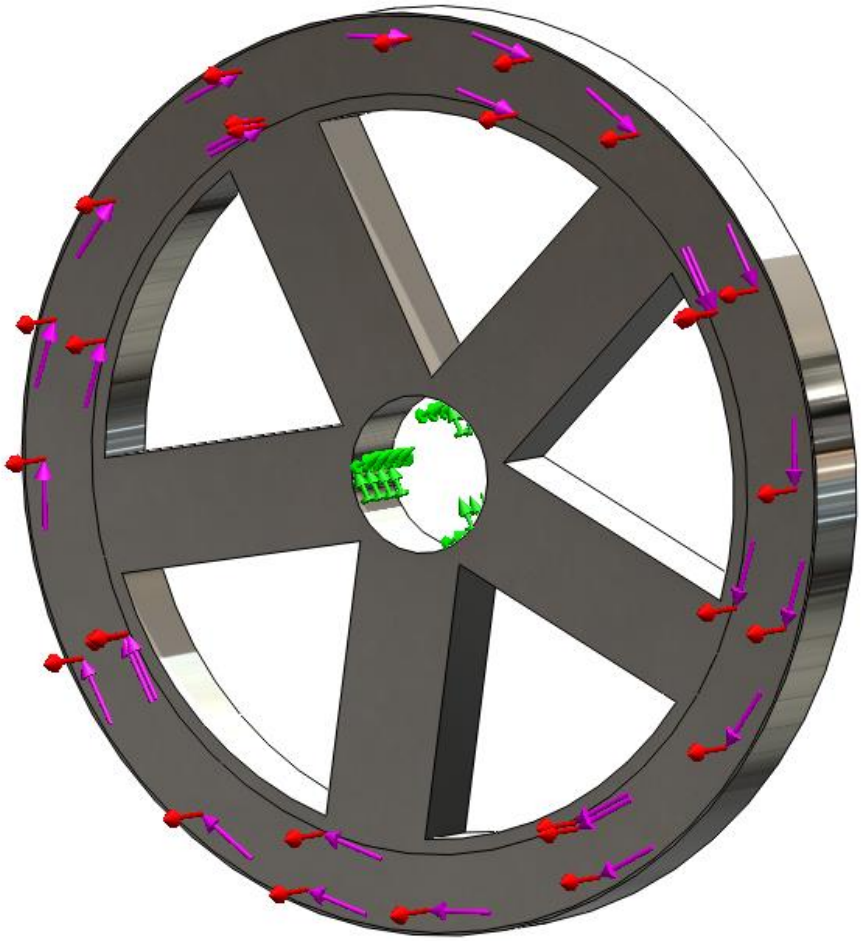


Figure 5.12: A single 5-beams spider-wheel rotor plate.

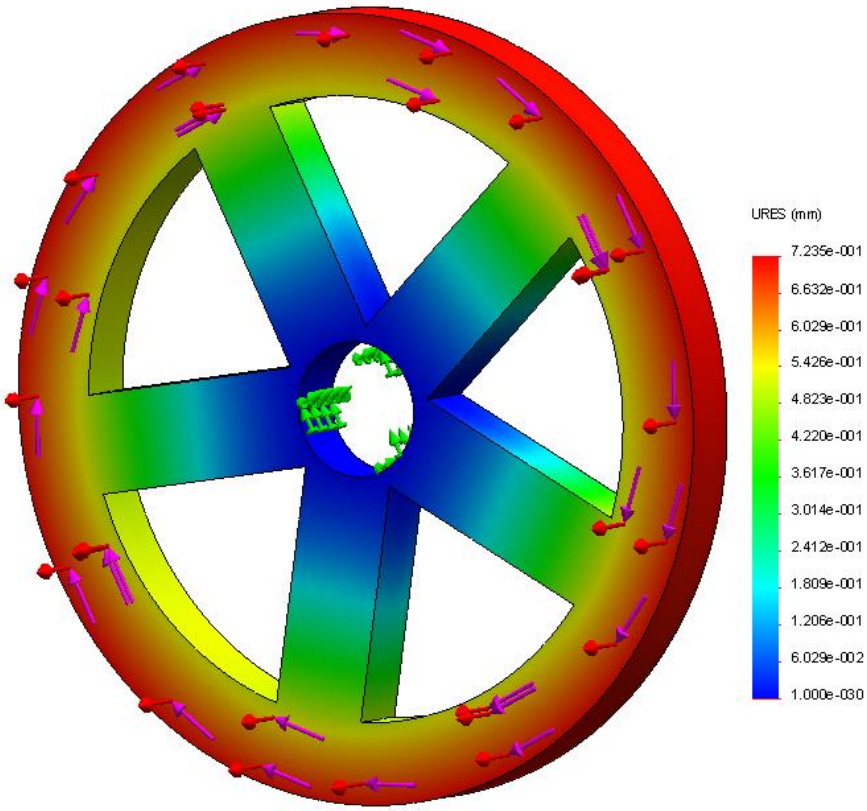


Figure 5.13: Deflection results of the 5-spoke spider wheel rotor plate design of which the thickness is 0.373 m.

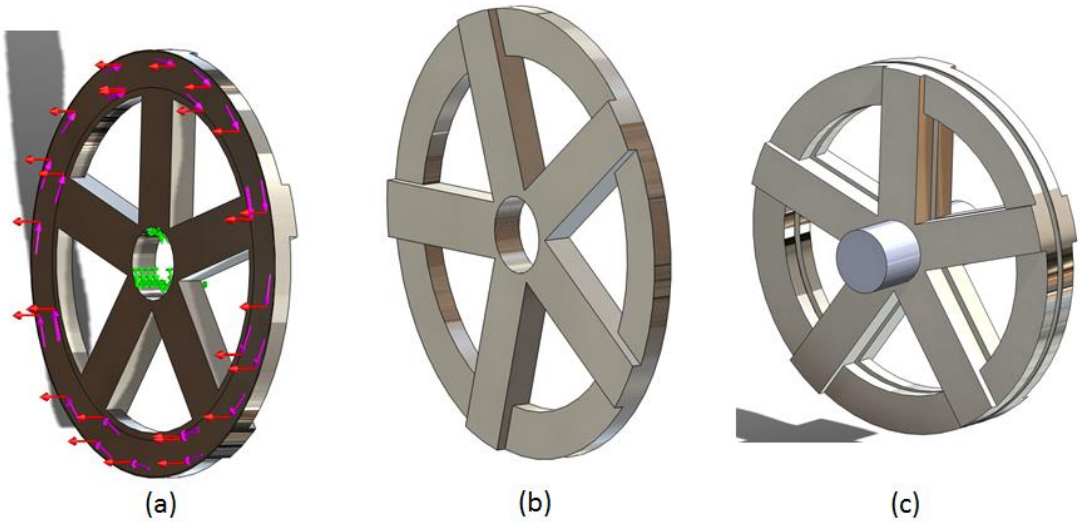


Figure 5.14: Strengthening the 5-spoke spider wheel rotor by increasing the thickness of the spokes; (a) The rotor plate front view where permanent magnets are attached to; (b) a back view of the rotor plate and the spokes are extended to the back; (c) a view of both rotor plates with extended spokes.

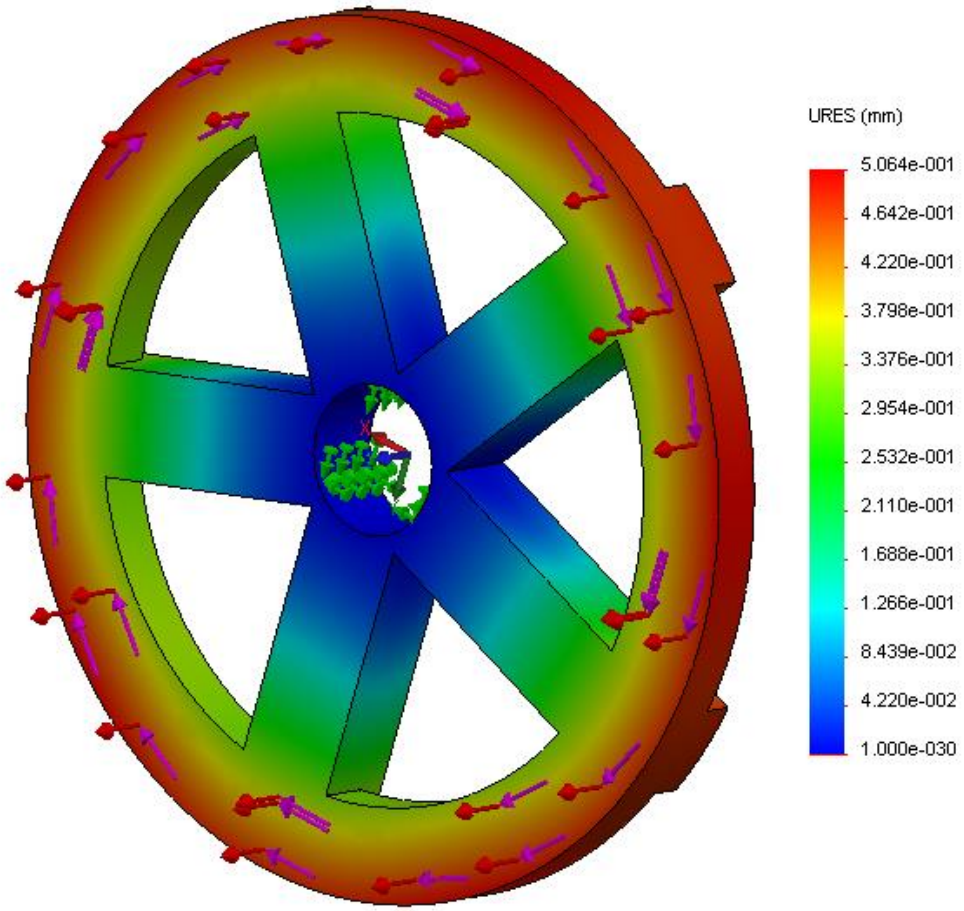


Figure 5.15: Deflection contour of the rotor plate after increasing the thickness of the spokes.

5.4 Rotor plates design with a support ring

A support ring is then considered to further strengthen the structure of the rotor plate (Figure 5.16), especially the outer area. The support ring can structurally connect both rotor plates together to reduce deflection. Although fixing the support ring onto the outer circumference of the rotor plate is more effective to hold the rotor plates together, but the edge of the rotors has to remain clear to give

access to the stator and to install a cooling system. Therefore, it can only be fixed to the inner circumference.

The distance between the two rotor plates is the total thickness of the permanent magnets, the air gap and the stator cores, which is 0.1038 m. An extra 0.05 m is reserved for the gap between the support ring and the permanent magnets to accommodate a cooling path.

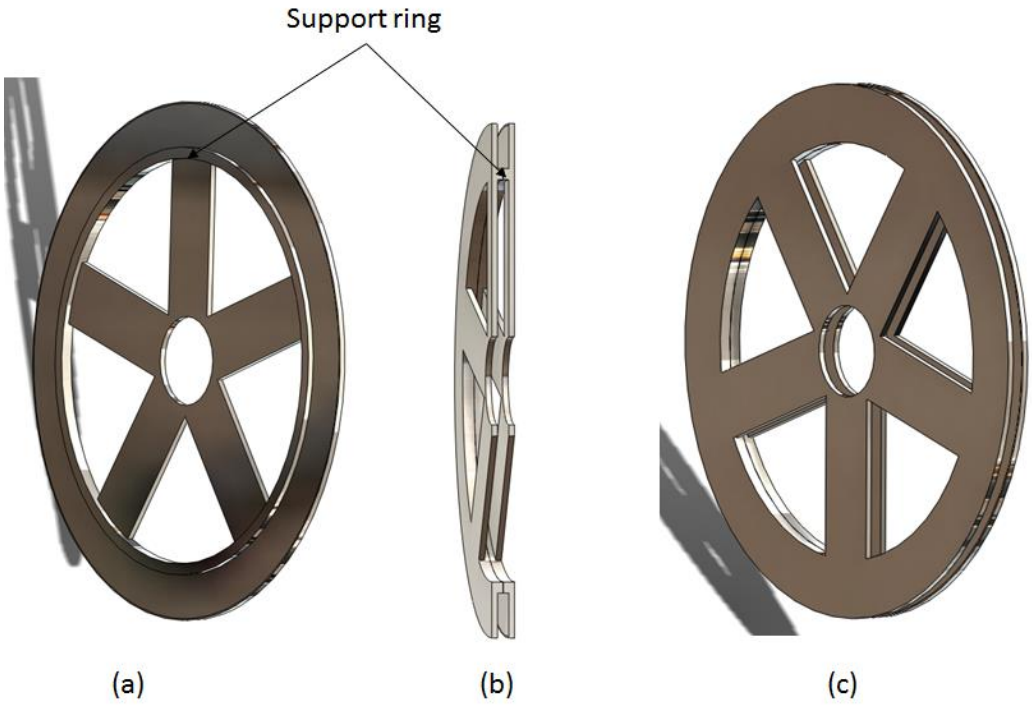


Figure 5.16: Rotor plate design with inner support ring.

By adding a support ring, the required thickness of the outer area of each rotor plate is reduced to 0.0625 m and the extension of the spoke is not required (Figure 5.16). The total weight of the two rotors is reduced to 23.94 tons, which is 69% lighter than the original design. The simulated deflection effect is shown in

Figure 5.17. The maximum rotor deflection is 0.49 mm, just below the 0.5 mm allowance. To avoid stress concentration, fillets can be installed between the spokes and the ring during the manufacturing process.

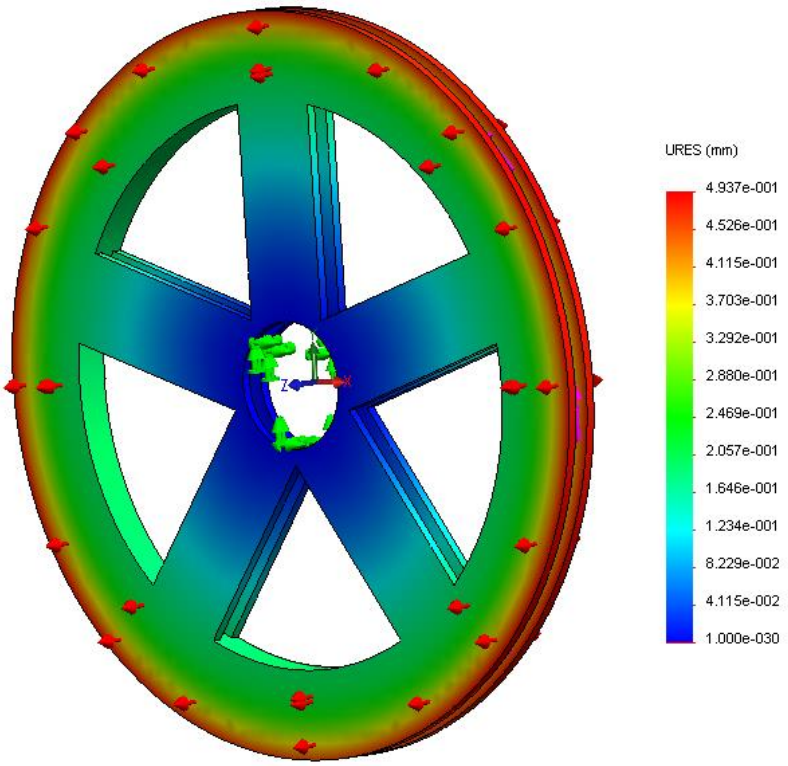


Figure 5.17: Deflection solution of the rotor plate design with inner support ring.

5.5 Structure design of the stator

A YASA machine does not have stator yokes to hold the stator cores. Instead, a whole piece of glass reinforced plastic is shaped to a disc with slots, to which the stator cores are bonded (Figure 5.18). Apart from being lightweight, glass reinforced plastic does not conduct magnetic flux, and therefore, the losses of magnetic flux are lower than a stator using steel yokes. Two steel rings are used

at the inner and outer circumferences to seal the stator. Bearings are installed at the inner ring, which move around the support rings of the rotors. On the outer ring, the inlets and outlets for the cooling system are installed so that pipes can be connected to inject coolants into the stator teeth. The outer ring will also be attached to a housing to fix the stator in place.

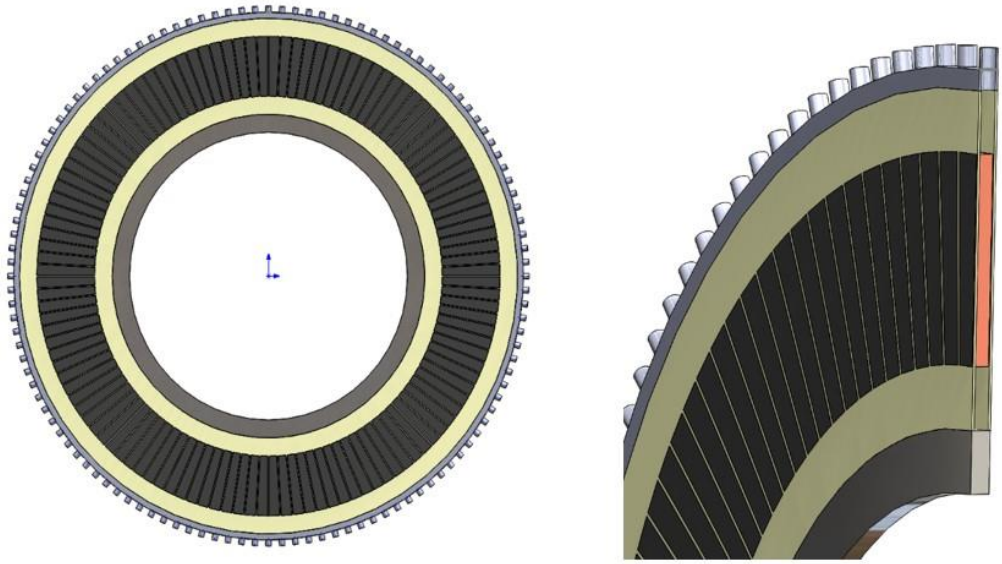


Figure 5.18: Illustration of the stator structure design. Bearings are not shown in the figure.

The stator of a YASA machine is positioned in the midway between the two rotors. Ideally, the two opposite and same magnetic attractive forces acting on the stator should cancel out. In reality, small deviation of the position of the stator is inevitable and will result in some magnetic attractive force acting on the stator, causing the stator to deflect. A study is performed here to determine how significant this imbalanced attractive force can affect the structure of the stator if it shifts by 2% from the centre during operation. In practice, this small shift could

either be caused by manufacturing error or wear and tear of a rotor. In the current geometry, this 2% deviation means that the air gap of the stator and one rotor is 4.9 mm and of another rotor is 5 mm.

Using equation (3.29), the attractive force of 4.9 mm air gap is 1.64 MN and the attractive force of 5 mm air gap is 1.60 MN. This results in a force of 0.04 MN acting on the stator. The boundary conditions set in the simulation of the stator are: 1) the outer ring is fixed; 2) inner ring is set as a roller; and 3) the imbalance forces are applied on the surface of the stator shoes. The simulation result (Figure 5.19) shows that the stator deflection is 0.126 mm at 0.04 MN which is only 2.52% of the air gap. The deflection is quite small in regard to the deflection limit set to the rotor.

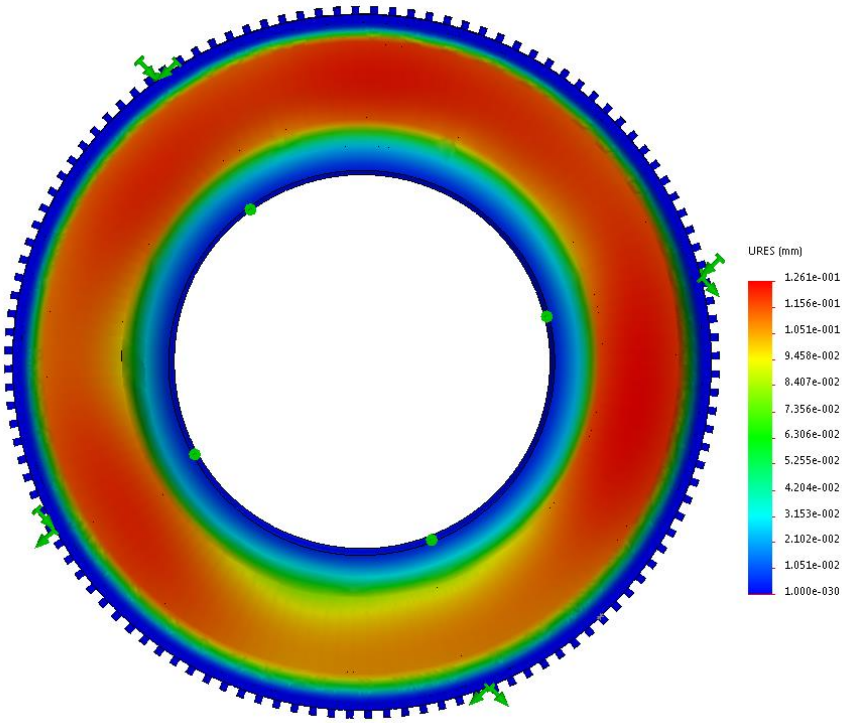


Figure 5.19: Deflection result of the 1MW YASA stator.

5.6 Proposed assembly method

Assembling a large-scale axial flux machine is challenging. When assembling the stators and the rotors, the attractive force between the permanent magnets and the iron cores can react when they are meters apart. The two parts are brought together axially to an only 5 mm gap, at which point the attractive force is 1.43 MN. It is also essential to maintain the rotor and the stator as parallel as possible. Variation in air gap length can have significant influence on the machine efficiency, and the worst case, the rotor may crash into the stator causing catastrophic damage. Considering these issues, the assembly of the YASA machine structure is proposed and a schematic is shown in Figure 5.20.

First, the stator is fixed to a housing and the shaft is positioned in the centre both perpendicularly and horizontally. Jacking screws should be in place at this point. The jacking screws for two rotor plates need to be threaded in opposite directions. The jacking screws help the rotors approach the stator slowly and prevent the rotor from crashing into place. Both rotor plates should approach to the centre slowly using the jacking screw at the same time and speed. This is to ensure that the two opposite magnetic force applied on the stator is always balanced so that it does not cause defection. The rotor plates are followed by retainers that hold the plates up straight. The rotors are jacked in until the support

rings on both plates are in contact. The two rotor plates are screwed together and the retainers and jacking screws are removed.

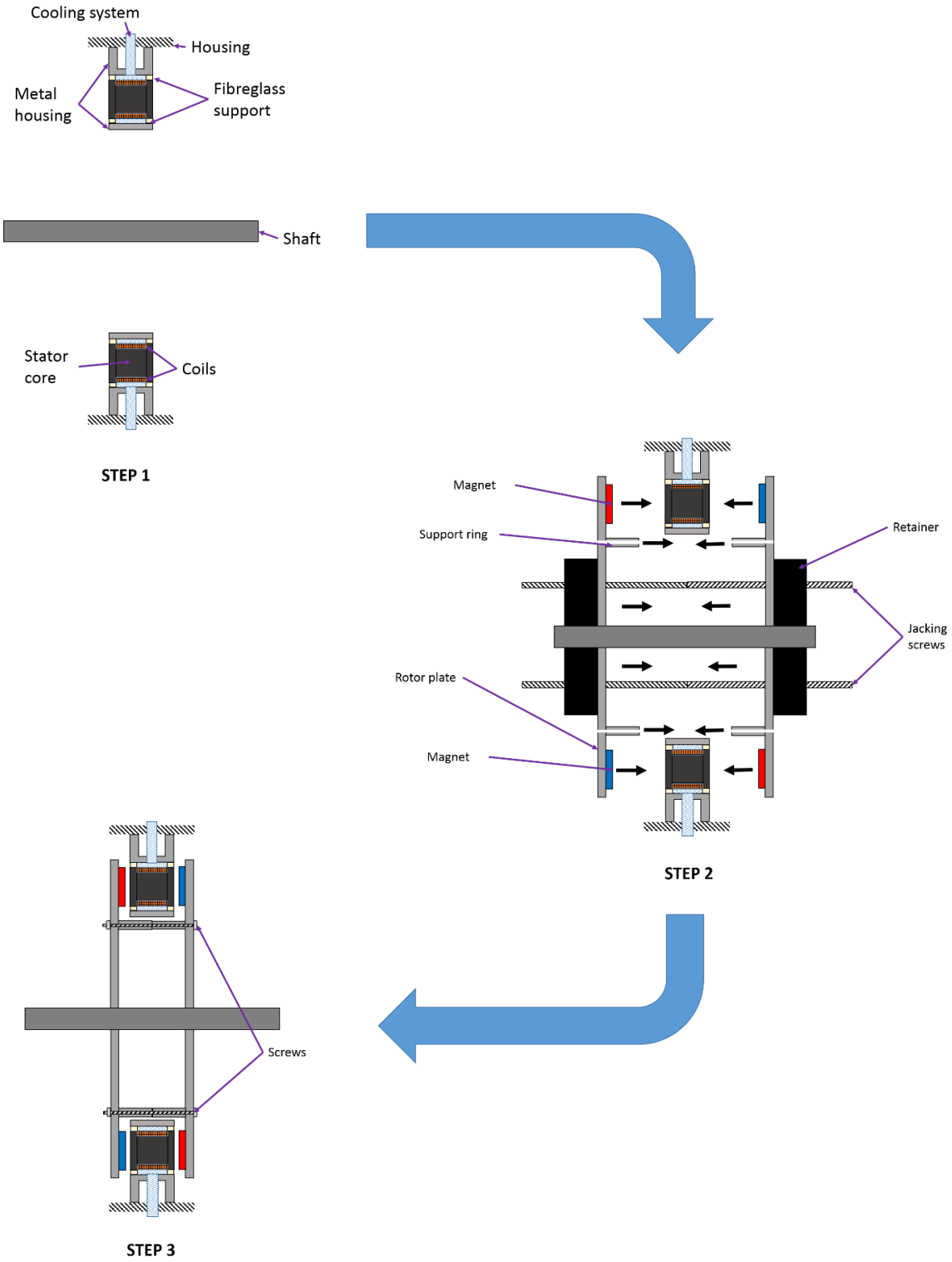


Figure 5.20. A proposed assembling method for the stator and the rotors.

5.7 Summary

To reduce the weight of the rotor plate without the deflection exceeding the design allowance, a spider wheel structure is considered where the number of spokes, spoke dimensions and plate thickness are analysed with the Roark's formula. These parameters are further refined using the FEM. A support ring is added between two plates to further improve the structural integrity. The optimised rotor plate is about 69% lighter than a simple flat plate and the maximum deflection is below 0.5 mm. A method to assemble the rotors and the stator is proposed.

Chapter 6 – Thermal Design

This chapter focuses on the thermal design for a MW-scale YASA generator. The major heat source of a generator is from the copper windings on the stator. Overheating of a machine can lead to irreversible failure of some machine components. First, demagnetisation will occur once the Curie temperature of the NdFeB permanent magnets (maximum 230°C) (NdFeB_info.com 2014) is reached. Second, the insulation of the copper windings will decompose quickly if the temperature is beyond the working temperatures. Although Class C insulation (e.g. polyimide) can have a maximum working temperature of 240°C (MWS Wire Industries 2014a), it is a relatively expensive insulation material. Class H (180°C) insulations are more commonly used. In addition, having no stator yoke to hold the stator core, the stator core of the YASA is made of glass reinforced plastic, the mechanical properties of which are temperature sensitive. Therefore, designing an effective cooling system is important to prolong the lifetime and to produce the best efficiency.

In general, a cooling system for an axial flux machine can have two major designs. They are the through-flow ventilated cooling system and the fully-enclosed cooling system. The through-flow ventilated cooling system is thermally

advantageous since it allows air to enter the air gap of the machine to cool both the rotor and stator rather than having the air recirculating inside the model in a fully enclosed cooling system.

Through-flow ventilated air cooling on an axial flux machine can be achieved by dragging air from the environment into the machine due to the pressure difference created from the rotation of the rotor plates (Howey 2010). This method is more suitable for a high-speed machine (R Camilleri et al. 2012). However, applying this method to a MW-scale YASA generator is challenging. Firstly, a direct drive machine has a low rotational speed and hence the amount of air flowing through the model may not be sufficient to transfer heat. Secondly, considering offshore applications, a fully enclosed system may be more suitable as it protects the generator from the harsh environment. In this case, a fully enclosed cooling system will be considered for the YASA generator.

In this study, this cooling design is aimed at reducing the operating temperatures of windings and stator cores to a Class F (155°C) rating and the winding insulation rating is assumed to be Class H (180°C). A typical thermal electrical design begins with an analytical approach by developing a lumped parameter thermal network. The advantage of this technique is 'fast' (Boglietti et al. 2009), but the accuracy is highly dependent upon the preciseness of the network and more importantly the heat transfer coefficients (HTCs) (Boglietti et al. 2009;

Zhang et al. 2011). Convection correlations are available to calculate the heat transfer coefficient of simple geometries. For a complex geometry, the calculation of the HTC using empirical convection correlation is difficult. In this case, the computational fluid dynamics (CFD) is used to predict the HTC. The HTC of the cooling duct designed for a MW-scale YASA generator was analysed using the convection correlations and the CFD with Solidworks Flow Simulation. As the main heat source is the stator windings and stator cores, only the heat transfer properties of the stator will be investigated.

6.1 Forced air cooling system

In a MW-scale YASA generator, heat is generated in the stator windings and needs to be conducted through layers of insulation materials, which have low thermal conductivity. To enable an effective convective heat transfer, air should be in direct contact with the windings by flowing through the small channels between the stator cores after passing through a reservoir, where the cool air can be in contact with the end windings (Figure 6.1). The air is then forced through a neighbouring stator channel, entering another reservoir before exiting the housing. This cooling design allows air to flow through the gap between the stator cores only twice. Only a 1/60 section of a full 1 MW YASA model is studied for simplification considering the rest is symmetrical. A divider is used to separate the inlet and outlet reservoir, preventing the air from bypassing the narrow passages.

Both inlet and outlet are installed on the outer ring but not on the inner ring, which is reserved for the structural purposes. The dimensions of the coolant pathway are shown in Table 6.1.

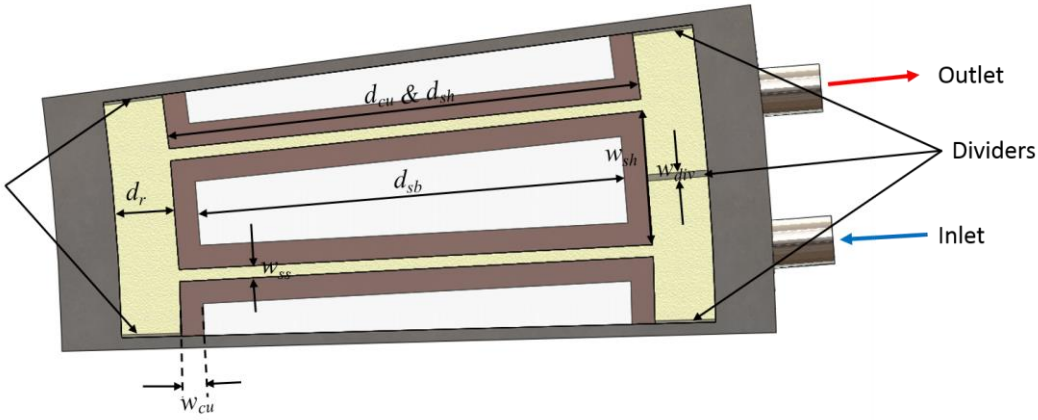


Figure 6.1: 1/60 sectioned stator cooling system of the 1 MW YASA generator.

Table 6.1: The dimensions of the cooling design of the 1 MW YASA generator.

Parameter	Symbol	Values
Depth of stator shoes & depth of coil	d_{sh} & d_{cu}	395 mm
Diameter of inlet and outlet	d_{in} & d_{out}	30 mm
Width of stator slot	w_{ss}	10 mm
Width of copper winding	w_{cu}	19.2 mm
Length of stator bar & length of coil	l_{sb} & l_{cu}	30.2 mm
Width of stator shoe	w_{sh}	111 mm
Length of stator shoe	l_{sh}	7.5 mm
Depth of the stator bar	d_{sb}	356.6 mm
Width of the divider	w_{div}	5 mm
Depth of the reservoir	d_r	50 mm

6.2 Computational fluid dynamics (CFD) simulation

In this section, the computational fluid dynamics (CFD) method is used to simulate the heat transfer of the forced air cool YASA generator. The dimensions of the 1 MW YASA generator that is obtained from the optimisation in Chapter 3 is modelled in the Solidworks Flow Simulation package. The dimensions of the 1 MW YASA generator is shown in Table 6.1.

6.2.1 Boundary conditions and meshing

After creating a cooling system model of the YASA generator in the CFD software, boundary conditions, materials of the components, heat sources and radiation are set. The boundary conditions on the cooling system model are the inlet mass flow rate and the outlet's environment pressure (0.1 MPa) at 40°C. The turbulence parameters setting is: Turbulence intensity is 2% and the turbulence length is 0.47mm. The materials are copper for the windings, glass reinforced plastic for the stator supports, plain carbon steel for the outer case and electrical steel for the stator cores. The heat generated by the two copper windings is 908.5 W and by the two stator cores is 24.4 W based on the power losses calculation in Chapter 3. The surface of the stator plates, and the outer frame which are facing the outer atmosphere is assumed to have white wall radiation and the surface of the stator shoes facing to the atmosphere is assumed to have black body radiation. Although the only 1/60 of the stator is modelled and undergo the flow simulation, the simulation requires a considerable amount of computer RAM to perform the

meshing and calculation. Due to the limitation of RAM of the computer used, the mesh size cannot fully go through mesh independences. The smallest mesh size can be used to simulate the model is 5.33 mm. The number of fluid cells generated is 11180, solid cells is 27584 and partial cells is 33865.

6.2.2 Determination of inlet mass flow rate

As turbulent flow is more effective at transferring heat, the minimum mass flow rate to allow turbulent flow through a duct is estimated when the Reynold's number Re>2300,

$$\dot{m} = \frac{Re \cdot v \cdot A_{cp} \cdot \rho}{D_H} \tag{6.1}$$

where v is the kinematic viscosity of the cooling fluid, ρ is the density of the air and A_{cp} is the cross-sectional area of the channel between two stator cores. The D_H is the hydraulic diameter of the channel,

$$D_H = \frac{4A_{cp}}{P} \tag{6.2}$$

where P is the wetted perimeter which is equal to the total outer length of the narrow channel. The channel can be seen as a rectangular duct, and the hydraulic diameter is,

$$D_H = \frac{2ab}{a+b} \tag{6.3}$$

Using the air properties at 140°C, a minimum 1 g/s inlet mass flow rate is required to achieve turbulent flow of the air in the duct. Steady-state CFD analysis was then used to investigate how the stator temperature is influenced by the air flow rate. Figure 6.2 shows that with increasing air flow rate, the steady-state stator temperature decreases and saturates at around 80°C. With a mass flow rate above 11 g/s, the stator can achieve a steady-state temperature below 150°C, within the Class F design limit. To investigate whether this cooling system can allow a higher power losses, such that the applied current density can be increased, the heat generated by the two stator coils is increased by twice to 1817 W. The maximum stator temperature as a function of the mass flow rate is shown in the orange curve in Figure 6.2(a). In this case, 30 g/s mass flow rate of air is required to achieve the 150°C steady-state temperature.

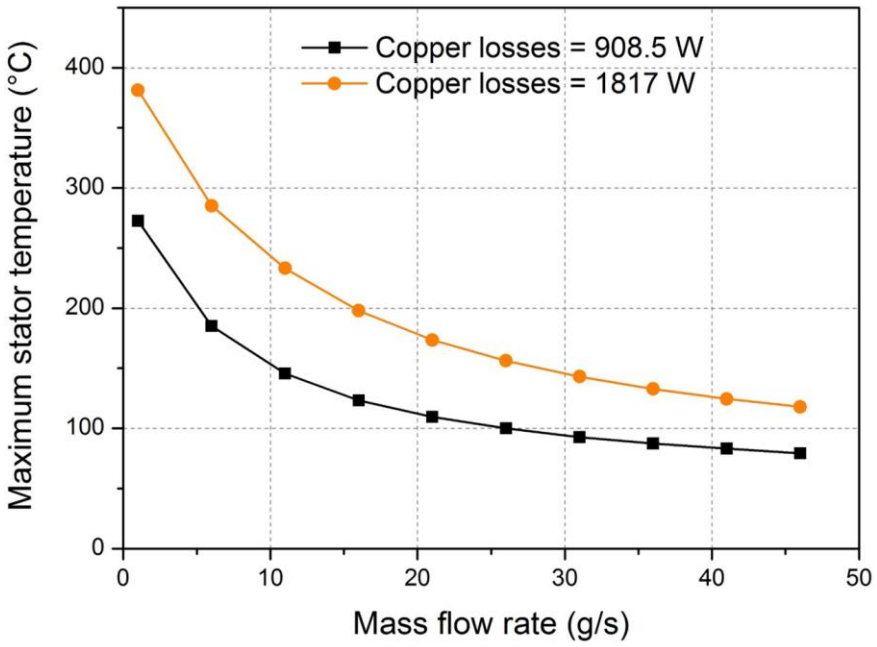
Table 6.2: Air properties (The Engineering Toolbox 2014a).

Density at 140°C, ρ_{air}	0.854 kg/m^3
Dynamic Viscosity at 140°C, μ	2.0×10^{-5} Pa.s
Specific Heat Capacity at 140°C, *Cp*	1013 J/kg.K
Thermal Conductivity at 140°C, *k*	0.0343 W/mK

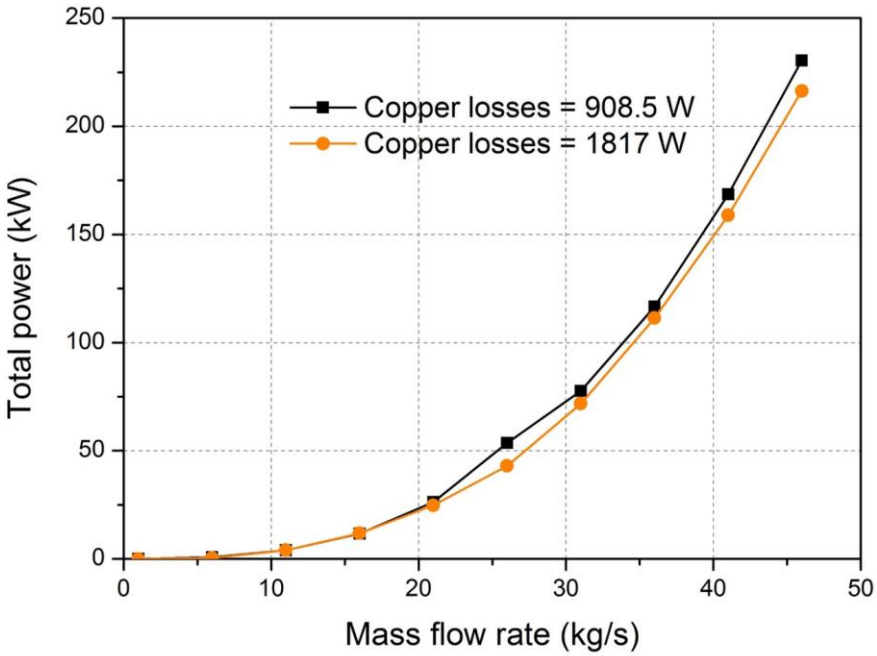
Even though the machine can be cooled below the design limit using forced air, the feasibility of this cooling system must be considered in conjunction with the power required to achieve the mass flow rate. In this case, a full machine model

that has sixty of the above cooling section is considered. Assuming all 60 sections have exactly the same power output and thermal behaviours, to cool the stators below 155°C will require a total of 660 g of air flowing through the machine per second. The pressure drop across the cooling path is shown in Figure 6.3. The largest pressure drop occurs at the entrance into the cooling channel by around 800 Pa. A pressure drop of 500 Pa occurs when the air pass through each channel. This drop is likely caused by the friction of the surface. The simulation assumed the winding has a smooth surface. In reality, this is not the case, and the friction loss will be much higher. The total power required to drive the air through the system can be determined by multiplying the volume flow rate of air with the pressure drop from the inlet to outlet times 60.

The required power for each mass flow rate is shown in Figure 6.2(b). At copper losses of 908.5 W, a total of 4053 W of power is required to pump the air through the whole machine at 660 g/s by a compressor. This has yet to consider any losses of the compressor itself. For a 1 MW YASA generator, this is equivalent to 0.4% of generated power. When the copper losses increase to 1817 W or the current loading increases to 8.5 MA/m^2, the cooling system will account for at least 7% of the generated power by a 1 MW YASA generator in order to cool the machine below 155°C.



(a)



(b)

Figure 6.2: (a) the relationship between the maximum stator temperature and the air mass flow rate; (b) the power required to achieve the mass flow rate for each 1/60 section.

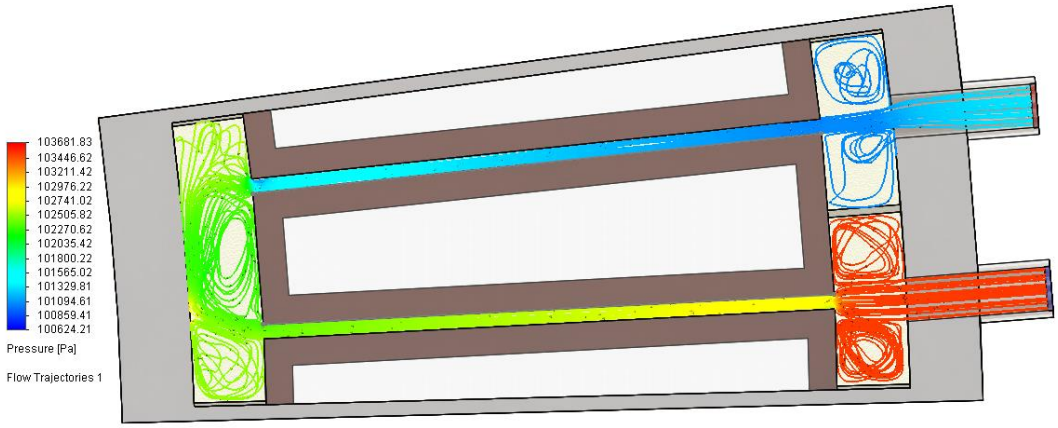
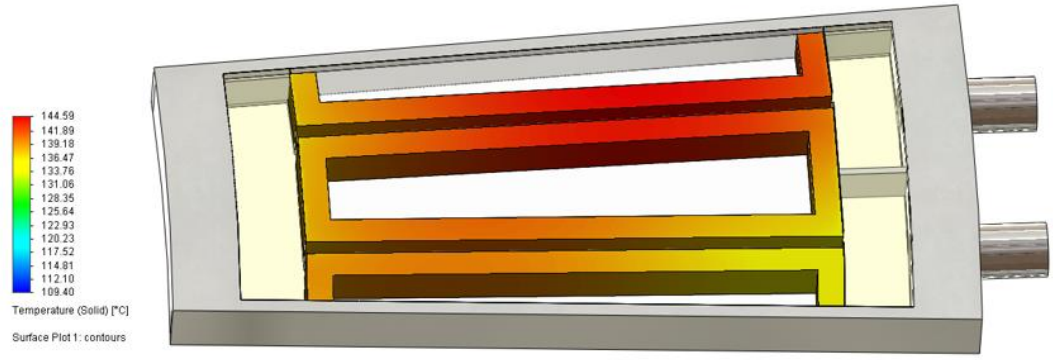


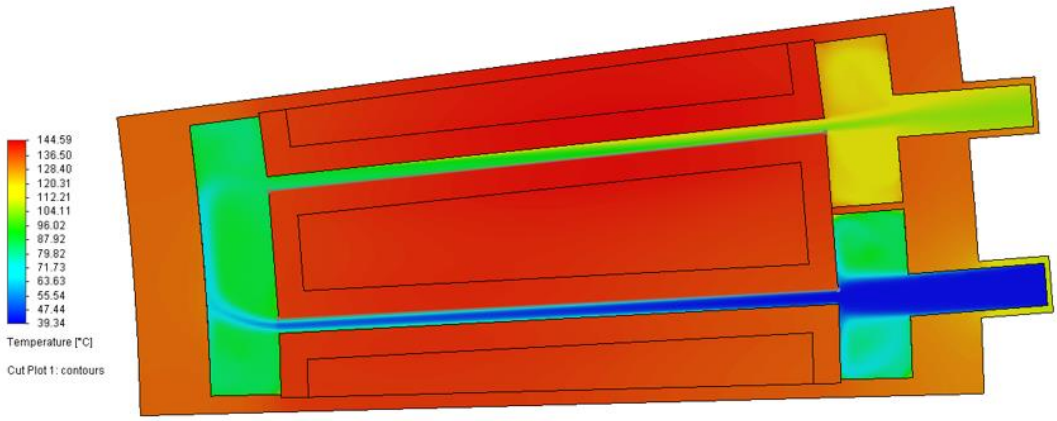
Figure 6.3: Simulated pressure across the model.

Figure 6.4(a) shows the surface temperature profile of the model at 11 g/s mass flow rate from the CFD simulation. The surface of the stator windings has a maximum temperature of 144.59°C, same as the bulk temperature of the stator (Figure 6.4(b)) as copper is a good thermal conductor. It is obvious that the windings around the second channel has a higher temperature than the first channel, with a small temperature difference around 5°C. This is due to the increased air temperature shown in Figure 6.4 (b). The air temperature increases to 50°C before exiting the first channel and reaches 120°C after pass through the second channel before exiting from the outlet. When the temperature of air increases, the volume of air expands dramatically and this form a high speed jet. The air velocity along the cooling path is showed in Figure 6.5. The jet stream was not observed in first cooling channel and the air speed is generally stable at 35 m/s. In the second channel, the jetting behaviour can be observed with the air velocity reaches as high as 50 m/s. The high air speed enables an effective convective heat

transfer in the channel. However, the air velocity near the end windings is low especially in the reservoirs near the inlet and the outlet. This may cause some cooling blind spots. Practically, it is possible to swap the inlet and outlet swiftly by switching the direction of the air compressor. This will help redistribute the temperature within the machine to achieve a homogenous cooling effect.



(a)



(b)

Figure 6.4: (a) surface temperature of the stator windings; (b) bulk temperature obtained by cutting through the centre of the model.

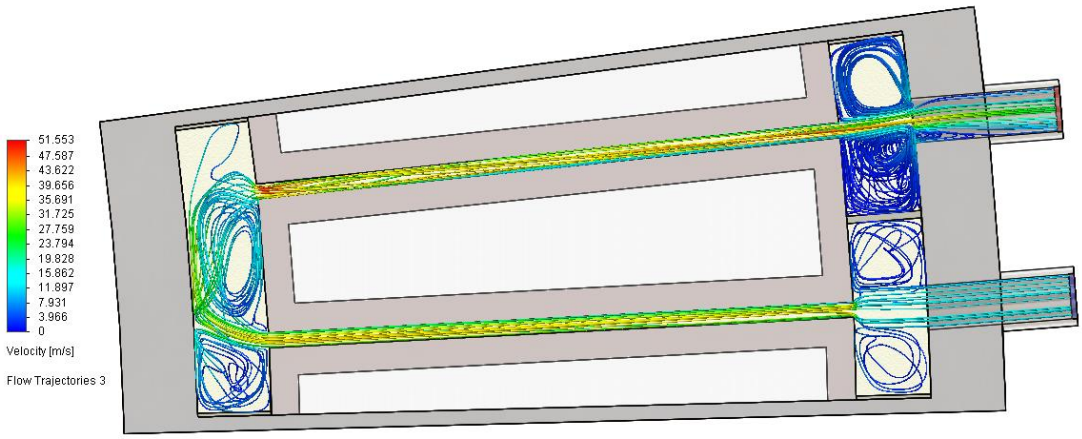


Figure 6.5: contour of air velocity along the cooling duct.

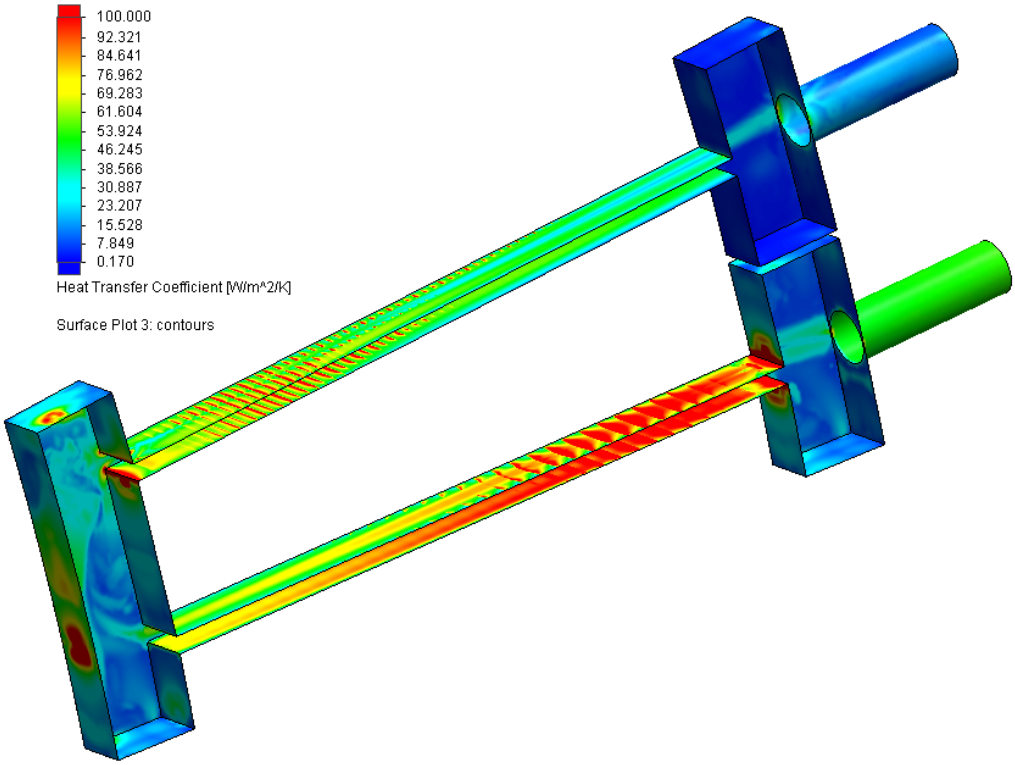


Figure 6.6: Heat transfer coefficient of the model surface.

The CFD simulation also calculates the heat transfer coefficients (HTC) at the stator core surface. The equation used in the Solidworks Flow Simulation software to calculate this HTC value is (Solidworks 2012),

$$h = \frac{Q_{convection}}{\mathrm{A}(T_s - T_f)} \tag{6.4}$$

where $Q_{convection}$ is the heat transfer rate of convection, A is the surface area, T_s is the temperature of surface and T_f is the temperature of surrounding fluid. The HTC contour is shown in Figure 6.6 and the HTCs shows some large fluctuations near the entrance of the channels. This is due to a rapid transition of the air temperature and velocity when air enters from the reservoirs to the narrow channels. However, the fluctuation stabilises as the air temperature and flow start to settle. The contour also shows that the HTC near the end winding is low, particularly in the reservoir near the outlet. This is consistent with the air velocity in those areas.

6.3 Summary

The chapter presents an effective forced air cooling system for a MW-scale YASA generator. The stator windings can be effectively cooled below 150°C at 660 g/s air mass flow rate using only 0.4% of the rated power. Using computational fluid dynamics, the air flow behaviour along the cooling path is characterised and some thermal hot spots around the end windings are identified. Further

optimisation is needed to address these issues. The heat transfer coefficient on the stator surface is characterised and is strongly dependent upon the air flow properties.

Chapter 7 – Conclusions and Further Work

7.1 Conclusions

The key research question of this thesis is how to develop and evaluate a design methodology for large-scale machines. Traditionally, a small or medium scale machine is designed iteratively using FEM as it can generate higher accuracy results that replicate closely to real machines. In the current design of the MW-scale YASA generator, the ratio of the diameter to the air gap length is 930, while the ratio of the existing 50 kW YASA prototype is just above 210. Using just FEM to design large-scale machines is therefore extremely challenging as the ratio of the largest to the smallest feature is high, leading to long processing times. In this case, an alternative technique that is independent of scale is needed for designing large-scale machines.

Performing analytical design calculations is independent of scale. Therefore, to design large-scale machines, it is more efficient to determine a design space using an analytical method leading to a design reference map. This can visualise the results and relationship between each objective function and also see compromises made in machine design. In addition, the optimisation tool with the Pseudo-weight vector approach adapted can further reduce the possible design

models to one, and therefore the workload for FEM simulation is significantly reduced. However, there are weaknesses of the analytical design tool: 1) the sensitivity study shows that the current density is sensitive to the leakage factor and the magnet concentration factor during the optimisation process that has higher weight ratio on the power losses. For example, the current density will change by 5% for every 1% change in the leakage factor and magnet concentration factor. As the values of the constants are based on assumptions or literature reports, strictly speaking, they should be considered as variables and optimised analytically or in the FEM. Although the constants are sensitive, the analytical calculated flux density is only 14% different from the one simulated with FEM; 2) Another concern of the current analytical tool is that the structure of the rotor plates is assumed to be two solid plates, which deviates significantly from the final structural design that is consist of a spider wheel structure and two support rings. The structural weight in the analytical tool is hence over-estimated; 3) the thermal design only considers the power losses but not the detail of the temperature rise in the analytical design tool, although it is difficult to derive the lumped parameter analysis model before knowing the full structure design of the YASA machine.

The role of the electromagnetic FEM to simulate a MW-scale machine is not to perform iterative design optimisation, but to validate the analytical calculations (flux density, back EMF and cogging torque) on one design. The electromagnetic FEM can also be used to perform minor adjustments of the dimensions and shape

of the machine components to improve efficiency. As these dimensions are directly related to the constants used in the sizing equations, by determining these constants will also resolve the sensitivity issue. The structural FEM in this thesis proposed a spider wheel structure with support ring, which reduced the weight by 60% from the solid rotor plate considered initially. A thorough structural design of a generator should investigate all machine components such as stator, housing, gears, bearings and shaft; especially how these components interact with each other. The CFD simulation of the cooling system has shown that forced air-cooling is capable of reducing the maximum temperature of the MW-scale YASA to Class H (180°C). There are few more aspects can be explored with the CFD 1) the use of other potential cooling materials, such as water or cooling liquid; 2) the channel size can be optimised and the issue of some blind spots in the reservoirs can be further studied.

A complete design practice should also include some analysis of the manufacturability and the practicality. The final design should be scrutinised by experts in relevant fields. Any modifications should be simulated in the FEM, after which a machine prototype can be produced and tested to conform to design standards.

7.2 Further work

Analytical design

To improve the analytical design tool in Chapter 3, the following work can be done:

Having learned from previous experiences, we are led to conclude that a rationalised design methodology for a MW-scale machine should have a design loop including both the analytical calculations and the finite element simulations (Figure 7.1). The design loop starts with a fast analytical calculation to produce the parameters of one machine design, followed by simulating the electromagnetic, structural and thermal properties of this design on the FEM. This thesis has essentially completed the first iteration of the design loop. The design outcome of this thesis should be feedback for the analytical design tool. This includes: 1) After trimming the dimensions and shape of the machine components on the electromagnetic FEM that related to the constant values in the sizing equations, the new constant values are adapted in the analytical design tool for the second design iteration; 2) the Roark's formula should now consider the spider wheel structure rather than the simple rotor plates to calculate plate thickness and weight by giving an allowed deflection limit. Equations need to be re-derived due to change in geometry. It is also worth considering using different materials to construct the spider wheel; 3) a cooling system is designed in the FEM in the previous iteration after knowing the machine structure. In the second iteration of analytical design, a lumped parameter analysis model can be produced based on this cooling system.

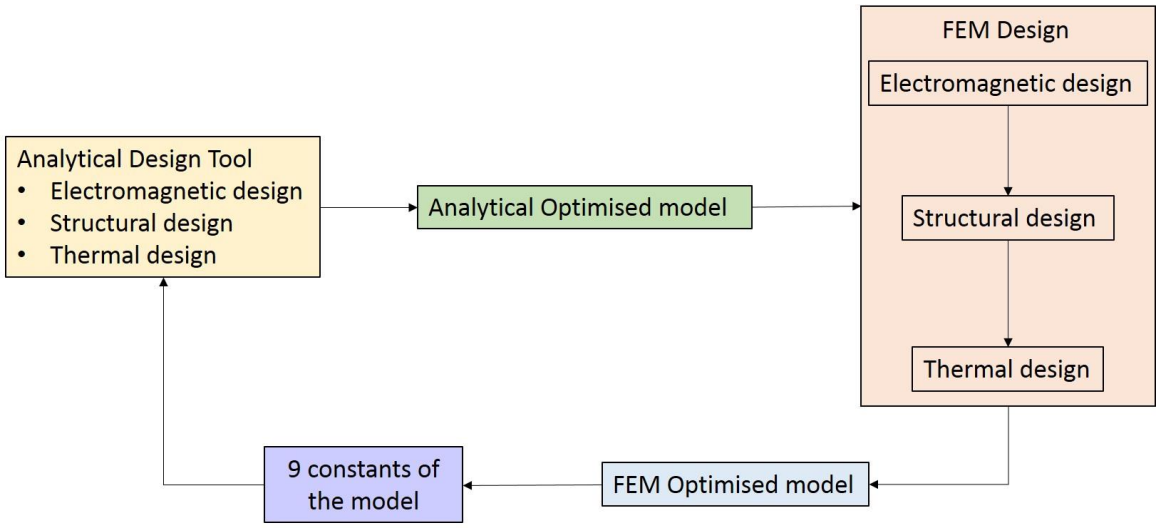


Figure 7.1: Proposed Design Loop for MW-scale generators.

Electromagnetic design with finite-element

1. Due to the limitation of the computer used to generate the megawatt - scale YASA model, limited data points were taken. To solve this problem, a latest version of Opera 3D which allows the simulation to be run with multiple CPU cores can be used.

2. In addition, if the problem raised above can be solved, a transient analysis of the megawatt-scale YASA generator can be simulated in order to have a clearer idea of the performance of the machine. This enables the simulation of the eddy current losses of the machine and a higher accuracy efficiency map to be generated.

3. The current 50 kW YASA prototype cannot fully validate the analytical and numerical methods to apply to the low speed megawatt-scale YASA machine.

An experiment with a large scale YASA machine is useful to fully validate the methodologies for the YASA design.

Structural design

1. The structural design of the stator as well as the bearing type and size to be used in the megawatt-scale YASA machine needs to be investigated. Further structural optimisation is expected in order to have a high power-to-weight ratio.

2. The structural design of the stator needs to be further investigated to improve the strength of the structure that not only can withstand the attractive force due to misalignment but also ensure that the structure can cope with the cooling system.

3. The other mechanical parts of the YASA machine, such as the shaft, housing and bearing need to be further investigated. The full structure design should be improved to conform to the manufacture and practical machine standard.

Thermal design

1. A thermochromic liquid crystal experiment will be performed to collect a mapping of the heat transfer coefficient in the YASA stator cooling system. This result can be used to validate the CFD methods. With the HTC data, a lumped parameter method can be applied to the YASA machine.

2. With the experimental results, the thermal correlation for the YASA cooling system can be defined and this can be used to derive the lumped parameter model. This model can then feed into the analytical design tool to complete the design loop.

Appendix I

In *Section 4.2.2.1* Roark's formula was introduced and used to calculate the rotor disc deflection. The equations in the plate constants (C) and the loading constants (L) of Roark's formula are given below.

$$C_2 = \frac{1}{4}\left[1-\left(\frac{b}{a}\right)^2\left(1+2\ln\frac{a}{b}\right)\right]$$

$$C_3 = \frac{b}{4a}\left\{\left[\left(\frac{b}{a}\right)^2+1\right]\ln\frac{a}{b}+\left(\frac{b}{a}\right)^2-1\right\}$$

$$C_5 = \frac{1}{2}\left[1-\left(\frac{b}{a}\right)^2\right]$$

$$C_6 = \frac{b}{4a}\left[\left(\frac{b}{a}\right)^2-1+2\ln\frac{a}{b}\right]$$

$$C_8 = \frac{1}{2}\left[1+\nu+(1-\nu)\left(\frac{b}{a}\right)^2\right]$$

$$C_9 = \frac{b}{a}\left\{\frac{1+\nu}{2}\ln\frac{a}{b}+\frac{1-\nu}{4}\left[1-\left(\frac{b}{a}\right)^2\right]\right\}$$

$$L_{11} = \frac{1}{64}\left\{1+4\left(\frac{r_0}{a}\right)^2-5\left(\frac{r_0}{a}\right)^4-4\left(\frac{r_0}{a}\right)^2\left[2+\left(\frac{r_0}{a}\right)^2\right]\ln\frac{a}{r_0}\right\}$$

$$L_{14} = \frac{1}{16}\left[1-\left(\frac{r_0}{a}\right)^4-4\left(\frac{r_0}{a}\right)^2\ln\frac{a}{r_0}\right]$$

Appendix II

In this appendix, the calculation process of the single layer fractional slot concentrated winding layout of the 1MW YASA machine with 50 number of pole pairs and 120 number of stator slots is discussed. The methodology used is presented by Hanselman (1994); Hendershot & Miller (1994) and Pyrhnen, Jokinen, & Hrabovcov (2008).

As this YASA machine design has a slots per pole per phase is equal to a fractional number which is shown in the calculation below,

$$q = \frac{Q}{2pm} = \frac{120}{2 \times 50 \times 3} = \frac{2}{5}$$

The conditions of symmetry that are needed to fulfil in order to create a first-grade fractional slot winding as stated by Pyrhnen, Jokinen, & Hrabovcov (2008) is listed below,

1) $\frac{p}{n} = \frac{50}{5} = 10 \in N$

2) $\frac{n}{3} = \frac{5}{3} \notin N$

3) $n = 5 \in N_{odd}$

Number of layers in the voltage phasor diagram t* = 1.

Number of pole pairs in the base winding p* = $\frac{p}{n} = \frac{50}{10} = 5$.

Number of slots of a base winding $Q^* = \frac{Q}{t}$.

Number of radii $Q' = \frac{Q^*}{t^*} = \frac{12}{1} = 12$.

Slot angle $\alpha_u = \frac{360° \times p^*}{Q^*} = \frac{360° \times 1}{12} = 30°$.

Number of phasors skipped in the numbering, $N_{ps} = \left(\frac{p^*}{t^*}\right) - 1 = \left(\frac{5}{1}\right) - 1 = 4$.

Since t*=1, Q'=Q*=12, therefore the phasors for each phase are $\frac{Q^*}{m} = \frac{12}{3} = 4$, which are then divided into negative Z- and positive Z+ phasors.

The number of phasors per phase in the first-grade base winding is $\frac{Q^*}{m} = \frac{Q}{mt} = \frac{120}{3 \times 10} = 4 \in N_{even}$.

As in this case there is no zone variation, the phasors are evenly divided into positive and negative phasors and therefore number of pahsors of both types is two, Z- = Z+ = 2.

By employing a normal zone order –u, +w, -v, +u, -w, +v, the voltage phasor diagram is divided into zones with two phasors in each as shown in Figure 3.13. When the voltage phasor diagram is ready, the upper layer of the winding is set.

The positions of the coil sides in the bottom layer are defined when an appropriate coil span is selected. For fractional slot windings, it is not possible to construct a full-pitch winding, this is because $q \notin N$.

The full-pitch coil span, y_Q of a full-pitch winding would be y in slot pitches $y = y_Q = mq = 3 \times 0.4 = 1.2 \notin N$. The coil span may be decreased by $y_v = 0.2$. The coil span becomes an integer, which enables the construction of the winding. $y = mq - y_v = 3 \times 0.4 - 0.2 = 1 \notin N$. Then, the winding layout can be found as shown in Table 3.8.

Biblography

4C Offshore, 2014a. Global Wind Speed Rankings. Available at: http://www.4coffshore.com/windfarms/windspeeds.aspx.

4C Offshore, 2014b. Greater Gabbard. Available at: http://www.4coffshore.com/windfarms/greater-gabbard-united-kingdom-uk05.html.

Adcock, I., 2012. Winning the Power Struggle. *Automotive Design*.

Arnold Magnetic Technologies, Sintered Neodymium-Iron-Boron Magnets. Available at: www.arnoldmagnetics.com/WorkArea/DownloadAsset.aspx?id=5305 [Accessed March 18, 2015].

ASM International, 1998. *Metals Handbook Desk* 2nd Enditi. J. R. Davis, ed., Boca Raton: CRC Press.

Aydin, M., Qu, R. & Lipo, T.A., 2003. Cogging torque minimization technique for multiple-rotor, axial-flux, surface-mounted-PM motors: alternating magnet pole-arcs in facing rotors. In *Industry Applications Conference, 2003. 38th IAS Annual Meeting. Conference Record of the*. pp. 555–561.

Bang, D., Polinder, H., Shrestha, G., et al., 2008. Design of a Lightweight Transverse Flux Permanent Magnet Machine for Direct-Drive Wind Turbines. In *Industry Applications Society Annual Meeting, 2008. IAS '08. IEEE*. Edmonton, pp. 1–7.

Bang, D., Polinder, H., Shrestha, et al., 2008. Review of Generator Systems for Direct-Drive Wind Turbines. In A. S. Kelikian & S. K. Sarrafian, eds. *EWEC*. Brussels: Lippincott Williams & Wilkin, pp. 1–11.

Bang, D. et al., 2009. Ring-Shaped Transverse Flux PM Generator for Large Direct-Drive Wind Turbines. In *Power Electronics and Drive Systems, 2009. PEDS 2009. International Conference on*. Taipei, pp. 61–66.

Bang, D. & Polinder, H., 2010. *UpWind Research Report, Electromagnetic Optimization of Direct-drive Generators*,

Barakat, G., El-meslouhi, T. & Dakyo, B., 2001. Analysis of the cogging torque behavior of a two-phase axial flux permanent magnet synchronous machine. *IEEE Transactions on Magnetics*, 37(4), pp.2803–2805.

BBC, 2009. Wind Farm Suffers Gearbox Faults. Available at: http://news.bbc.co.uk/1/hi/england/kent/8379569.stm.

Benecki, W.T., 2012. Permanent Magnet Industry Outlook-2013. *Magnetics Business & Technology*. Available at: http://www.magneticsmagazine.com/main/articles/permanent-magnet-industry-outlook-2013/ [Accessed April 15, 2015].

Bianchi, N. et al., 2006. Design Considerations for Fractional-Slot Winding Configurations of Synchronous Machines. *IEEE Transactions on Industry Applications*, 42(4), pp.997–1006.

Bianchi, N., Bolognani, S. & Frare, P., 2006. Design Criteria for High-Efficiency SPM Synchronous Motors. *IEEE Transactions on Energy Conversion*, 21(2), pp.396–404.

Bianchi, N., Bolognani, S. & Frare, P., 2003. Design criteria of high efficiency SPM synchronous motors. In *IEEE International Electric Machines and Drives Conference, 2003. IEMDC'03.* pp. 1042–1048.

Bianchi, N. & Dai Pre, M., 2006. Use of the Star of Slots in Designing Fractional-slot Single-Layer Synchronous Motors. *Electric Power Applications, IEE Proceedings*, 153(3), pp.459– 466.

Blaabjerg, F. & Chen, Z., 2006. *Power Electronics for Modern Wind Turbines*, San Rafael: Morgan & Claypool.

Boglietti, A. et al., 2009. Evolution and Modern Approaches for Thermal Analysis of Electrical Machines. *IEEE Transactions on Industrial Electronics*, 56(3), pp.871–882.

Burton, T. et al., 2001. Wind-turbine Performance. In *Wind Energy Handbook*. New York: John Wiley & Sons.

Camilleri, R. et al., 2012. Investigation into the temperature profile of a liquid cooled YASA© AFPM machine. *6th IET International Conference on Power Electronics, Machines and Drives (PEMD 2012)*, pp.1–8.

Camilleri, R., Howey, D.A. & Mcculloch, M.D., 2012. Thermal Limitations in Air-Cooled Axial Flux In-Wheel Motors for Urban Mobility Vehicles : A Preliminary Analysis. In *Electrical Systems for Aircraft, Railway and Ship Propulsion (ESARS), 2012*. pp. 1–8.

Caricchi, F. et al., 1998. FEM Evaluation of Performance of Axial Flux Slotted Permanent Magnet Machines. In *The1998 IEEE Industry Applications Conference. Thirty-Third IAS Annual Meeting*. St. Louis, MO, pp. 12–17.

Chen, J., Nayar, C. V & Xu, L., 2000. Design and Finite-Element Analysis of an Outer-Rotor Permanent-Magnet Generator for Directly Coupled Wind. *IEEE Transactions on Magnetics*, 36(5), pp.3802–3809.

Chen, Y. & Lv, P., 2010. Structural optimization design for high-speed railway bridge erecting machine. *International Conference on Advanced Technology of Design and Manufacture (ATDM 2010)*, pp.176–180. Available at: http://digital-library.theiet.org/content/conferences/10.1049/cp.2010.1283.

Chen, Y. & Pillay, P., 2005. Axial-flux PM Wind Generator with a Soft Magnetic Composite Core. In *Conference Record of Industry Applications Conference, 2005. Fourtieth IAS Annual Meeting.* pp. 231–237.

Chen, Y., Pillay, P. & Khan, A., 2004. PM wind generator comparison of different topologies. In *Conference Record of the 2004 IEEE Industry Applications Conference 2004 39th IAS Annual Meeting*. pp. 1405–1412.

Chuang, F.C., 2009. Optimization for Reduction of Torque Ripple in an Axial Flux Permanent Magnet Machine. *IEEE Transactions on Magnetics*, 45(3), pp.1760–1763.

Chung, M.-J. & Gweon, D.-G., 2002. Modeling of the Armature Slotting Effect in the Magnetic Field Distribution of a Linear Permanent Magnet Motor. *Electrical Engineering*, 84(2), pp.101–108.

Clark, D., 2012. Has the Kyoto Protocol made any difference to carbon emissions? *The Guardian*.

Cleantech Investor Ltd, 2012. Wind Turbine Manufacturers Global Market Shares. *Cleantech Magazine*.

Cobham Technical Services, 2012. Opera-3d User Guide.

Cros, J. & Viarouge, P., 2002. Synthesis of High Performance PM Motors with Concentrated Windings. *IEEE Transactions on Energy Conversion*, 17(2), pp.248–253.

Cros, J., Viarouge, P. & Gélinas, C., 1998. Design of PM Brushless Motors Using Iron-resin Composites for Automotive Applications. In *The 1998 IEEE Industry Applications Conference, 1998. Thirty-Third IAS Annual Meeting.* St. Louis, MO, pp. 5–11.

Crozier, R. & Mueller, M., 2012. Integrated Structural and Electromagnetic Design of Direct-drive Linear Machines for Wave Energy. *IET Renewable Power Generation*, 6(3), pp.137–148.

Deb, K., 2009. Pseudo-Weight Vector Approach. In *Multi-objective Optimization using Evolutionary Algorithms*. Chichester: John Wiley & Sons, pp. 391–392.

Departement of Energy & Climate Change, 2011. *UK Renewable Energy Roadmap*,

Department of Energy & Climate Change, 2013. *DUKES 2013 Chapter 6: Renewable sources of energy*,

Dosiek, L. & Pillay, P., 2007. Cogging Torque Reduction in Permanent Magnet Machines. *IEEE Transactions on Industry Applications*, 43(6), pp.1565–1571.

El-Refaie, A.M. et al., 2006. Experimental Verification of Optimal Flux Weakening in Surface PM Machines using Concentrated Windings. *IEEE Transactions on Industry Applications*, 42(2), pp.443–453.

El-refaie, A.M., 2010. Fractional-Slot Concentrated-Windings Synchronous Permanent Magnet Machines : Opportunities and Challenges. *IEEE Transactions on Industrial Electronics*, 57(1), pp.107–121.

Enercon, 2013. Wind Turbines. Available at: http://www.enercon.de/en-en/Windenergieanlagen.htm [Accessed March 22, 2015].

Eom, J.-B. et al., 2001. Minimization of Cogging Torque in Permanent Magnet Motors by Teeth Pairing and Magnet Arc Design using Genetic Algorithm. *Journal of Magnetism and Magnetic Materials*, 226-230, pp.1229–1231.

Espanet, C., Miraoui, A. & Kauffmann, J.-M., 2003. Optimal Design of an High Torque DC Brushless in-Wheel Motor. In *IEEE International Electric Machines and Drives Conference, 2003. IEMDC'03.* Madison, pp. 1402–1409.

Fei, W., 2011. *Permanent Magnet Synchronous Machines with Fractional Slot and Concentrated Winding Configurations*. Cranfield University.

Fei, W. & Luk, P.C.K., 2009. An Improved Model for the Back-EMF and Cogging Torque Characteristics of a Novel Axial Flux Permanent Magnet Synchronous Machine With a Segmental Laminated Stator. *IEEE Transactions on Magnetics*, 45(10), pp.4609–4612.

Feng, Y., Tavner, P.J. & Long, H., 2010. Early Experiences with UK Round 1 Offshore Wind Farms. In *Proceedings of the Institution of Civil Engineers: energy.* pp. 167–181.

Ferrari, R., 2007. The Finite-Element Method, Part 2: P. P. Silvester, an Innovator in Electromagnetic Numerical Modeling. *IEEE Antennas and Propagation Magazine*, 49(3), pp.216–234.

Gamesa, 2013. Gamesa Homepage. Available at: http://www.gamesacorp.com/en/ [Accessed March 22, 2015].

General Electric, 2013. Wind Turbines. Available at: http://www.ge-energy.com/wind [Accessed March 22, 2015].

Global Wind Energy Council, 2013. *Global Wind Statistics 2012*,

Goldwind, 2013. Goldwind Homepage. Available at: http://www.goldwindglobal.com/web/index.do.

Gorginpour, H., Oraee, H. & Mcmahon, R.A., 2014. Electromagnetic-Thermal Design Optimization of the Brushless Doubly Fed Induction Generator. *IEEE Transactions on Industrial Electronics*, 61(4), pp.1710–1721.

Guodian United Power Technology Co. Ltd, 2013. Guodian United Power Homepage. Available at: http://www.gdupc.com.cn/defaultEn.aspx [Accessed March 22, 2015].

Gupta, C., Marwaha, S. & Manna, M.S., 2009. Finite Element Method as an aid to Machine Design: A Computational Tool. In *Proceedings of the COMSOL Conference*.

Hanselman, D.C., 2003. *Brushless Permanent Magnet Motor Design*, Madison: Magna Physics Publishing.

Hansen, A.D. & Hansen, L.H., 2007. Wind Turbine Concept Market Penetration over 10 Years (1995-2004). *Wind Energy*, 10, pp.81–97.

Hendershot, J.R. & Miller, T.J.E., 1995. *Design of Brushless Permanent-magnet Motors (Monographs in Electrical and Electronic Engineering)*, Madison: Clarendon PRess.

Hey, J., Howey, D.A. & Lamperth, M., 2010. Transient Thermal Modeling of an Axial Flux Permanent Magnet (AFPM) Machine Using a Hybrid Thermal Model. , pp.691–700.

Hillier, M.S. & Hillier, F.S., 2002. Conventional Optimization Techniques. In S. Ruhul, M. Masoud, & Y. Xin, eds. *Evolutionary Optimization*. Dordrecht: Kluwer Academic Publishers, p. 3.

Höganäs AB, 2013a. Somaloy 1000 3P SMC Datasheet. Available at: http://www.hipih.com/SMC/datasheet/SMC_HQlHUuLYJZzOJ.htm.

Höganäs AB, 2013b. Somaloy 700 3P SMC Datasheet. Available at: http://www.hipih.com/SMC/datasheet/SMC_2iAQgHhBGhqi3.htm.

Honsinger, V.B., 1987. Sizing Equations for Electrical Machinery. *IEEE Transactions on Energy Conversion*, EC-2(1), pp.116–121.

Hörz, M., Herzog, H. & Haas, A., 2006. Axial Flux Machine with Single Tooth Fractional Slot Winding - Comparison of Different Winding Design Approaches. In *International Symposium on Power Electronics, Electrical Drives, Automation and Motion, 2006. SPEEDAM 2006.* Taormina, pp. 1444–1448.

Howey, D. a., Childs, P.R.N. & Holmes, A.S., 2012. Air-gap Convection in Rotating Electrical Machines. *IEEE Transactions on Industrial Electronics*, 59(3), pp.1367–1375.

Howey, D.A., 2010. *Thermal Design of Air-cooled Axial Flux Permanent Magnet Machines*. Imperial College London.

Huang, S. et al., 1999. A Comparison of Power Density for Axial Flux Machines based on General Purpose Sizing Equations. *IEEE Transactions on Energy Conversion*, 14(2), pp.185–192.

Huang, S. et al., 1998. A General Approach to Sizing and Power Density Equations for Comparison of Electrical Machines. *IEEE Transactions on Industry Applications*, 34(1), pp.92–97.

Hwang, C. & Cho, Y.H., 2001. Effects of Leakage Flux on Magnetic Fields of Interior Permanent Magnet Synchronous Motors. *IEEE Transactions on Magnetics*, 37(4), pp.3021–3024.

Ida, N., 2000. *Engineering Electromagnetics*, New York: Springer.

Ivanovski, Z., 2011. Direct-drive Wind Turbines. *International Journal of Scientific & Engineering Research*, 2(10), pp.1–11.

Keysan, O., McDonald, A. & Mueller, M., 2011. A Direct Drive Permanent Magnet Generator Design for a Tidal Current Turbine(SeaGen). *2011 IEEE International Electric Machines & Drives Conference (IEMDC)*, pp.224–229.

LeVeque, R., 2004. *Finite Volume Methods for Hyperbolic Problems*, Cambridge: Cambridge University Press.

Li, H., Chen, Z. & Polinder, H., 2009. Optimization of Multibrid Permanent-Magnet Wind Generator Systems. *IEEE Transactions on Energy Conversion*, 24(1), pp.82–92.

Li, J. & Chen, Z., 2008. Overview of Different Wind Generator Systems and their Comparisons. *IET Renewable Power Generation*, 2(2), pp.123–138.

Liao, C., Katcher, T. & Chen, C.-L., 1999. Thermal Management of AC Induction Motors Using Computational Fluid Dynamics Modeling. In *IEEE International Electric Machines and Drives Conference. IEMDC'99.* pp. 189–191.

Lim, C.H. et al., 2011. Experimental Validation of CFD Modelling for Heat Transfer Coefficient Predictions in Axial Flux Permanent Magnet Generators. *International Journal of Thermal Sciences*, 50(12), pp.2451–2463.

London Array, 2014. Harnessing the Power of Offshore Wind. Available at: http://www.londonarray.com [Accessed March 22, 2015].

Magnussen, F. & Sadarangani, C., 2003. Winding Factors and Joule Losses of Permanent Magnet Machines with Concentrated Windings. In *IEEE International Electric Machines and Drives Conference, 2003. IEMDC'03.* pp. 333–339.

Marignetti, F., Colli, V.D. & Coia, Y., 2008. Design of Axial Flux PM Synchronous Machines Through 3-D Coupled Electromagnetic Thermal and. *IEEE Transactions on Industrial Electronics*, 55(10), pp.3591–3601.

Maynes, B.D.J. et al., 2003. Simulation of Airflow and Heat Transfer in Small Alternators using CFD. *IEE Proceedings - Electric Power Applications*, 150(2), pp.146–152.

Mcdonald, A.S., Mueller, M.A. & Polinder, H., 2008. Structural Mass in Direct-drive Permanent Magnet Electrical Generators. *IET Renewable Power Generation*, 2(1), pp.3–15.

Ming Yang, 2013. Investor Relations Home. Available at: http://ir.mywind.com.cn/phoenix.zhtml?c=238508&p=irol-IRHome.

Mueller, M.A., McDonald, A.S. & MacPherson, D.E., 2005. Structural Analysis of Low-speed Axial-flux Permanent-magnet Machines. *IEE Proceedings - Electric Power Applications*, 152(6), pp.1417–1426.

MWS Wire Industries, 2014a. Magnet Wire Insulation Guide. In *MWS Technical Data Book*. pp. 2–3.

MWS Wire Industries, 2014b. Square Magnet Wire. In *MWS Technical Data Book*. p. 7.

NdFeB_info.com, 2014. Temperature Ratings. Available at: http://www.ndfeb-info.com/temperature_ratings.aspx [Accessed April 5, 2015].

Negrea, M. & Rosu, M., 2001. Thermal Analysis of a Large Permanent Magnet Synchronous Motor for Different Permanent Magnet Rotor Configurations. In *IEEE International Electric Machines and Drives Conference. IEMDC 2001.* IEEE, pp. 777–781.

Odvárˇka, E. et al., 2010. Thermal modelling of water-cooled axial-flux permanent magnet machine. In *5th IET International Conference on Power Electronics, Machines and Drives (PEMD 2010)*. IET, pp. TU414–TU414.

Parviainen, A., 2005. *Design of Axial-flux Permanent-magnet Low-speed Machines and Performance Comparison between Radial-flux and Axial-flux Machines*.

Pelosi, G., 2007. The finite-element Method, Part I: R. L. Courant. *IEEE Antennas and Propagation Magazine*, 49(2), pp.180–182.

Perho, J., 2002. *Reluctance Network for Analysing Induction Machines*. Helsinki University of Technology.

Pinilla, M., 2012. Performance Improvement in a Renewable Energy Direct Drive Permanent Magnet Machine by means of Soft Magnetic Composite Interpoles. *IEEE Transactions on Energy Conversion*, 27(2), pp.440–448.

Polinder, H., 2006. Comparison of Direct-drive and Geared Generator Concepts for Wind Turbines. *IEEE Transactions on Energy Conversion*, 21(3), pp.725–733.

Polinder, H. et al., 2007. *Concept Report on Generator Topologies, Mechanical & Electromagnetic Optimization*,

Pompermaier, C., Sjöberg, L. & Nord, G., 2012. Design and Optimization of a Permanent Magnet Transverse Flux Machine. In *2012 XXth International Conference onElectrical Machines (ICEM)*. Marseille, pp. 606–611.

Proca, A.B., Keyhani, A. & El-Antably, A., 2003. Analytical Model for Permanent Magnet Motors with Surface Mounted Magnets. *IEEE Transactions on Energy Conversion*, 18(3), pp.386–391.

Pyrhnen, J., Jokinen, T. & Hrabovcov, V., 2008. *Design of Rotating Electrical Machines*, Chichester, UK: John Wiley & Sons, Ltd.

Qu, R., Aydin, M. & Lipo, T.A., 2003. Performance Comparison of Dual-rotor Radial-flux and Axial-flux Permanent-magnet BLDC Machines. In *IEEE International Electric Machines and Drives Conference, 2003. IEMDC'03.* IEEE, pp. 1948–1954.

Ragheb, M. & Ragheb, A.M., 2011. Wind Turbines Theory - The Betz Equation and Optimal Rotor Tip Speed Ratio. In R. Carriveau, ed. *Fundamental and Advanced Topics in Wind Power*. InTech, pp. 19–38.

Rasmussen, C.B. & Ritchie, E., 1997. A Magnetic Equivalent Circuit Approach for Predicting PM Motor Performance. In *Conference Record of the 1997 IEEE Industry Applications Conference Thirty-Second IAS Annual Meeting. IAS '97.* pp. 10–17.

RenewableUK, 2014. Offshore Wind. Available at: http://www.renewableuk.com/en/renewable-energy/wind-energy/offshore-wind/index.cfm [Accessed March 14, 2015].

Roark, R.J., 1932. *Stresses Produced in a Circular Plate by Eccentric Loading and By a Transverse Couple*, The University of Wisconsin Engineering experiment station.

Rostami, N. et al., 2012. Lumped-Parameter Thermal Model for Axial Flux Permanent Magnet. *IEEE Transactions on Magnetics*, 49(3), pp.1178–1184.

Roy, J. & Whitcomb, L.L., 1997. Structural Design Optimization and Comparative Analysis of a New High-Performance Robot Arm via Finite Element Analysis. In *Proceedings of the 1997 IEEE International Conference on Robotics and Automation*. Albuquerque, pp. 2190–2197.

Sheringham Shoal, 2014. Sheringham Shoal Homepage. Available at: http://www.scira.co.uk/ [Accessed April 14, 2015].

Siemens, 2012. Siemens 6.0MW Offshore Wind Turbine.

Siemens, 2013. Wind Power Solutions for Onshore, Offshore and Service Projects. Available at: http://www.energy.siemens.com/hq/en/renewable-energy/wind-power/ [Accessed April 14, 2015].

Silvester, P.P. & Ferrari, R.L., 1996. *Finite Elements for Electrical Engineers* 3rd ed., Cambridge: Cambridge University Press.

Sinovel, 2013. Sinovel Homepage. Available at: http://www.sinovel.com/en/index.aspx [Accessed April 14, 2014].

Sitapati, K., 2001. Performance Comparisons of Radial and Axial Field , Permanent Magnet , Brushless Machines. In *IEEE Transactions on Industry Applications*. pp. 1219–1226.

Solidworks, 2012. Convection Heat Coefficient. *Solidworks*. Available at: http://help.solidworks.com/2012/English/SolidWorks/cworks/Convection_Heat_Coefficient.htm [Accessed March 15, 2015].

Soong, W.L., 2008. Sizing of Electrical Machines. , pp.17–18.

Surahammmars Bruks AB, 2013a. Non Oriented Electrical Steel.

Surahammmars Bruks AB, 2013b. Non Oriented Electrical Steel Typical Data.

Suzlon, 2013. Suzlon Homepage. Available at: http://www.suzlon.com/ [Accessed April 14, 2015].

Svechkarenko, D., 2007. *On Analytical Modeling and Design of a Novel Transverse Flux Generator for Offshore Wind Turbines*. KTH.

Tangudu, J.K. et al., 2009. Lumped Parameter Magnetic Circuit Model for Fractional-slot Concentrated-winding Interior Permanent Magnet Machines. In *2009 IEEE Energy Conversion Congress and Exposition*. San Jose, pp. 2423–2430.

The Engineering Toolbox, 2014a. Air properties. Available at: http://www.engineeringtoolbox.com/air-properties-d_156.html [Accessed April 14, 2015].

The Engineering Toolbox, 2014b. Resistivity , Conductivity and Temperature Coefficients for some Common Materials. Available at: http://www.engineeringtoolbox.com/resistivity-conductivity-d_418.html.

The European Wind Energy Association, 2014. *Wind in power 2013 European Statistics*,

Toliyat, H.A. & Kliman, G.B., 2004. *Handbook of Electric Motors* 2nd ed., Boca Raton: CRC Press.

United Nations, 1998. Kyoto Protocol to the United Nations Framework Convention on Climate Change.

University of Colorado at Boulder, 2013. FEM Modeling: Mesh, Loads and BCs. In *Introduction to Finite Element Methods*. Boulder.

Vansompel, H., Sergeant, P., Dupre, L., et al., 2012. Evaluation of a Simple Lamination Stacking Method for the Teeth of an Axial Flux Permanent-Magnet Synchronous Machine With Concentrated Stator Windings. *IEEE Transactions on Magnetics*, 48(2), pp.999–1002.

Vansompel, H., Sergeant, P. & Dupr, L., 2012. A Multilayer 2-D – 2-D Coupled Model for Eddy Current Calculation in the Rotor of an Axial-Flux PM Machine. *IEEE Transactions on Energy Conversion*, 27(3), pp.784–791.

Veries, E. de, 2012. Enercon E-126 7.5MW Still World's Biggest.

Vestas, 2013. Vestas Homepage. Available at: http://www.vestas.com/ [Accessed April 14, 2015].

Vries, E. de, 2009. E-126 in Action: Enercon's Next-Generation Power Plant. *Renewable Energy World magazine*. Available at: http://www.renewableenergyworld.com/rea/news/article/2009/09/e-126-in-action-enercons-next-generation-power-plant [Accessed April 14, 2015].

Vun, S.T. & McCulloch, M.D., 2014. Optimal Design Method for Large Scale YASA Machines. *IEEE Transactions on Energy Conversion "Optimal Design of Electric Machines"*, Extended a.

Vun, S.T., McCulloch, M.D. & Leong, C.Y., 2011. The Development of an Electromagnetic Analytical Design Tool for Megawatt-scale YASA generators. In *IET Conference on Renewable Power Generation (RPG 2011)*. Edinburgh, p. 44.

Walney (UK) Offshore Windfarms Ltd, 2014. Wayney Offshore Windfarms.

Wanjiku, J.G. et al., 2011. Minimization of Cogging Torque in a Small Axial-flux PMSG with a Parallel-teeth Stator. In *2011 IEEE Energy Conversion Congress and Exposition*. pp. 3687–3693.

WindPower, 2006. *Capital Grant Scheme for Offshore Wind Kentish Flats Offshore Wind Farm Annual Report (2006)*,

WindPower, 2007. *Offshore Wind Capital Grants Scheme Kentish Flats Offshore Wind Farm 2nd Annual Report (2007)*,

Windpower, 2008. *Offshore Wind Capital Grants Scheme Kentish Flats Offshore Wind Farm 3rd Annual Report (2008)*,

Woolmer, T., 2010. Wheel-hub Motor Cooling.

Woolmer, T.J., 2009. *The Yokeless and Segmented Armature Machine Developed for The LIFECar*. University of Oxford.

Woolmer, T.J. & McCulloch, M.D., 2007. Analysis of the Yokeless And Segmented Armature Machine. In *2007 IEEE International Electric Machines Drives Conference*. pp. 704–708.

Yilmaz, M. & Krein, P.T., 2008. Capabilities of Finite Element Analysis and Magnetic Equivalent Circuits for Electrical Machine Analysis and Design. In *2008 IEEE Power Electronics Specialists Conference*. IEEE, pp. 4027–4033.

Young, W.C. & Budynas, R.G., 2002. Beams; Flexure of Straight Bars. In *Roark's Formulas for Stress and Strain*. New York: McGRAW-HILL, pp. 125–266.

Young, W.C. & Budynas, R.G., 1938. *Roark's Formulas for Stress and Strain* 1st ed., New York: McGRAW-HILL.

Young, Warren C., Budynas, R.G., 2002. *Roark's Formulas for Stress and Strain* 6th ed., New York: McGRAW-HILL.

Zarko, D., Ban, D. & Lipo, T.A., 2008. Analytical Solution for Cogging Torque in Surface Permanent-Magnet Motors Using Conformal Mapping. *IEEE Transactions on Magnetics*, 44(1), pp.52–65.

Zavvos, A. et al., 2012. Structural Analysis and Optimisation of Transverse Flux Permanent Magnet Machines for 5 and 10 MW Direct Drive Wind Turbines. *Wind Energy*, 15, pp.19–43.

Zavvos, A. et al., 2012. Structural Comparison of Permanent Magnet Direct Drive Generator Topologies for 5MW Wind Turbines. In *6th IET International Conference on Power Electronics, Machines and Drives (PEMD 2012)*. Bristol: Iet, pp. 1–6.

Zhang, S., 2005. Problems Experienced with Operating Wind Farms in China. In *2005 IEEE/PES Transmission & Distribution Conference & Exposition: Asia and Pacific*. IEEE, pp. 1–5.

Zhang, Y. & Ula, S., 2008. Comparison and Evaluation of Three Main Types of Wind Turbines. In *Transmission and Distribution Conference and Exposition*. Chicago, pp. 1–6.

Zhang, Z. et al., 2012. Large-diameter Ironless Permanent Magnet Generator for Offshore Wind Power Application. In *2012 XXth International Conference on Electrical Machines*. Marseille, pp. 684–690.

Zhang, Z. et al., 2011. Review of modeling methods in electromagnetic and thermal design of permanent magnet generators for wind turbines. In *2011 International Conference on Clean Electrical Power (ICCEP)*. IEEE, pp. 377–382.

Zhu, Z.Q., 2009. Fractional Slot Permanent Magnet Brushless Machines and Drives for Electric and Hybrid Propulsion Systems. In *Ecologic Vehicles Renewable Energies*.